Title

New Methods for Quantum Mechanical Reaction Dynamics

Author

Thompson, Ward H

Publication Date

1996-12-01

LBNL-40238
UC-411

ERNEST ORLANDO LAWRENCE
BERKELEY NATIONAL LABORATORY

New Methods for Quantum Mechanical Reaction Dynamics

Ward H. Thompson
Chemical Sciences Division

December 1996
Ph.D. Thesis

DISCLAIMER

LBNL-40238
UC-411

New Methods for Quantum Mechanical Reaction Dynamics

Ward Hugh Thompson
Ph.D. Thesis

Department of Chemistry
University of California, Berkeley

and

Chemical Sciences Division
Lawrence Berkeley Laboratory
University of California
Berkeley, CA 94720

December 1996

This work was supported by the Director, Office of Energy Research, Office of Basic Energy Sciences, Chemical Sciences Division, of the U.S. Department of Energy under Contract No. DE-AC03-76SF00098.

New Methods for Quantum Mechanical Reaction Dynamics

by

Ward Hugh Thompson

B. S. (Oklahoma State University) 1991

A dissertation submitted in partial satisfaction of the

requirements for the degree of

Doctor of Philosophy

in

Chemistry

in the

GRADUATE DIVISION

of the

UNIVERSITY of CALIFORNIA at BERKELEY

Committee in charge:

Professor William H. Miller, Chair
Professor Robert A. Harris
Professor Robert G. Littlejohn

1996

New Methods for Quantum Mechanical Reaction Dynamics

by

Ward Hugh Thompson

Abstract

New Methods for Quantum Mechanical Reaction Dynamics

by

Ward Hugh Thompson

Doctor of Philosophy in Chemistry

University of California at Berkeley

Professor William H. Miller, Chair

Quantum mechanical methods are developed to describe the dynamics of bimolecular chemical reactions. We focus on developing approaches for ***directly*** calculating the desired quantity of interest.

Methods for the calculation of single matrix elements of the scattering matrix (S-matrix) and initial state-selected reaction probabilities are presented. This is accomplished by the use of absorbing boundary conditions (ABC) to obtain a localized (L^2) representation of the outgoing wave scattering Green's function. This approach enables the efficient calculation of only a single column of the S-matrix with a proportionate savings in effort over the calculation of the entire S-matrix. Applying this method to the calculation of the initial (or final) state-selected reaction probability, a more averaged quantity, requires even less effort than the state-to-state S-matrix elements.

It is shown how the same representation of the Green's function can be effectively applied to the calculation of negative ion photodetachment intensities. Photodetachment spectroscopy of the anion ABC^- can be a very useful method for obtaining detailed information about the neutral ABC potential energy surface, particularly if the ABC^- geometry is similar to the transition state of the neutral ABC. Total and arrangement-selected photodetachment spectra are calculated for the H_3O^- system, providing information about the potential energy surface for the $OH + H_2$ reaction when compared with experimental results.

Finally, we present methods for the direct calculation of the thermal rate constant from the flux-position and flux-flux correlation functions. The spirit of transition state

theory is invoked by concentrating on the short time dynamics in the area around the transition state that determines reactivity. These methods are made efficient by evaluating the required quantum mechanical trace in the basis of eigenstates of the Boltzmannized flux operator. This operator is of low rank, approximately equal to twice the number of states of the "activated complex." Applications to the D + H_2 and O + HCl reactions illustrate the power and usefulness of the present approach. The power of these methods should extend the range of accessible systems beyond reactions involving 3 or 4 atoms.

To my parents

Contents

List of Figures

List of Tables

Acknowledgements

I would like to thank my research advisor, Prof. William H. Miller, for his excellent guidance and support over the years. Working with him has been a challenging, enlightening, and thoroughly enjoyable experience. It is a rare opportunity to learn from such an exceptional scientist, and I am grateful for it.

I am indebted to Prof. Robert A. Harris for leading me to a higher understanding of quantum mechanics, both through his graduate courses and by allowing me to TA for him. I also wish to thank Prof. Daniel M. Neumark for many useful conversations on transition state spectroscopy.

I would particularly like to thank those graduate students, postdocs, and visiting professors with whom I have collaborated or worked closely: Scott Auerbach, Esther de Beer, Tim Germann, Dan Gezelter, Gerrit Grönenboom, Rig Hernandez, Hans Karlsson, Srihari Keshavamurthy, Prof. Claude Leforestier, Bill Poirer, Dave Skinner, Bruce Spath, and Haobin Wang. They have been the source of innumerable interesting discussions and useful insights.

My interaction with the past and present members of the Miller group has been an integral part of my graduate school education and I would like to acknowledge Yan-Tyng "Sherry" Chang, Dan Colbert, Åke Edlund, Lionel Gaucher, Victor Guallar, Prof. Nick Handy, Stephan Krempl, Uwe Manthe, Prof. Miquel Moreno, Johannes Natterer, Uri Peskin, Prof. Hanna Reisler, Peter Saalfrank, Günter Schmid, Tamar Seideman, Kathy Sorge, Gerhard Stock, Sean Sun, Agathe Untch, Prof. David Wardlaw, Joshua Wilkie, and Clemens Woywod. In addition, graduate students and postdocs in many other groups have made Berkeley an exciting place to learn.

I am grateful to Cheryn Gliebe for making life at Berkeley more enjoyable with her friendship and cheerful assistance. Without her help I am sure that I would have been sued, incarcerated, or unduly terminated at some point in my graduate career.

I wish to thank the students, postdocs, and professors in the Physics and Chemistry departments at Oklahoma State University. In particular, I am indebted to Prof. Paul Westhaus for allowing me to work with him. I benefited greatly from

his incredible dedication and patience. I am also appreciative of the many people in the Chemistry department at the University of Southern California who made my summer there interesting and enlightening.

Finally, I wish to thank my family. Without them I would not be where or who am I today. My sisters, Sunnie and Stacy, and my brother-in-law, Roy, have provided me with moral support and the occasional diversion over the years. More than anyone else, my parents are responsible for the completion of this degree. They have been a constant source of inspiration, support, and encouragement, and have always put my needs above theirs. My wife, Cindy, has always been there to lift my spirits, motivate me, or bring me back to reality. She has helped make my years in graduate school a very happy period in my life.

Chapter 1

Introduction

Understanding gas phase reaction dynamics is of great importance to the field of chemistry. Gas phase chemical reactions play a crucial role in processes occurring in the atmosphere, in combustion, in explosions, and in industrial procedures. On a more fundamental level, much of the basic physics of reaction dynamics can be investigated, unobscured, by the examination of isolated bimolecular collisions. This knowledge, thus acquired, can then be applied in the study of chemistry occurring in solution, in clusters, and on surfaces.

While classical and semiclassical approaches are of great use and describe many systems quite accurately, the fully correct treatment of reaction dynamics is quantum mechanical. For many reactions, a quantum mechanical treatment is required, such as for the hydrogen transfer reactions examined in this work, where tunneling can play an important role. However, in other cases where classical and semiclassical methods are accurate, it is also useful to have a viable quantum mechanical approach as a diagnostic tool for evaluating the usefulness and applicability of these methods. Such a comparison for relatively small systems can then aid in the interpretation of classical and semiclassical applications to larger systems which cannot be treated fully quantum mechanically. In addition, a rigorous quantum mechanical approach serves as a starting point for more approximate methods such as mixed quantum-classical, mixed quantum-semiclassical, or transition state theories.

It has been 20 years since the first rigorous quantum mechanical calculations

of the state-to-state reaction dynamics for an atom-diatom collision, the H + H_2 system, were carried out by Schatz and Kuppermann.[1,2] Yet, only now have the first state-to-state treatments of a *four* atom system appeared, for the OH + H_2 reaction. Indeed, it took more than a decade, and advances in both the available theory and computational power, before three atom reactive systems could be treated routinely. Still, many reactions of a diatom with an atom resist treatment, particularly in cases where a deep well and/or heavy masses are involved. The speed of computers will continue to increase in the near future, but it seems clear that without advances in the theory for treating the dynamics of chemical reactions the size of accessible systems will remain limited.

In this work, we attempt to advance the quantum mechanical theory of chemical reaction dynamics. While a complete treatment of the problem would begin with first principles in treating the full electron and nuclear problem, our starting point is the Born-Oppenheimer approximation. For many systems of interest this is an excellent approximation and we therefore focus on accurate representations of the dynamics of the nuclear degrees of freedom on a single Born-Oppenheimer surface or, in the case of the photodetachment intensities in Chapter 3, an instantaneous transition between two surfaces. In some of the present work it maybe be possible to straightforwardly account for deviations from the Born-Oppenheimer assumption, but this has been left as an area for future work.

Advances in experimental methods, particularly techniques involving molecular beams and lasers, have allowed the measurement of very detailed dynamical quantitities. The typical quantitities of interest include the differential cross section, given (for the case of an atom-diatom reaction) as

$$\sigma_{\tau' v' j' K' \leftarrow \tau v j K}(\theta) = \left| \frac{1}{2ik_{\tau vj}} \sum_J (2J+1)\, d^J_{K'K}(\theta)\, S_{\tau' v' j' K', \tau v j K} \right|^2 , \qquad (1.1)$$

in the helicity representation.[3] Here τ and τ' are indices representing different chemical arrangements, vjK ($v'j'K'$) are the initial (final) vibrational, rotational, and helicity quantum numbers, respectively, and $k_{\tau vj}$ is the initial translational wavevector for state vj. θ is the angle between the initial and final translational wavevectors, and

$d^J_{K'K}(\theta)$ is the reduced Wigner rotation matrix.[4,5] Finally, the $S^J_{n',n}$ are the state-to-state S-matrix elements giving the probability amplitude for reacting from state $n = vjK$ of the reactants (arrangement τ) into state $n' = v'j'K'$ of the products (arrangement τ'), for total angular momentum J. Note that to obtain the differential cross section, one adds the amplitudes and then squares so that there is interference between the different partial waves. This is the most detailed quantity measurable for a chemical reaction.

Also of interest is the integral cross section,[3]

$$\sigma_{\tau'v'j'K'\leftarrow\tau vjK} = \frac{\pi}{k^2_{\tau vj}} \sum_{J=\min(K,K')} (2J+1)\ |S_{\tau'v'j'K',\tau vjK}|^2 . \tag{1.2}$$

Here the probability amplitudes are squared and then added so the partial waves do not interfere. We have written these quantities in the fully state-resolved forms, but only rarely is this resolution approached in an experiment. For example, often only the initial state-selected cross section is measured where no attempt is made to determine the product quantum state.

In many cases, experiments are not state-resolved at all and a rate constant is measured. Depending on whether the experiment is carried out at a fixed total energy (as is often the case for unimolecular reactions) or at a fixed temperature, the microcanonical rate constant

$$k(E) = \frac{1}{2\pi\hbar\rho_r(E)} N(E), \tag{1.3}$$

or the thermal (canonical) rate constant,

$$k(T) = \frac{1}{2\pi\hbar Q_r(T)} \int_0^\infty e^{-\beta E} N(E)\, dE, \tag{1.4}$$

is obtained, where $\beta = 1/k_bT$. Here $N(E)$ is the cumulative reaction probability,

$$N(E) = \sum_{n_p,n_r} |S_{n_p,n_r}|^2, \tag{1.5}$$

(which is the reaction probability out of all reactant states for a fixed total energy E), $\rho_r(E) = \mathrm{Tr}_r[\delta(E-\hat{H})]$ is the reactant microcanonical density of states per unit

energy (Tr_r implies a trace over reactant states only), and $Q_r(T)$ is the canonical reactant partition function per unit volume given by

$$Q_r(T) = \left(\frac{2\pi\mu k_b T}{h^2}\right)^{3/2} \sum_{n_r} g_{n_r}\, e^{-\beta\epsilon_{n_r}}. \tag{1.6}$$

Here, μ is the reduced mass for the relative translation of the reactants, the ϵ_{n_r} are the energy levels of the reactant internal degrees of freedom, and g_{n_r} is the degeneracy of reactant state n_r.

From a theoretical point of view, one calculates the S-matrix elements and combines them together in the indicated way to obtain the desired quantity (cross section or rate constant). The current state of the art methods for obtaining the S-matrix are the coupled channel approach and the S-matrix Kohn variational principle,[6–8] both of which obtain the entire state-to-state S-matrix in a single calculation. If, however, one is not interested in a full state-to-state cross section, then these methods require great effort to be expended to obtain the S-matrix and then the hard won detail is summarily averaged over. What is needed, and what is the goal of this work is a set of methods that allow the quantity of interest to be obtained *directly*, *i.e.*, without first calculating some more detailed quantity. Such an approach has already been developed for the cumulative reaction probability.[9–12]

In Chapter 2 we discuss the calculation of single S-matrix elements and initial state-selected reaction probabilities. The key to these methods is the proper imposition of the outgoing wave boundary conditions. The coupled channel and S-matrix Kohn methods enforce these boundary conditions by explicitly including every possible asymptotic channel in all arrangements which is the reason they yield the entire S-matrix in a single calculation. In Chapter 2 it is shown how absorbing boundary conditions (ABC) can be used to obtain a localized (L^2) representation of the outgoing wave scattering Green's function. This approach enables the efficient calculation of only a single S-matrix element (or indeed an entire column of the S-matrix) with a proportionate savings in effort. Applying this method to the calculation of initial (or final) state-selected reaction probabilities requires even less effort for this more averaged quantity.

Chapter 3 demonstrates how this same representation of the Green's function can be effectively applied to the calculation of negative anion photodetachment intensities. Photodetachment spectroscopy has proven to be a very useful method for evaluating the transition state region of a reactive potential energy surface and is sometimes referred to as transition state spectroscopy.[13,14] In a typical scenario, a negative ion ABC^- is formed and crossed with a laser, detaching the electron and forming an unstable complex ABC which then falls apart. If the ABC^- geometry is similar to that of the transition state of the neutral ABC, such an experiment can provide detailed information about the saddle point region of the neutral potential. This approach generally requires theoretical simulations of the photodetachment spectra. In Chapter 3, total and arrangement-selected photodetachment spectra are calculated for the H_3O^- system providing information about the potential energy surface for the $OH + H_2$ reaction when compared with experimental results.[15]

Finally, Chapter 4 describes the direct calculation of the thermal rate constant from flux correlation functions. These methods invoke the spirit of transition state theory by concentrating on the short time dynamics in the area around the transition state that determines reactivity. Applications are presented to the one-dimensional Eckart barrier, the collinear $H + H_2$ reaction, and the three-dimensional $D + H_2$ and $O + HCl$ reactions. The power of these methods should make them applicable to larger systems (> 3, or even 4, atoms).

Chapter 2

Reaction Probabilities

2.1 Introduction

All the information quantum mechanics gives about a chemical reaction is contained in the scattering matrix (S-matrix). Each S-matrix element is the probability amplitude of reacting from a specific initial quantum state of the asymptotically separated reactants into a particular final quantum state of the asymptotically separated products. Thus, if one can calculate the S-matrix, all the possible experimentally measurable quantities for the reaction can be subsequently computed (*e.g.*, integral and differential cross sections, canonical and microcanonical rate constants, etc.). Many theoretical methods have been developed to calculate the S-matrix elements. However, most experiments are not fully state-selected since preparing reactants in a specified state and measuring the resulting state of the products is a formidable task. In general one is only interested in more averaged quantities anyway. And while for experimentalists, *measuring* more averaged quantities requires considerably less effort, until recently *calculating* more averaged quantities required the same effort as obtaining the most detailed quantities. Previous theoretical methods involved calculating the entire S-matrix, then summing and averaging this detailed information to obtain the desired quantity.

Methods for calculating the entire S-matrix are clearly useful and necessary. For instance, the phase information contained in these probability *amplitudes* is re-

quired for computing the differential cross section. Additionally, if more than one measurable quantity is desired, the S-matrix provides the information to obtain them all in a single calculation. However, these methods are computationally expensive which so far has made them unfeasible for reactions involving more than three atoms. Methods for *directly* calculating averaged quantities with a proportionate savings in effort are therefore of great value. Ideally one is seeking a hierarchy of methods in which all levels of detail can be obtained for a computational price commensurate with the level of detail.

2.2 Quantum Reactive Scattering

Here we first present a review of formal scattering theory to illustrate how the solution of the Schrödinger equation leads to the relevant relations involving the S-matrix.[16–18] In particular, we highlight some of the properties of the Green's function and its role in these expressions. We discuss the proper imposition of the physical boundary conditions for the scattering problem, specifically how this can be accomplished by the use of absorbing boundary conditions (ABC). We then express the relations in a finite basis, in this case a discrete variable representation (DVR). Finally we show how more averaged quantities, such as half state-selected and cumulative reaction probabilities can be computed directly within this formulation.

2.2.1 Review of Formal Theory

All the information about a quantum mechanical system is contained in the solution of the time-independent Schrödinger equation:

$$(\hat{H} - E)|\Psi\rangle = 0. \tag{2.1}$$

The most familiar case is that in which the system is bound and the solution of this equation yields the discrete energy eigenvalues and the corresponding eigenstates. The fact that the spectrum is discrete results from the physical boundary conditions of the system: namely that $\Psi(x) \to 0$ as $|x| \to \infty$ since $V(x) \to \infty$ as $|x| \to \infty$. (These

are known as homogeneous boundary conditions.) However, the case of interest to us, is that of the scattering of particles (*i.e.*, an unbound system in which $V(x) \not\to \infty$ as $|x| \to \infty$). In this case the energy spectrum is continuous and the Schrödinger equation is solved for a specified energy to obtain the scattering wavefunction, $\Psi(E)$. (The nature of the energy spectrum is again due to the physical boundary conditions which are: $\Psi(x) \to \Phi(x)$ as $|x| \to \infty$, where Φ is a nonzero, asymptotic solution of the Schrödinger equation which is a combination of an incoming plane wave and outgoing spherical waves. These boundary conditions are called inhomogeneous.)

For the bound system the typical procedure for solving the Schrödinger equation is relatively straightforward. A basis set representation is chosen, the matrix elements of the Hamiltonian in this basis are calculated, and the resulting linear algebra equation

$$(\mathbf{H} - E\mathbf{I}) \cdot \mathbf{c} = \mathbf{0} \tag{2.2}$$

is diagonalized to obtain the eigenvalues $\{E_n\}$ and the eigenstates $\{\Psi_n\}$. Here $\mathbf{H}$ is the Hamiltonian matrix, $\mathbf{I}$ the identity matrix, and $\mathbf{c}$ a vector of coefficients of the basis functions (Ψ_n is obtained as linear combination of the basis functions with coefficients $\mathbf{c}$ determined from the diagonalization procedure). At first glance, the scattering system cannot be treated in the similar manner since the boundary conditions are more complicated. In fact, this is one of the primary goals of this work – to put the solution of scattering problems on the same footing as bound state problems. Namely, one hopes to obtain an approach which consists of: (1) choosing a basis, (2) calculating matrix elements, and (3) performing a linear algebra problem.

In contrast to the bound system, the scattering system must have a wavefunction that is nonzero over an infinite stretch of space encompassing the interaction region, where the colliding particles are close together, as well as the completely separated reactants and products. Clearly this eliminates a straightforward use of a *finite* basis representation. However, the wavefunctions of the isolated reactants and products are often easily obtained since the problem can be separated into uncoupled problems of the eigenfunctions of the two fragments and a plane wave describing their relative translation. Since the wavefunction is known in these asymptotic re-

gions of the potential, the effort of a finite basis approach must be centered on the interaction region. This raises the crucial issue of how to solve the problem in the interaction region once the asymptotic wavefunctions in the reactant and product valleys are known; the key to this is the proper enforcement of the scattering boundary conditions.

The Schrödinger equation is a homogeneous differential equation but for a scattering problem the boundary conditions are inhomogeneous. However, it is possible to write Eq. (2.1) in the form of an inhomogeneous equation. This allows the boundary conditions to be introduced into the differential equation itself. We do this by separating the Hamiltonian into a zeroth order part, $\hat{H}_0$, which describes the separated fragments and an interaction potential, $\hat{V}_{int}$, which describes the interactions of the fragments as they come together. Then Eq. (2.1) can be rewritten as

$$(E - \hat{H}_0)|\Psi\rangle = \hat{V}_{int}|\Psi\rangle. \tag{2.3}$$

The general solution of such an inhomogeneous equation is the sum of a complementary solution ϕ which satisfies the corresponding homogeneous equation:

$$(E - \hat{H}_0)|\phi\rangle = 0, \tag{2.4}$$

and a particular solution χ which is any solution of the inhomogeneous equation,

$$(E - \hat{H}_0)|\chi\rangle = \hat{V}_{int}|\Psi\rangle. \tag{2.5}$$

For the purpose of illustration, let us consider the concrete example of collinear atom-diatom scattering. Writing the Hamiltonian in the Jacobi coordinates of the reactant arrangement,

$$\hat{H} = -\frac{\hbar^2}{2\mu_R}\frac{\partial^2}{\partial R^2} - \frac{\hbar^2}{2\mu_r}\frac{\partial^2}{\partial r^2} + V(r, R). \tag{2.6}$$

A straightforward choice for the zeroth order Hamiltonian is to take

$$\hat{H}_0 = \lim_{R\to\infty} \hat{H} = -\frac{\hbar^2}{2\mu_R}\frac{\partial^2}{\partial R^2} - \frac{\hbar^2}{2\mu_r}\frac{\partial^2}{\partial r^2} + \nu_{asym}(r), \tag{2.7}$$

since the potential becomes independent of R when the reactants are completely separated (for the molecular scattering cases we will consider). Then the interaction potential is given by

$$V_{int}(r,R) = V(r,R) - v_{asym}(r). \tag{2.8}$$

The complementary solution must be an eigenfunction of $\hat{H}_0$; this Hamiltonian is separable and the eigenfunctions have the form

$$\phi_n(r,R) = \frac{e^{-ik_nR}}{v_n^{1/2}}\,\varphi_n(r). \tag{2.9}$$

where $k_n = \sqrt{2\mu_R(E-\varepsilon_n)/\hbar^2}$ is the wavevector, $v_n = \hbar k_n/\mu_R$ the velocity, and φ_n the solution of the asymptotic vibrational Hamiltonian:

$$\left[-\frac{\hbar^2}{2\mu_r}\frac{\partial^2}{\partial r^2} + v_{asym}(r)\right]\varphi_n(r) = \varepsilon\varphi_n(r). \tag{2.10}$$

The factor of $\sqrt{v_n}$ normalizes ϕ_n to have unit incident flux. (This is just one possible choice of the normalization factor.)

Obtaining the particular solution of the inhomogeneous equation is much harder. A standard technique for solving such equations is the method of Green's functions.[19] The Green's function for this problem is defined as the solution of the differential equation

$$[E - H_0(\mathbf{q})]\; G_0(\mathbf{q},\mathbf{q}') = \delta(\mathbf{q}-\mathbf{q}'), \tag{2.11}$$

where $\mathbf{q} = (R,r)$. This is the inhomogeneous equation with the inhomogeneity replaced by a Dirac delta function. From this equation, one can recognize that the Green's function is in fact the inverse of $E - \hat{H}_0$. This presents a complication since the Green's function will be singular whenever E equals an eigenvalue of $\hat{H}_0$. And since $\hat{H}_0$ is the Hamiltonian for a scattering problem it has a continuous set of eigenvalues. This is dealt with by adding a small imaginary constant, $i\epsilon$, to the energy with the understanding that after all the manipulations are complete, the limit is taken that ϵ goes to zero. Thus, the Green's function becomes

$$G_0^+(\mathbf{q}',\mathbf{q};E) = \lim_{\epsilon\to 0^+} \langle\mathbf{q}'|\,(E + i\epsilon - \hat{H}_0)^{-1}\,|\mathbf{q}\rangle, \tag{2.12}$$

where we have added the superscript + to G_0 to denote that we chose to add a *positive* (imaginary) constant. We could just as well have subtracted $i\epsilon$ from the energy (to give G_0^-) but that would represent the imposition of a different set of boundary conditions, as will be discussed below.

Once the Green's function is known, the particular solution is obtained by convoluting $G_0^+(\mathbf{q}, \mathbf{q}', E)$ with the inhomogeneity:

$$\chi^+(\mathbf{q}) = \int d\mathbf{q}'\, G_0^+(\mathbf{q}, \mathbf{q}'; E)\, V_{int}(\mathbf{q}')\, \Psi^+(\mathbf{q}'). \tag{2.13}$$

These equations do carry with them a physical interpretation. If we imagine a beam of A atoms colliding with beam of B-C molecules, at large separation the wavefunction is a product of an incoming wave describing the two fragments coming together and the (as yet) unperturbed vibrational state, n, of BC. As a result of the collision a scattered wave is emanated outward describing A-B + C motion. (Scattered waves are also produced describing A + B-C resulting from elastic and inelastic collisions.) Thus, the physical boundary condition of the problem must be that asymptotically the wavefunction is a combination of an incoming plane wave and outgoing scattered waves in each channel. (Here, a "channel" refers to a possible asymptotic state of A-B(n') + C or A + B-C(n') products of the collision.) The coefficient of each of these scattered waves is the S-matrix element equal to the probability amplitude for reacting from the initial (incoming) state into the final (outgoing) channel:

$$\Psi_n^+(E) \sim \frac{e^{-ik_n R}}{\sqrt{v_n}}\, \phi_n(r) + \sum_{n'} \frac{e^{ik_{n'} R}}{\sqrt{v_{n'}}}\, \phi_{n'}(r)\, S_{n' \leftarrow n}(E) \tag{2.14}$$

(Note that the wavefunction must also be regular at the origin: $\lim_{R \to 0} \Psi_n^+(R) = 0$.) Naturally, the generator of these scattered waves is the interaction potential between the two fragments and the nature of this potential determines reaction dynamics and hence, the scattered waves as is evident from Eq. (2.13). [If we had *subtracted* $i\epsilon$ from the energy (instead of adding it) to obtain the incoming wave Green's function G_0^- the resulting asymptotic form of the scattering wavefunction would be

$$\Psi_n^-(E) \sim \frac{e^{-ik_n R}}{\sqrt{v_n}}\, \phi_n(r) + \sum_{n'} \frac{e^{-ik_{n'} R}}{\sqrt{v_{n'}}}\, \phi_{n'}(r)\, C_{n' \leftarrow n}(E). \tag{2.15}$$

Thus, this choice of the sign of $i\epsilon$ gives the scattered waves as *incoming.*]

We can obtain the same result by some simple operator algebra. The solution to Eq. (2.5) may be obtained by multiplying from the left with $(E - \hat{H}_0)^{-1}$ which we now recognize as the Green's function. (This might more correctly be called the Green's operator, but it should be obvious when the Green's function is really a function and when it is really an operator.) This gives an equation for χ,

$$\chi = (E - \hat{H}_0)^{-1} \hat{V}_{int} \Psi. \tag{2.16}$$

Clearly, this is the operator form of Eq. (2.13) once we make the identification

$$(E - \hat{H}_0) \hat{G}_0 = \hat{I}. \tag{2.17}$$

Again, there is the problem of $\hat{G}_0$ being singular and it is necessary to add a small imaginary constant to the energy.

We now need to address the issue of solving the Schrödinger equation for for the full scattering wavefunction, Ψ^+. Recall that the full solution to the differential equation in (2.3) is the sum of the complementary and particular solutions so that $\Psi^+ = \phi + \chi^+$ and

$$\Psi^+ = \phi + \hat{G}_0^+ \hat{V}_{int} \Psi^+. \tag{2.18}$$

This is known as the Lippmann-Schwinger equation. Note that this is an integral equation that requires us to know Ψ^+ before we can obtain it. We need somehow to resolve this and "close" the equation. This can be accomplished if we substitute the expression for Ψ^+ into the right hand side to obtain

$$\Psi^+ = \phi + \hat{G}_0^+ \hat{V}_{int} \phi + \hat{G}_0^+ \hat{V}_{int} \hat{G}_0^+ \hat{V}_{int} \Psi^+. \tag{2.19}$$

Continuing to iteratively substitute we obtain an equation containing an infinite series of terms involving $\hat{G}_0^+$ and $\hat{V}_{int}$:

$$\begin{aligned} \Psi^+ &= \phi + \hat{G}_0^+ \hat{V}_{int} \phi + \hat{G}_0^+ \hat{V}_{int} \hat{G}_0^+ \hat{V}_{int} \phi + \hat{G}_0^+ \hat{V}_{int} \hat{G}_0^+ \hat{V}_{int} \hat{G}_0^+ \hat{V}_{int} \phi + \cdots \\ &= \phi + [1 + \hat{G}_0^+ \hat{V}_{int} + (\hat{G}_0^+ \hat{V}_{int})^2 + \cdots] \hat{G}_0^+ \hat{V}_{int} \phi. \end{aligned} \tag{2.20}$$

The quantity in the square brackets is immediately recognized as a geometric series the sum of which can be expressed in closed form to give

$$\Psi^+ = \phi + (1 - \hat{G}_0^+ \hat{V}_{int})^{-1} \hat{G}_0^+ \hat{V}_{int} \phi. \tag{2.21}$$

This expression can be rearranged by noting the property of the inverse of a product of operators:

$$\begin{aligned} \hat{B}^{-1} \hat{A}^{-1} &= (\hat{A} \hat{B})^{-1} \\ (1 - \hat{G}_0^+ \hat{V}_{int})^{-1} \hat{G}_0^+ &= [(E - \hat{H}_0)(1 - \hat{G}_0^+ \hat{V}_{int})]^{-1} \\ &= [E + i\epsilon - \hat{H}_0 - \hat{V}_{int}]^{-1} \\ &= [E + i\epsilon - \hat{H}]^{-1} \\ &= \hat{G}^+(E), \end{aligned} \tag{2.22}$$

where $\hat{G}^+(E)$ is the full Green's function. Then the full scattering wavefunction is given by

$$\Psi^+(E) = [1 + \hat{G}^+(E) \hat{V}_{int}] \phi. \tag{2.23}$$

Note that the ϕ term gives the proper solution in the case where $\hat{V}_{int} = 0$. In a general case ϕ will describe reactants in a specific quantum state n, and also depend on the energy, so more proper notation is $\phi_n(E)$. Then the full scattering wavefunction for reaction from state n of the reactants is given by

$$\Psi_n^+(E) = [1 + \hat{G}^+(E) \hat{V}_{int}] \phi_n(E). \tag{2.24}$$

2.2.2 S-matrix Elements

The scattering wavefunction, as an eigenstate of the Hamiltonian satisfying the proper boundary conditions, contains all the information necessary to obtain the S-matrix. Indeed, the the scattering operator[16] is defined such that its plane wave matrix elements are given by

$$\langle \phi_{n_p}(E') | \hat{S} | \phi_{n_r}(E) \rangle = \langle \Psi_{n_p}^-(E') | \Psi_{n_r}^+(E) \rangle \tag{2.25}$$

where $\Psi^-_{n_p}(E')$ is the scattering wavefunction for product state n_p with incoming wave boundary conditions:

$$\Psi^-_{n_p}(E') = [1 + \hat{G}^-(E')\,\hat{V}_{int}]\,\phi_{n_p}(E'). \tag{2.26}$$

Now we wish to consider overlap of the scattering wavefunctions at different energies.[20] Taking the adjoint of Eq. (2.26), this gives

$$\begin{aligned}\langle\Psi^-_{n_p}(E')|\Psi^+_{n_r}(E)\rangle &= \langle\phi_{n_p}(E')|[\hat{V}_{int}\,\hat{G}^+(E') + 1]|\Psi^+_{n_r}(E)\rangle \\ &= \langle\phi_{n_p}(E')|\hat{V}_{int}\,\hat{G}^+(E')|\Psi^+_{n_r}(E)\rangle + \langle\phi_{n_p}(E')||\Psi^+_{n_r}(E)\rangle\end{aligned} \tag{2.27}$$

However, we can make use of Eq. (2.18) to replace $\Psi^+_{n_r}(E)$ in the second term. Then we obtain

$$\begin{aligned}\langle\Psi^-_{n_p}(E')|\Psi^+_{n_r}(E)\rangle &= \langle\phi_{n_p}(E')|\phi_{n_r}(E)\rangle + \langle\phi_{n_p}(E')|\hat{V}_{int}\,\hat{G}^+(E')|\Psi^+_{n_r}(E)\rangle \\ &+ \langle\phi_{n_p}(E')|\hat{G}^+_0(E)\,\hat{V}_{int}|\Psi^+_{n_r}(E)\rangle.\end{aligned} \tag{2.28}$$

This can be simplified by noting that the Hamiltonian in $\hat{G}^+(E')$ can be acted on $\Psi^+_{n_r}(E)$ and the zeroth-order Hamiltonian in $\hat{G}^+_0(E)$ can be acted to the left onto $\phi_{n_p}(E')$. Doing this gives the result

$$\begin{aligned}\langle\Psi^-_{n_p}(E')|\Psi^+_{n_r}(E)\rangle &= \langle\phi_{n_p}(E')|\phi_{n_r}(E)\rangle + \langle\phi_{n_p}(E')|\hat{V}_{int}|\Psi^+_{n_r}(E)\rangle\left\{\frac{1}{E' - E + i\epsilon}\right\} \\ &+ \langle\phi_{n_p}(E')|\hat{V}_{int}|\Psi^+_{n_r}(E)\rangle\left\{\frac{1}{E - E' + i\epsilon}\right\}.\end{aligned} \tag{2.29}$$

Combining the common terms and noting that

$$\frac{1}{E' - E + i\epsilon} + \frac{1}{E - E' + i\epsilon} = \frac{-2i\epsilon}{(E - E')^2 + \epsilon^2}, \tag{2.30}$$

is a prelimit delta function equal to $-2\pi i\,\delta(E - E')$ as $\epsilon \to 0^+$, gives

$$\langle\Psi^-_{n_p}(E')|\Psi^+_{n_r}(E)\rangle = \langle\phi_{n_p}(E')|\phi_{n_r}(E)\rangle - 2\pi i\langle\phi_{n_p}(E')|\hat{V}_{int}|\Psi^+_{n_r}(E)\rangle\,\delta(E - E'). \tag{2.31}$$

Since the asymptotic states are plane waves, this becomes

$$\begin{aligned}\langle\Psi^-_{n_p}(E')|\Psi^+_{n_r}(E)\rangle &= \delta_{n_p,n_r}\,\delta(E - E') - 2\pi i\langle\phi_{n_p}(E')|\hat{V}_{int}|\Psi^+_{n_r}(E)\rangle\,\delta(E - E'), \\ &= S_{n_p,n_r}(E)\,\delta(E - E'),\end{aligned} \tag{2.32}$$

where $S_{n_p,n_r}(E)$ is the "on-shell" S-matrix. This illustrates the conservation of energy and naturally, one always calculates the S-matrix for initial and final states with the same total energy. One normally defines a transition operator, $\hat{T}$, such that

$$\hat{V}_{int}|\Psi^+_{n_r}(E)\rangle = \hat{T}|\phi_{n_r}(E)\rangle, \tag{2.33}$$

and it can be shown that

$$\hat{T} = \hat{V}_{int} + \hat{V}_{int}\hat{G}^+\hat{V}_{int}. \tag{2.34}$$

Then the S-matrix elements are given by

$$S_{n_p,n_r}(E) = \delta_{n_p,n_r} - 2\pi i\langle\phi_{n_p}(E)|\hat{V}_{int} + \hat{V}_{int}\,\hat{G}^+(E)\,\hat{V}_{int}|\phi_{n_r}(E)\rangle. \tag{2.35}$$

This can be written in an alternate form by noting that

$$\begin{aligned}(\hat{H}_0 - E)|\phi_{n_r}(E)\rangle &= 0\\ (\hat{H}_0 + \hat{V}_{int} - E)|\phi_{n_r}(E)\rangle &= \hat{V}_{int}|\phi_{n_r}(E)\rangle\\ (\hat{H} - E)|\phi_{n_r}(E)\rangle &= \hat{V}_{int}|\phi_{n_r}(E)\rangle,\end{aligned} \tag{2.36}$$

and similarly for the product asymptotic state. Then, the S-matrix elements are given by

$$S_{n_p,n_r}(E) = \delta_{n_p,n_r} - 2\pi i\langle\phi_{n_p}(E)|(\hat{H} - E) + (\hat{H} - E)\,\hat{G}^+(E)\,(\hat{H} - E)|\phi_{n_r}(E)\rangle. \tag{2.37}$$

At this point, we note that this expression can be obtained in a more general case than we have considered here. In the distorted wave representation, the asymptotic wavefunctions can be chosen to be more sophisticated than plane waves, in which case the S-matrix elements can be expressed as (with a slightly different normalization convention for the asymptotic wavefunctions which only affects the factor of $-2\pi i$)

$$S_{n_p,n_r}(E) = S^0_{n_p,n_r}(E) + \frac{i}{\hbar}\left[\langle\Phi_{n_p}\,|\,\hat{H} - E\,|\,\Phi_{n_r}\rangle + \langle(\hat{H} - E)\,\Phi_{n_p}\,|\,\hat{G}^+(E)\,|\,(\hat{H} - E)\,\Phi_{n_r}\rangle\right]. \tag{2.38}$$

Here, Φ_n is *any* (regular) scattering wavefunction with a unit incoming wave in channel n and outgoing waves in all other open channels n'

$$\Phi_n(\mathbf{r}, R) \sim -\frac{e^{-ik_nR}}{v_n^{1/2}}\,\phi_n(\mathbf{r}) + \sum_{n'}\frac{e^{ik_{n'}R}}{v_{n'}^{1/2}}\,\phi_{n'}(\mathbf{r})\;S^0_{n',n}. \tag{2.39}$$

($\mathbf{r}$ in Eq. (2.39) denotes all coordinates of the system other than that for relative translation, R, and $\{\phi_n(\mathbf{r})\}$ the asymptotic channel eigenfunctions; v_n is the translational velocity for channel n.) As is evident from Eq. (2.39), $S^0_{n_p,n_r}$ is the scattering amplitude between asymptotic states n_p and n_r that is already included in the distorted wave Φ_{n_r}. Thus, it is seen that Eq. (2.37) is a special case of Eq. (2.39) in which $S^0_{n_p,n_r}$ is chosen to be δ_{n_p,n_r}.

The distorted wave representation is extremely useful as it allows one to take advantage of any knowledge of the scattering wavefunction. The asymptotic waves, Φ_{n_p} and Φ_{n_r} can contain any level of scattering information, elastic, inelastic, or even reactive. The simplest choice is to take the distorted wave to be

$$\Phi_n(\mathbf{r},R) = -\frac{e^{-ik_nR}}{v_n^{1/2}}\,\phi_n(\mathbf{r}), \tag{2.40}$$

for which

$$S^0_{n',n} = 0. \tag{2.41}$$

This is really an "undistorted wave" containing no scattering information. Elastic scattering information can be incorporated into an *elastically distorted* wave by choosing

$$\Phi_n(\mathbf{r},R) \sim -\frac{e^{-ik_nR}}{v_n^{1/2}}\,\phi_n(\mathbf{r}) + \frac{e^{ik_nR}}{v_n^{1/2}}\,\phi_n(\mathbf{r})\,S^0_{n,n}. \tag{2.42}$$

Similarly an *inelastically distorted* wave can be used by choosing

$$S^0_{n',n} = 0, \tag{2.43}$$

in Eq. (2.42) only for n and n' of different chemical arrangements. Reactive distorted waves can also be used as will be discussed below.

2.2.3 DVR-ABC Formulation

In a basis set representation such as a DVR the S-matrix is given by (with matrices and vectors represented in boldface)

$$\begin{aligned} S_{n_p,n_r}(E) &= S^0_{n_p,n_r}(E) + \frac{i}{\hbar}\,[\mathbf{\Phi}^T_{n_p}\cdot(\mathbf{H}-E\mathbf{I})\cdot\mathbf{\Phi}_{n_r} && (2.44)\\ &+ \mathbf{\Phi}^T_{n_p}\cdot(\mathbf{H}-E\mathbf{I})\cdot\mathbf{G}^+(E)\cdot(\mathbf{H}-E\mathbf{I})\cdot\mathbf{\Phi}_{n_r}]. && (2.45)\end{aligned}$$

The difficulty here is that the Green's function and the asymptotic waves are nonzero out to infinity in the reactant and product valleys. This cannot be treated with a finite basis representation. What is needed is a way to turn the problem into a psuedo-bound state problem which can be treated by typical L^2 approaches. One way to accomplish this is by using absorbing boundary conditions. As discussed above, the Green's function is formally defined as

$$\hat{G}^{+}(E) = \lim_{\epsilon \to 0^{+}} (E - \hat{H} + i\epsilon)^{-1}, \tag{2.46}$$

where the $i\epsilon$ serves to impose the outgoing wave boundary conditions. If ϵ is allowed to become a function of position such that it is zero in the interaction region but turns on moving out in the reactant and product valleys it also serves to make the Green's function localized. The Green's function now dies off to zero as the "absorbing potential" increases in the entrance and exit valleys but the correct behavior is maintained in the interaction region. We refer to the use of ϵ in the Green's function in the this manner as absorbing boundary conditions.

We note that the discrete variable representation, and other grid point methods, has been developed and used by many persons,[21–37] with the work of Light and co-workers[38–40] being particularly important in recent years. This idea of adding a negative imaginary potential to the Hamiltonian (or alternatively adding a positive imaginary component to the energy) has been used in many time-dependent[41–47] and time-independent[48–57] methods. In time-dependent wavepacket approaches, absorbing potentials (often referred to as negative imaginary potentials (NIPS), complex absorbing potentials (CAPS), or empirical optical potentials) are placed at the asymptotic edges of the finite basis representation so that outgoing flux will be absorbed and not reflected back to intefere with the true dynamics. The DVR-ABC formalism refers to the representation of the outgoing wave Green's function within a DVR and by including a negative imaginary potential and the scattering relations that result.

Using absorbing boundary conditions we can transform the expression for the S-matrix into a more useful form, taking advantage of the L^2 nature of the Green's function. Including this position-dependent absorbing potential, the Green's function

satisfies the relation

$$(E\mathbf{I} - \mathbf{H} + i\boldsymbol{\epsilon}) \cdot \mathbf{G}^{+}(E) = \mathbf{I}, \tag{2.47}$$

where we have noted that $\epsilon \rightarrow \hat{\epsilon}$ is now an operator. Dividing the Green's function into real and imaginary parts, $\mathbf{G} = \mathbf{G}_r + i\mathbf{G}_i$, we obtain equations relating the two:

$$(\mathbf{H} - E\mathbf{I}) \cdot \mathbf{G}_i = \boldsymbol{\epsilon} \cdot \mathbf{G}_r, \tag{2.48}$$

and

$$(\mathbf{H} - E\mathbf{I}) \cdot \mathbf{G}_r = -\mathbf{I} - \boldsymbol{\epsilon} \cdot \mathbf{G}_i. \tag{2.49}$$

Taking the transpose of these equations, noting that $\mathbf{G}_i, \mathbf{G}_r, \mathbf{H}$, and $\boldsymbol{\epsilon}$ are symmetric matrices gives

$$\mathbf{G}_i \cdot (\mathbf{H} - E\mathbf{I}) = \mathbf{G}_r \cdot \boldsymbol{\epsilon}, \tag{2.50}$$

and

$$\mathbf{G}_r \cdot (\mathbf{H} - E\mathbf{I}) = -\mathbf{I} - \mathbf{G}_i \cdot \boldsymbol{\epsilon}. \tag{2.51}$$

Using these equalities to evaluate the matrix elements of $(\hat{H} - E)\,\hat{G}\,(\hat{H} - E)$ yields

$$(\mathbf{H} - E\mathbf{I}) \cdot \mathbf{G}_r \cdot (\mathbf{H} - E\mathbf{I}) = -(\mathbf{H} - E\mathbf{I}) - \boldsymbol{\epsilon} \cdot \mathbf{G}_r \cdot \boldsymbol{\epsilon}, \tag{2.52}$$

for the real part of the Green's function and

$$(\mathbf{H} - E\mathbf{I}) \cdot \mathbf{G}_i \cdot (\mathbf{H} - E\mathbf{I}) = -\boldsymbol{\epsilon} - \boldsymbol{\epsilon} \cdot \mathbf{G}_i \cdot \boldsymbol{\epsilon}, \tag{2.53}$$

for the contribution of the imaginary part. Substituting these equations into the expression for the S-matrix in the DVR gives

$$S_{n_p,n_r}(E) = S^0_{n_p,n_r}(E) - \frac{i}{\hbar}\left[\boldsymbol{\Phi}^T_{n_p} \cdot \boldsymbol{\epsilon} \cdot \boldsymbol{\Phi}_{n_r} + \boldsymbol{\Phi}^T_{n_p} \cdot \boldsymbol{\epsilon} \cdot \mathbf{G}^{+}(E) \cdot \boldsymbol{\epsilon} \cdot \boldsymbol{\Phi}_{n_r}\right]. \tag{2.54}$$

where $\boldsymbol{\Phi}_n$ is the following DVR vector in grid point space

$$(\boldsymbol{\Phi}_{\mathbf{n}})_j = w_j^{1/2}\, \Phi_n(\mathbf{q}_j), \tag{2.55}$$

$\mathbf{q}$ denotes all coordinates, and $\mathbf{q}_j$ and w_j are the (multidimensional) grid points and DVR weights, respectively.

This is the fundamental expression for the S-matrix in the DVR-ABC formalism of scattering theory. Typically, the distorted (or asymptotic) waves are chosen such that they are nonzero only in the given arrangement, *i.e.*, $\mathbf{\Phi}_{n_r} = 0$ in the product arrangement and $\mathbf{\Phi}_{n_p} = 0$ in the reactant arrangement, *i.e.*, nonreactive distorted waves are chosen. Then the first two terms in Eq. (2.54) are zero and S-matrix is given by

$$S_{n_p,n_r}(E) = -\frac{i}{\hbar}\, \mathbf{\Phi}^T_{n_p} \cdot \boldsymbol{\epsilon}_p \cdot \mathbf{G}^+(E) \cdot \boldsymbol{\epsilon}_r \cdot \mathbf{\Phi}_{n_r}, \tag{2.56}$$

where we have noted that $\boldsymbol{\epsilon} \cdot \mathbf{\Phi}_{n_r} = \boldsymbol{\epsilon}_r \cdot \mathbf{\Phi}_{n_r}$ if $\mathbf{\Phi}_{n_r}$ is a nonreactive distorted wave, and similarly for the distorted wave in the product arrangement. Also, the zeroth order contribution to the reactive S-matrix is zero, ($S^0_{n_p,n_r}(E) = 0$) if nonreactive distorted waves are used.

The initial state-selected reaction probability is given as the sum over product quantum states of the state-to-state reaction probabilities:

$$P_{n_r}(E) = \sum_{n_p} |S_{n_p,n_r}(E)|^2. \tag{2.57}$$

Using the expression we just derived for the S-matrix elements in the DVR-ABC formulation this gives

$$P_{n_r}(E) = \sum_{n_p} \mathbf{\Phi}^T_{n_r} \cdot \boldsymbol{\epsilon}_r \cdot \mathbf{G}^+(E)^* \cdot \boldsymbol{\epsilon}_p \cdot \mathbf{\Phi}_{n_p}\, \mathbf{\Phi}^T_{n_p} \cdot \boldsymbol{\epsilon}_p \cdot \mathbf{G}^+(E) \cdot \boldsymbol{\epsilon}_r \cdot \mathbf{\Phi}_{n_r}, \tag{2.58}$$

where we have noted that $\mathbf{G}^+(E)$ is a complex-symmetric matrix. This equation can be made useful by means of the identity

$$(2\hbar)^{-1} \sum_{n_p} \boldsymbol{\epsilon}_p \cdot \mathbf{\Phi}_{n_p} \mathbf{\Phi}^{T*}_{n_p} \cdot \boldsymbol{\epsilon}_p = \boldsymbol{\epsilon}_p, \tag{2.59}$$

which is a completeness-like relation in the ABC formalism. An equivalent expression exists for the reactant wavefunctions and absorbing potentials.

In the following, we derive this Eq. (2.59). The starting point is two operator identities involving the microcanonical density operator, $\delta(E - \hat{H})$:

$$\delta(E - \hat{H}) = -\frac{1}{\pi} \mathrm{Im}\, \hat{G}^+(E) \tag{2.60}$$

$$\delta(E - \hat{H}) = \sum_n \rho\, |\, \Psi_n(E)\, \rangle \langle\, \Psi_n(E)\, |, \tag{2.61}$$

where $\Psi_{E,n}$ is the exact scattering wavefunction. $\rho = (2\pi\hbar)^{-1}$ is a density of states factor related to the normalization of the translational part of the scattering wavefunction. A Lippmann-Schwinger-type equation for $\Psi_{E,n}$ in terms of the zeroth order scattering wavefunction Φ_n can be obtained of the form

$$\begin{aligned}\Psi_n(E) &= [1 + \hat{G}^+(E)(\hat{H} - E)]\,\Phi_n \\ &= \hat{G}^+(E)(E - \hat{H} + i\hat{\epsilon} + \hat{H} - E)\,\Phi_n \\ &= \hat{G}^+(E)\,i\hat{\epsilon}\,\Phi_n. \end{aligned} \tag{2.62}$$

This is a well-known result for the case where ϵ is a positive constant, but we note that it also applies in the more general case that $\hat{\epsilon}$ is an operator. (Though now one has to be aware that $\hat{\epsilon}$ and $\hat{G}^+(E)$ do not commute.) Using this expression in Eq. (2.61), and putting this into a DVR gives

$$\delta(E - \mathbf{H}) = (2\pi\hbar)^{-1} \sum_n \mathbf{G}^+(E) \cdot \boldsymbol{\epsilon} \cdot \boldsymbol{\Phi}_n \, \boldsymbol{\Phi}_n^{T*} \cdot \boldsymbol{\epsilon} \cdot \mathbf{G}^+(E)^*. \tag{2.63}$$

The right-hand side of this equation is of the form we have obtained in the expression for the initial state-selected reaction probabilities above. Now we need to relate this to a more convenient and compact form. Turning to Eq. (2.60), one has

$$\begin{aligned}\mathrm{Im}\,\hat{G}^+(E) &= \mathrm{Im}\,(E + i\hat{\epsilon} - \hat{H})^{-1}\,(E - i\hat{\epsilon} - \hat{H})\,(E - i\hat{\epsilon} - \hat{H})^{-1}, \\ &= -\hat{G}^+\,\hat{\epsilon}\,\hat{G}^+(E)^*, \end{aligned} \tag{2.64}$$

the DVR of which combined with Eq. (2.60) is

$$\delta(E - \mathbf{H}) = \frac{1}{\pi}\,\mathbf{G}^+(E) \cdot \boldsymbol{\epsilon} \cdot \mathbf{G}^+(E)^*. \tag{2.65}$$

Equating Eqs. (2.63) and (2.65) results in the closure relation in Eq. (2.59).

If we use the closure relation in Eq. (2.59) for the initial state-selected reaction probability then we obtain

$$P_{n_r}(E) = \frac{2}{\hbar}\,\boldsymbol{\Phi}_{n_r}^{T*} \cdot \boldsymbol{\epsilon}_r \cdot \mathbf{G}^+(E)^* \cdot \boldsymbol{\epsilon}_p \cdot \mathbf{G}^+(E) \cdot \boldsymbol{\epsilon}_r \cdot \boldsymbol{\Phi}_{n_r}. \tag{2.66}$$

Note that a similar expression holds for the final state-selected reaction probability,

$$P_{n_p}(E) = \frac{2}{\hbar}\,\boldsymbol{\Phi}_{n_p}^{T*} \cdot \boldsymbol{\epsilon}_p \cdot \mathbf{G}^+(E)^* \cdot \boldsymbol{\epsilon}_r \cdot \mathbf{G}^+(E) \cdot \boldsymbol{\epsilon}_p \cdot \boldsymbol{\Phi}_{n_p}, \tag{2.67}$$

which is the probability of ending up in product quantum state n_p when the reactants have been prepared in a microcanonical ensemble. At first this result may not seem any simpler to calculate than an S-matrix element. Indeed, both require the operation of the Green's function operation onto a single vector (the asymptotic wavefunction). However, the state-selected probability is easier to obtain because the basis does not need to be extended as far out in the product valley as for the calculation of the S-matrix element. This results from the physics of the problem. That is, while overall reactivity is determined a localized area around the interaction region, the detailed aspects about state-specific reactivity and product state distributions is not determined until further out towards the asymptotic valleys.

The same closure relation of Eq. (2.59) relates the initial state-selected reaction probability to the cumulative reaction probability,

$$N(E) = \sum_{n_r} P_{n_r}(E) = \sum_{n_p,n_r} |S_{n_p,n_r}|^2. \tag{2.68}$$

A direct expression for N(E) has been obtained by Seideman and Miller[9]

$$N(E) = 4\,\mathrm{tr}[\mathbf{G}^+(E)^* \cdot \boldsymbol{\epsilon}_p \cdot \mathbf{G}^+(E) \cdot \boldsymbol{\epsilon}_r], \tag{2.69}$$

within the DVR-ABC formalism as adapted from the result of Miller, Schwartz, and Tromp.[58] This expression has been used for many systems including the H + H_2,[9,10,59] H + O_2,[60] OH + H_2,[61,62] and ketene isomerization[63] reactions as well as gas-surface scattering.[64,65] Of particular note is the development by Manthe and Miller[12] of a remarkably efficient method for evaluating the quantum mechanical trace in Eq. (2.69).

2.3 The Collinear H + H_2 Reaction

The collinear H + H_2 → H_2 + H exchange reaction is a two-dimensional problem which provides a good first test of a state-specific scattering method. Unlike a one-dimensional system, meaningful (vibrational) state-selected quantities can be calculated, but without the computational difficulty of a full three-dimensional scattering problem.

The potential energy surface used for this reaction is the Liu-Siegbahn-Truhlar-Horowitz (LSTH) surface which is an analytical fit[66,67] by Truhlar and Horowitz to the *ab initio* calculations of Liu and Siegbahn.[68] This is a full three degree of freedom surface which we constrain to the collinear configuration for these calculations. The barrier height is 0.425 eV and is symmetrically located with a collinear transition state. The mass of the hydrogen atom is taken as 1837.151 atomic units.

There are multiple coordinate systems which are appropriate for the treatment of this problem. These include Jacobi coordinates (of the reactant or product arrangement), normal mode coordinates of the transition state, and valence bond coordinates. The present calculations have been carried out in the reactant Jacobi coordinates, (R, r), and in the normal mode coordinates of the transition state, (q_1, q_2); neither coordinate system has a distinct advantage over the other for this case. Note that in this two-dimensional case the Jacobi coordinates, like the normal coordinates, are Cartesian and therefore $-\infty < r, R < \infty$. In addition, the two sets of coordinates are related to by a simple linear transformation (rotation):

$$\begin{aligned} r &= q_1 + \frac{1}{2}q_2, \\ R &= \frac{3}{2}q_1 - \frac{1}{4}q_2, \\ &\Updownarrow \\ q_1 &= \frac{1}{2}R + \frac{1}{4}r, \\ q_2 &= -R + \frac{3}{2}r. \end{aligned} \tag{2.70}$$

In turn, these coordinates are related to the bond distances by

$$\begin{aligned} r_1 &= r, \\ r_2 &= R - \frac{1}{2}r, \end{aligned} \tag{2.71}$$

and

$$\begin{aligned} r_1 &= q_1 + \frac{1}{2}q_2, \\ r_2 &= q_1 - \frac{1}{2}q_2. \end{aligned} \tag{2.72}$$

The primary advantage of these coordinates (vs. valence bond coordinates, for example) is that the kinetic energy operator is separable.

In the present discussion we will concentrate for the most part on the normal coordinates while pointing out any differences with the use of Jacobi coordinates. The Hamiltonian is given by

$$\hat{H} = -\frac{\hbar^2}{2\mu_1}\frac{\partial^2}{\partial q_1^2} - \frac{\hbar^2}{2\mu_2}\frac{\partial^2}{\partial q_2^2} + V(r,R), \tag{2.73}$$

where the translational and vibrational reduced masses are

$$\begin{aligned} \mu_1 &= 2m_H, \\ \mu_2 &= \frac{m_H}{6}, \end{aligned} \tag{2.74}$$

respectively.

We have chosen to use a discrete variable representation as the finite basis. Specifically we use the $(-\infty, +\infty)$ sinc-function DVR of Colbert and Miller.[37] This choice for the basis has multiple advantages: (1) the kinetic energy matrix elements are given in closed form, (2) no multidimensional integrals of the potential need to be evaluated numerically since the potential matrix is approximated as diagonal (with a given diagonal element equal to the potential evaluated at that DVR grid point), and (3) the Hamiltonian matrix is sparse for a multidimensional case such as this.

The absorbing potentials in the reactant and product regions, ϵ_r and ϵ_p, are taken to be a function of the translational Jacobi coordinate for each arrangement; *i.e.*,

$$\epsilon_\tau(q_1, q_2) = \epsilon(R_\tau(q_1, q_2)), \tag{2.75}$$

for $\tau = r$ (reactants) or p (products), where R_r and R_p are functions of the transition state normal coordinates (q_1, q_2). For all calculations in this paper, the absorbing potential has been taken to be a quartic function, beginning at R_0 and ending at R_{max},

$$\epsilon_\tau(R_\tau) = \lambda \left(\frac{R_\tau - R_0}{R_{max} - R_0}\right)^4, \tag{2.76}$$

though we note that other functional forms work essentially as well.

2.3.1 State-to-State Reaction Probability

We have calculated the state-to-state S-matrix elements for the collinear H + H_2 reaction in the DVR-ABC formalism using Eq. (2.56). The calculation is carried out as follows. First a DVR grid (basis) is chosen; for a sinc-function DVR this means specifying the spacing between grid points. The density of the DVR grid points is specified by the grid constant, N_B, which is the number of points per deBroglie wavelength. This is related to the spacing between points, Δq, by $N_B = 2\pi/k\,\Delta q$ where $k = (2mE/\hbar^2)^{1/2}$. Typically N_B is on the order of 4, relatively independent of the system being treated. This can be thought of as a basic guideline - four points are required to represent one period of the wave. A direct product grid in the two coordinates, R and r (or q_1 and q_2) is laid out and then truncated according to two criteria: (1) In the product and reactant asymptotic valleys, the grid is truncated at the boundaries of the absorbing potentials. Namely, a grid point in arrangement τ is discarded if the value of the translational Jacobi coordinate of that arrangement, R_τ, is larger than a specified value, R_{max}. (2) The grid is truncated according to an energy cuttoff. If the potential energy at a grid point is larger than a fixed value, V_{cut}. The assumption underlying this is that for V_{cut} chosen sufficiently large, the wavefunction will be zero at these points and therefore they do not need to be considered.

There are essentially three convergence parameters to consider in these calculations: (1) N_B must be large enough to properly represent the Green's function on the DVR grid; (2) V_{cut} must be large enough to include all physically relevant regions of the potential energy surface; and (3) R_{max} must be large enough for the absorbing potential to absorb all the outgoing flux without reflection.

A typical DVR grid in the transition state normal mode coordinates for a state-to-state calculation for the collinear H + H_2 reaction is shown in Figure 2.1 overlayed on the contour plot of the LSTH potential energy surface.[68,66,67] The contours of the quartic absorbing potential $\epsilon(\mathbf{q})$ are indicated by broken lines.

Once the basis set has been chosen, the matrix elements of the relevant operators can be evaluated. In the sinc-function DVR an analytical form for the

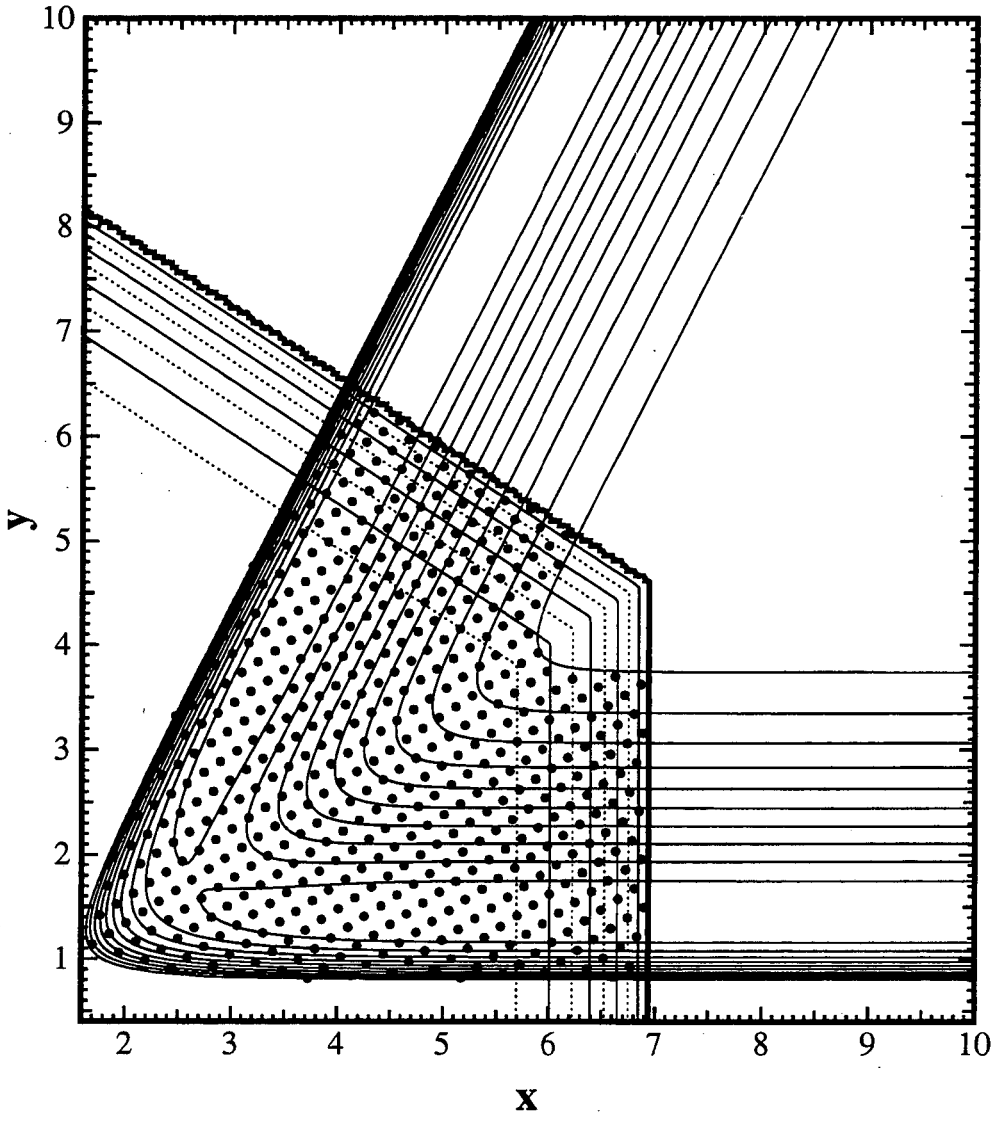

Figure 2.1: Contour plot of the LSTH potential energy surface. A typical DVR grid laid out in normal coordinates is shown as the filled circles. The dashed lines are the contours of the absorbing potential. x = R and y = $\sqrt{3}r/2$ are the mass-scaled Jacobi coordinates.

kinetic energy matrix elements exist and for the $(-\infty,\infty)$ version these are given by

$$\langle x_i| -\frac{\hbar^2}{2\mu}\frac{d^2}{dx^2}|x_{i'}\rangle = (\mathbf{T}_x)_{i,i'} = \frac{\hbar^2}{2\mu\Delta x^2}(-1)^{(i-i')}\left\{\begin{array}{ll}\pi^2/3, & i=i'\\ \frac{2}{(i-i')^2}, & i\neq i'\end{array}\right\}. \tag{2.77}$$

In addition, the matrix elements of the potential in a DVR are approximated as diagonal, with the diagonal elements equal to the potential evaluated at the corresponding DVR point. Thus, we have that

$$(\mathbf{V})_{i,i'} = V(x_i)\,\delta_{i,i'}, \tag{2.78}$$

and similarly for the absorbing potential,

$$(\boldsymbol{\epsilon})_{i,i'} = \epsilon(x_i)\,\delta_{i,i'}. \tag{2.79}$$

The Hamiltonian is thus formed in the DVR basis and the next step is to obtain the asymptotic state and solve the linear system

$$(E - \mathbf{H} + i\boldsymbol{\epsilon})\cdot\mathbf{x} = \boldsymbol{\epsilon}_r\cdot\boldsymbol{\Phi}_{n_r}, \tag{2.80}$$

to obtain

$$\mathbf{x} = \mathbf{G}^+(E)\cdot\boldsymbol{\epsilon}_r\cdot\boldsymbol{\Phi}_{n_r}, \tag{2.81}$$

with which the S-matrix elements $S_{n_p,n_r}(E)$ can be trivially computed.

The asymptotic wavefunction Φ_n can be chosen as any (regular) scattering wavefunction with a unit incoming wave in channel n and outgoing waves in all other open channels n' as shown in Eq. (2.39). We have chosen the asymptotic state to be an undistorted wave of the form (in the reactant Jacobi coordinates)

$$\Phi_n(\mathbf{r},R) = -\frac{e^{-ik_nR}}{v_n^{1/2}}\,\phi_n(\mathbf{r}), \tag{2.82}$$

Another, more conventional choice, would be the standing free wave

$$\begin{aligned}\Phi_n(\mathbf{r},R) &= -2i\,\frac{\sin k_nR}{v_n^{1/2}}\,\phi_n(\mathbf{r}) \\ &= \left[-\frac{e^{-ik_nR}}{v_n^{1/2}} + \frac{e^{ik_nR}}{v_n^{1/2}}\right]\phi_n(\mathbf{r}),\end{aligned} \tag{2.83}$$

which contains elastic distortion such that

$$S^0_{n',n} = \delta_{n',n}. \tag{2.84}$$

We have tried this form as well, but we find that the incoming wave in Eq. (2.82) leads to better convergence. We note that for the free or distorted incoming radial function it is not necessary to multiply it by a cutoff function to regularize it for small R (as is necessary in the Kohn variational approach[37]); this is because Φ_n is always multiplied by the reactant or product absorbing potential (*cf.* Eqs. (2.56) and (2.66)) which vanishes identically for small R.

In Figure 2.2 the present calculated state-to-state reaction probabilities for collinear H + H_2 are compared to benchmark results obtained by Bondi and Connor.[69] The agreement is excellent. The $v = 0 \rightarrow v' = 0$ reaction probability displays a threshold to reaction at approximately 0.55 eV. As mentioned above, the bare barrier is 0.425 eV and the 0.125 eV of zero point energy in the symmetric stretch mode at the transition state is responsible for the difference. Note that there is a significant amount of tunneling below this threshold energy as well as reflection at energies above it, as is typical for a quantum mechanical reaction over a barrier. After reaching maximum around 0.6 eV, the reaction probability slowly becomes smaller as elastic scattering is more important at higher translational energies. Two prominent (and well known) resonances are observed at 0.89 and 1.29 eV (near the energies of the $v = 1$ and $v = 2$ states). These are Feshbach resonances due to vibrational nonadiabaticity. Due to changes in the adiabatic zero point energy along the reaction path, a higher vibrational state (which asymptotically is a closed channel) can be accessed in the region of the transition state. A transition to such a state results in a (relatively) long-lived resonance before a transition can be made back to the lower state and the fragments can separate to give reactants or products. The resonances at 0.89 and 1.29 eV have lifetimes of about 16 and 22 fs, respectively. The $v = 0 \rightarrow v' = 1$ (which is equal to $P_{1,0}$) and $v = 1 \rightarrow v' = 1$ probabilities display resonances at the same energies. For the calculations shown in Fig. 2.2, we used $R_{max} = 6.9$ a.u., $N_B = 3.7$, and $V_{cut} = 4.1$ eV resulting in at grid of 546 points at 1.0 eV.

Figure 2.3 illustrates the convergence of the reactive state-to-state probabil-

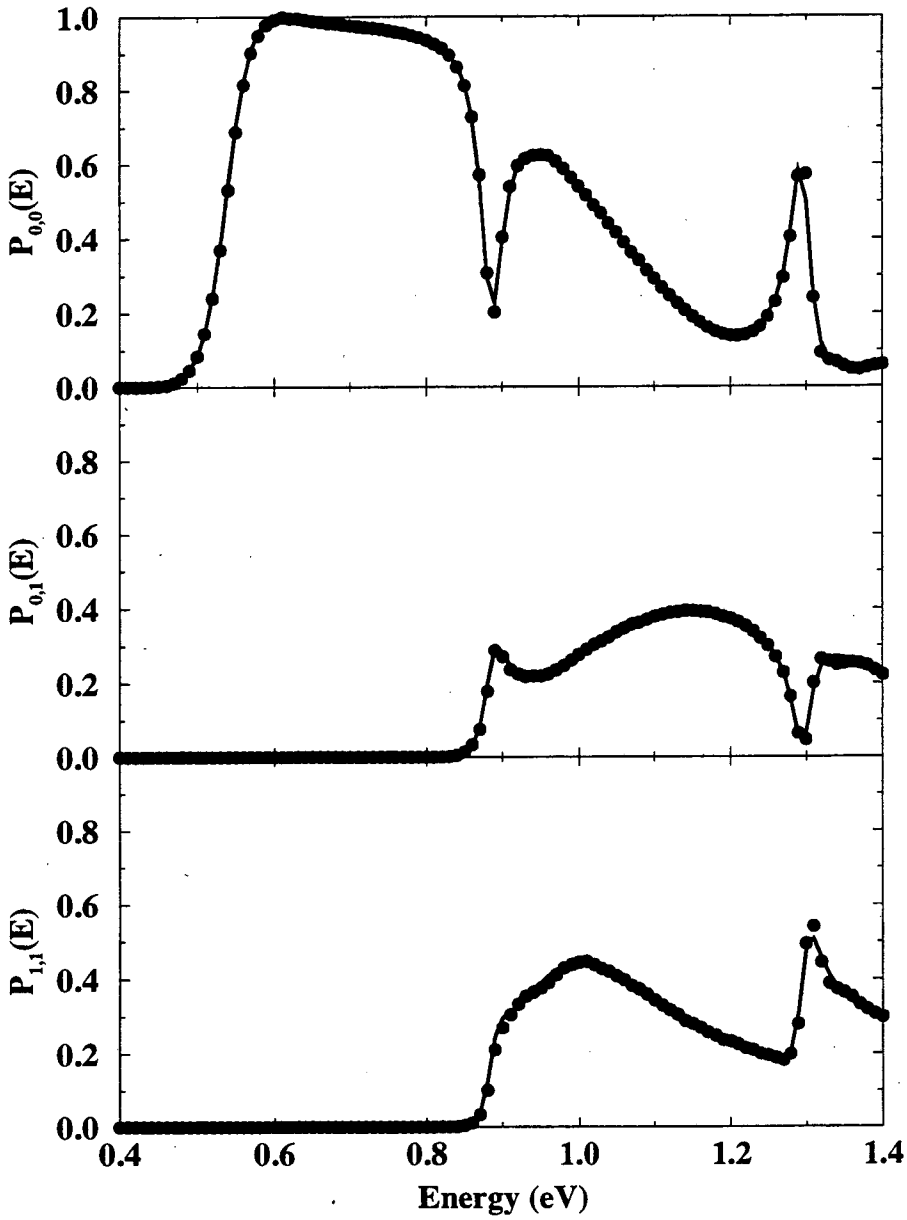

Figure 2.2: State-to-state reaction probabilities, $P_{0,0}(E)$, $P_{0,1}(E)$, and $P_{1,1}(E)$, for the collinear H + H_2 reaction calculated with the DVR-ABC Green's function (filled circles) compared with the results of Bondi and Connor (Ref. 69) shown as the solid line.

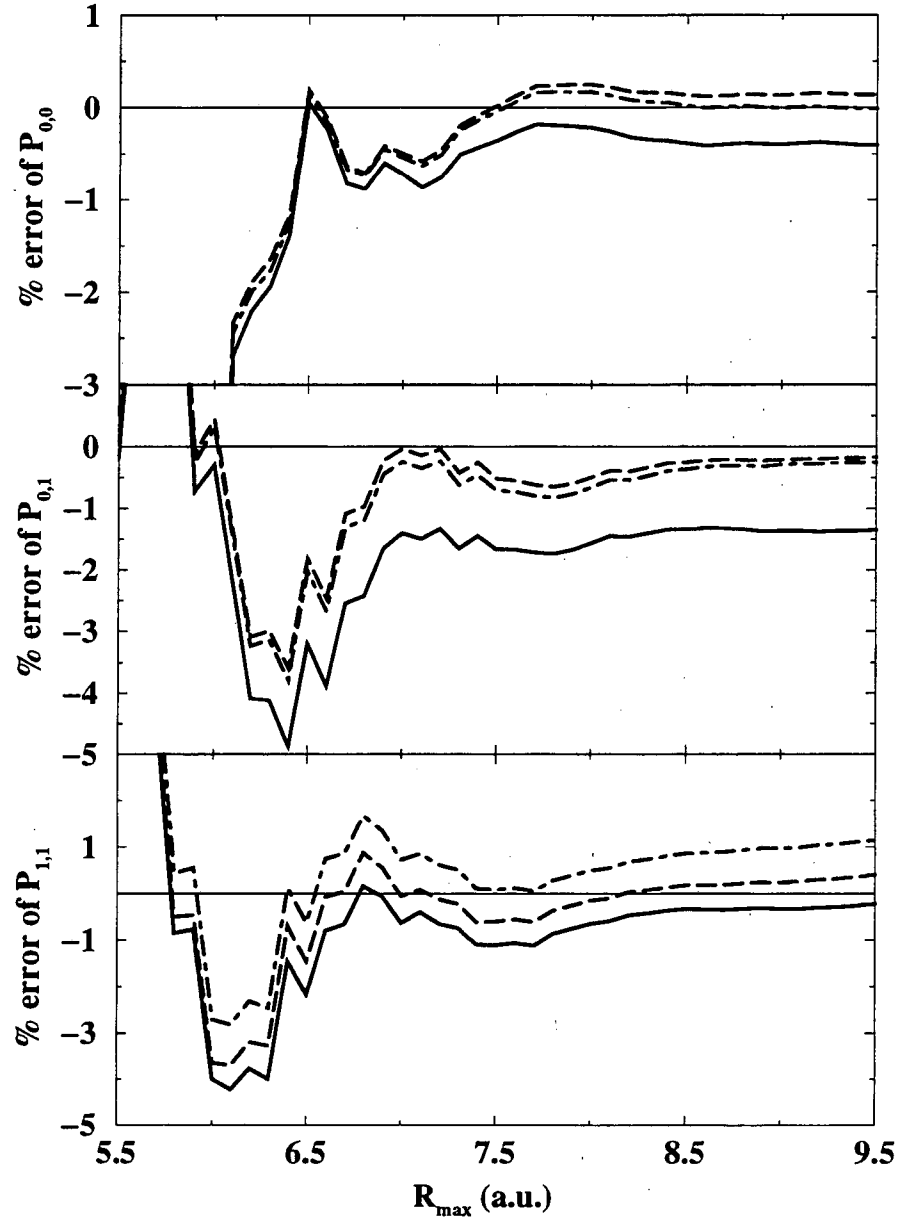

Figure 2.3: Percent error in the calculated state-to-state reaction probabilities as a function of the extent of the grid, R_{max} at E = 1.0 eV. Results are shown for different values of V_{cut}: the thick solid line has V_{cut} = 3.0 eV, the dashed-dot line V_{cut} = 4.0 eV, and the long-dashed line V_{cut} = 5.0 eV. The thin solid line marks zero percent error. The error is calculated relative to the results of Bondi and Connor (Ref. 69).

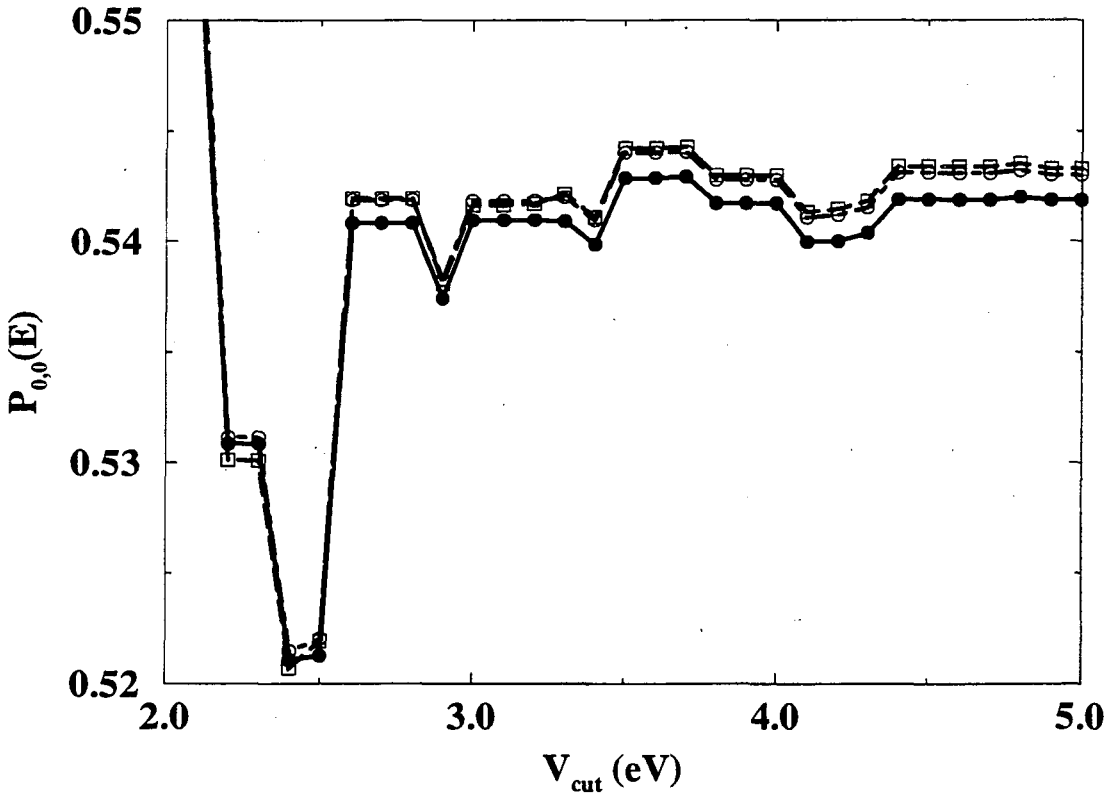

Figure 2.4: Calculated state-to-state reaction probabilities as a function of the extent of the cuttoff energy, V_{cut} at E = 1.0 eV. Results are shown for different values of R_{max}: the thick solid line and filled circles has R_{max} = 6.8 a.u., the dashed-dot line and open circles R_{max} = 7.0 a.u., and the long-dashed line and open squares R_{max} = 7.2 a.u.

ities at a total energy of 1.0 eV as the size of the grid, R_{max} is increased, for different values of V_{cut}. (The percent error is calculated by comparison to the results of Bondi and Connor.[69]) At this energy the $v = 0$ and 1 vibrational states are open channels. Agreement with the exact answer to within 3% can be obtained with R_{max} = 6.7 a.u., V_{cut} = 3.0 eV and 421 DVR points; as noted above, 1% error can be attained with about 120 more points.

The dependence of the $v = 0$ to $v' = 0$ reaction probability the cuttoff energy is shown in Figure 2.4 for R_{max} equal to 6.8, 7.0, and 7.2 a.u for E = 1.0 eV. For reference, the reaction probability obtained by Bondi and Connor is 0.546 at

this energy. Note that the reaction probability displays a large oscillation at low V_{cut} but is relatively stable above $V_{cut} = 2.6$ eV. In fact, $P_{0,0}$ is converged to within 2% above this value of V_{cut} while the other probabilities ($P_{0,1}$ and $P_{1,1}$) are within 6% of the exact answer. For the two larger values of R_{max}, all the reaction probabilities are converged to 1% error for $V_{cut} = 3.5$ eV (and within 2% for $R_{max} = 6.8$). As discussed above, the truncation of the DVR grid by an energy cuttoff assumes that the wavefunction is zero at grid points where the potential energy is larger than V_{cut}. From Fig. 2.4, one would infer that the scattering wavefunction at total energy 1.0 eV has little amplitude outside the area where the potential is less than 2.6 eV.

2.3.2 Initial State-Selected Reaction Probabilities

For computing the total reaction probability for a given initial reactant state (*via* Eq. (2.66)), the DVR grid was again laid down in the normal mode coordinates of the transition state as shown in Figure 2.5. The absorbing potentials ϵ_r and ϵ_p were chosen as above, Eq. (2.75)-(2.76), though now the parameters R_0 and R_{max} are different for the reactant and product absorbing potentials. Since no state-specific information is being obtained about the products, the product absorbing potential can be brought in much closer to the transition state. Indeed, while the reactant absorbing potential remains essentially the same as in the state-to-state case, the product absorbing potential can be brought in close to the interaction region as in a calculation of the cumulative reaction probability.[9,10]

Since the savings in calculating the initial state-selected rather than the state-to-state reaction probabilities is realized because the product absorbing potential no longer needs to extend as far into the exit valley, an important question then becomes, How close can the product absorbing potential be to the interaction region? Figure 2.6 shows the convergence for $E = 1.0$ eV with respect to $R_{p,max}$, the end of the grid in the product valley. Recall that for the state-to-state probabilities the grid was truncated in the asymptotic valleys with $R_{max} = 6.9$ a.u. to obtain 1% error. Here, the same level of accuracy is realized when the product absorbing strip ends at $R_{p,max} = 5.0$ a.u. corresponding to a grid of 358 DVR points. For these calculations,

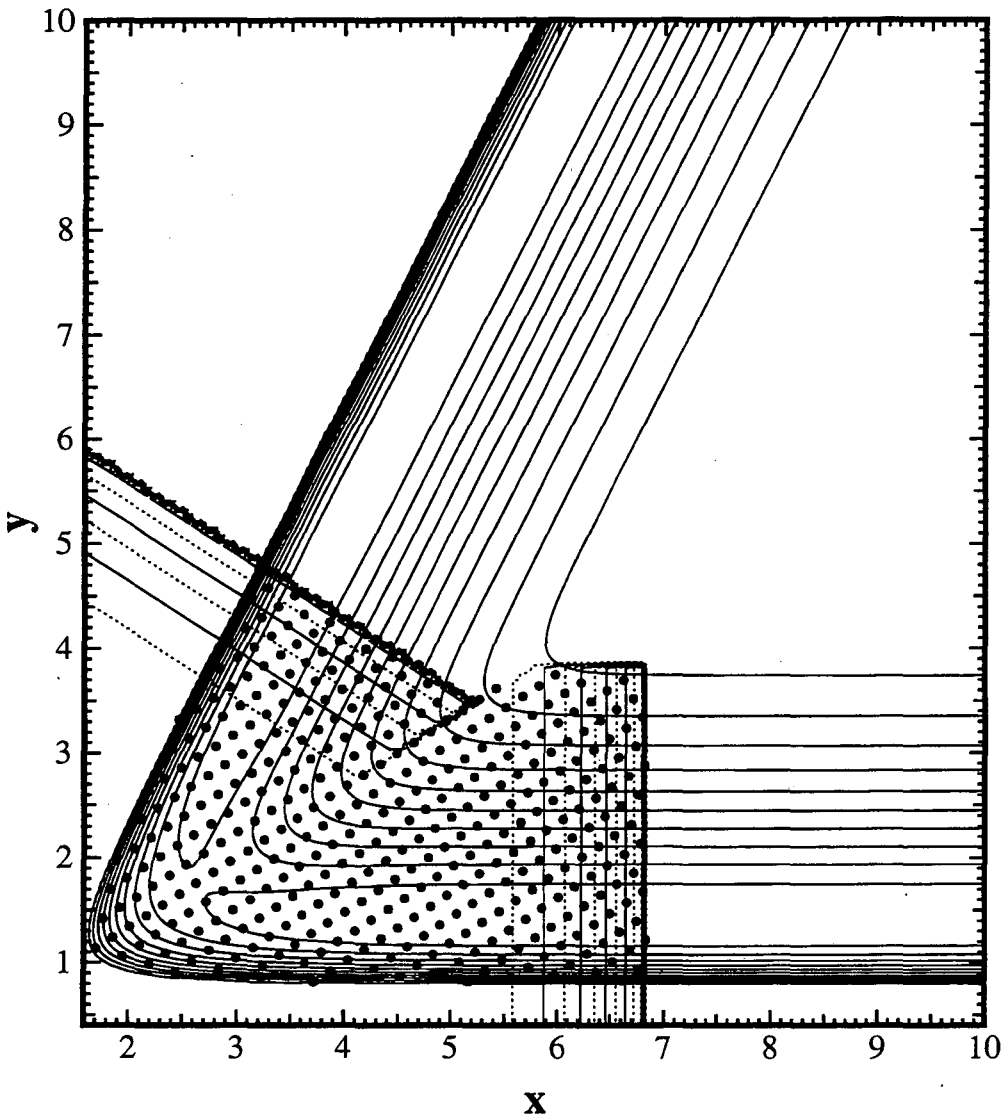

Figure 2.5: Contour plot of the LSTH potential energy surface overlayed with a DVR grid (shown as the filled circles) laid out in normal coordinates for a typical initial state-selected calculation. The dashed lines are the contours of the absorbing potential. x = R and y = $\sqrt{3}r/2$ are the mass-scaled Jacobi coordinates.

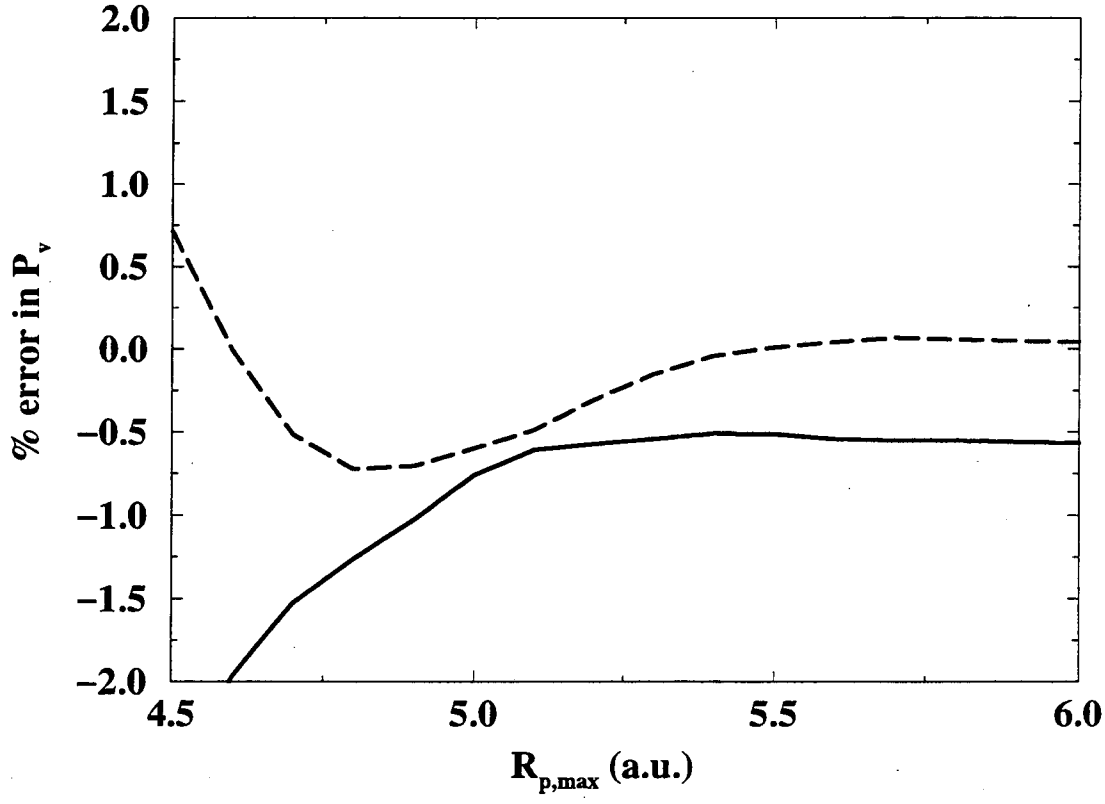

Figure 2.6: Percent error in the initial state-selected reaction probabilities as a function of the extent of the grid in the product arrangement, $R_{p,max}$ at E = 1.0 eV. The solid line is the error for P_0 and the long-dashed line the error for P_1. The error is calculated relative to the results of Bondi and Connor (Ref. 69).

$R_{r,max}$ = 6.9 a.u., N_B = 3.5, and V_{cut} = 4.1 eV. This is merely an illustration of the convergence of the initial state-selected probabilities on the extent of the grid in the product valley. In fact, the minimum grid needed to obtain <1% error has $R_{r,max}$ = 6.8 a.u., $R_{p,max}$ = 5.2 a.u., N_B = 3.2, and V_{cut} = 3.8 eV corresponding to 290 DVR points (only slightly more than half that needed for the state-to-state probabilities). However, the reaction probabilities converge to within 3% for V_{cut} = 3.1 eV and a grid as small as 231 points.

Inelastic Distorted Waves and Numerov Propagation

In calculating partially state-resolved reaction probabilities we have also used inelastically distorted waves[70,71] for Φ_n, which are useful in reducing the size of the grid needed to represent the Green's function because the reactant absorbing potential can be brought in closer to the interaction region. (Non-reactive distorted waves have also been used analogously in S-matrix Kohn variational calculations of reactive scattering.[72–74])

In this work, we have used the (standard) Numerov propagation method.[71] We note that any inelastic propagation algorithm would suffice for the present purpose. Indeed, the standard Numerov algorithm just described is not suitable for describing closed channels, for which the *renormalized* Numerov algorithm can be used. To obtain inelastically distorted waves, we need to solve the Schrödinger equation from the asymptotic reactant valley inward towards the interaction region. The full Schrödinger equation is

$$\left[-\frac{\hbar^2}{2\mu_R}\frac{\partial^2}{\partial R^2} - \frac{\hbar^2}{2\mu_r}\frac{\partial^2}{\partial r^2} + V(R,r) - E\right]\Phi(R,r) = 0. \tag{2.85}$$

We can define the asymptotic vibrational Hamiltonian as

$$\hat{h}^{\tau}_{asym} = -\frac{\hbar^2}{2\mu_r}\frac{d^2}{dr^2} + \nu^{\tau}_{asym}(r) \tag{2.86}$$

where the asymptotic potential is defined by the limit

$$\nu^{\tau}_{asym}(r) = \lim_{R_\tau \to \infty} V(R,r). \tag{2.87}$$

Here $\tau = r, p$ is the arrangement index. For simplicity, we will henceforth assume we are interested only in computing distorted waves in the reactant arrangement. If we define the interaction potential as $V_{int}(R,r) \equiv V(R,r) - \nu_{asym}(r)$ then the Schrödinger equation takes the form

$$\left[-\frac{\hbar^2}{2\mu_R}\frac{\partial^2}{\partial R^2} + V_{int}(R,r) + \hat{h}_{asym} - E\right]\Phi(R,r) = 0. \tag{2.88}$$

We can expand the asymptotic reactant wavefunction for vibrational channel n as

$$\Phi_n(R,r) = \sum_{n'} \phi_{n'}(r)\, u_{n' \leftarrow n}(R), \tag{2.89}$$

where $\phi_{n'}$ is the asymptotic vibrational state in channel n', satisfying

$$\hat{h}_{asym}\,\phi_{n'} = \varepsilon_{n'}\,\phi_{n'}. \tag{2.90}$$

The translational coefficient, $u_{n'\leftarrow n}(R)$, must satisfy the asymptotic boundary condition

$$u_{n'\leftarrow n}(R) \sim \delta_{n'\leftarrow n}\,\frac{e^{-ik_nR}}{v_n^{1/2}}, \tag{2.91}$$

requiring that there only be amplitude in state n at large R.

Inserting this expansion in the Schrödinger equation, multiplying by $\phi_k^*(r)$, and integrating over r results in a set of coupled linear equations

$$\left\{\frac{d^2}{dR^2}\,\mathbf{I} - \frac{2\mu_R}{\hbar^2}\left[\mathbf{V}_{int}(R) - \mathbf{E}_t\right]\right\}\cdot\mathbf{u}(R) = 0, \tag{2.92}$$

where $\mathbf{I}$ is the identity matrix in the vibrational channel space. Similarly,

$$\{\mathbf{V}_{int}(R)\}_{k,n'} = \langle\phi_k \mid \hat{V}_{int} \mid \phi_{n'}\rangle, \tag{2.93}$$

is the matrix of the interaction potential,

$$\{\mathbf{E}_t\}_{k,n'} = (E - \varepsilon_{n'})\,\delta_{k,n'}, \tag{2.94}$$

is the (diagonal) matrix of translational energies, and $\mathbf{u}(R)$ is the matrix of translational coefficients in the vibrational channel space.

We want to solve this for $\mathbf{u}(R)$ on a grid of points in the R coordinate. When the DVR grid is laid out in the reactant Jacobi coordinates it is convenient to choose the Numerov grid such that every fifth or tenth point, say, corresponds to a DVR grid point. (The Numerov grid generally needs to be denser than that for the DVR.) Once the R grid is defined,

$$R_m = mh, \qquad m = 1, \ldots, M \tag{2.95}$$

where h is the grid spacing, we define the matrix

$$\mathbf{T}_m = \frac{2\mu_R}{\hbar^2}\left[\mathbf{V}_{int}(R_m) - \mathbf{E}_t\right]. \tag{2.96}$$

The differential equation in the radial coordinate, Eq. (2.92), can be solved on this grid using a three-point recursion relation

$$\left(\mathbf{I}-\frac{h^2}{12}\mathbf{T}_m\right)\cdot\mathbf{u}_m-2\left(\mathbf{I}+5\frac{h^2}{12}\mathbf{T}_{m-1}\right)\cdot\mathbf{u}_{m-1}+\left(\mathbf{I}-\frac{h^2}{12}\mathbf{T}_{m-2}\right)\cdot\mathbf{u}_{m-2}=0, \quad (2.97)$$

which, upon solving for the matrix $\mathbf{u}_m$ gives

$$\mathbf{u}_m=\left(\mathbf{I}-\frac{h^2}{12}\mathbf{T}_m\right)^{-1}\left[2\left(\mathbf{I}+5\frac{h^2}{12}\mathbf{T}_{m-1}\right)\cdot\mathbf{u}_{m-1}+\left(\mathbf{I}+\frac{h^2}{12}\mathbf{T}_{m-2}\right)\cdot\mathbf{u}_{m-2}\right]. \quad (2.98)$$

This equation is solved from the asymptotic valley inward starting with the initial conditions at the two Numerov grid points, R_m and R_{m-1}:

$$\begin{aligned}(\mathbf{u}_m)_{n,n'} &= \delta_{n,n'}\frac{e^{-ik_nR_m}}{v_n^{1/2}},\\ (\mathbf{u}_{m-1})_{n,n'} &= \delta_{n,n'}\frac{e^{-ik_nR_{m-1}}}{v_n^{1/2}}.\end{aligned} \quad (2.99)$$

(*i.e.*, therefore $S^0_{n',n}=0$).

Figure 2.7 shows the initial state-selected reaction probabilities over a range of total energies for two different grid sizes compared to the results of Bondi and Connor. For the probability of reaction from the ground vibrational state, $P_0(E)$, the agreement is excellent for both values of $R_{r,max}$, except near the resonance at 0.9 eV where the error is on the order of several percent. For $P_1(E)$ reasonable agreement is obtained with the smaller grid while for the larger grid the agreement is within 1% except around 0.9 eV. The difficulty around this energy is due to the low translational energies associated with the excited vibrational state. These low translational energies require a very slow turn on of the absorbing potential to avoid reflection. It should be noted that the parameters describing the grid and absorbing potential were obtained by converging the reaction probabilities at $E=1.0$ eV. It is encouraging that such agreement can be obtained over the entire energy range using one set of parameters. For comparison with the above results, the minimum grid size needed to converge to within 1% at $E=1.0$ eV is 216 DVR points.

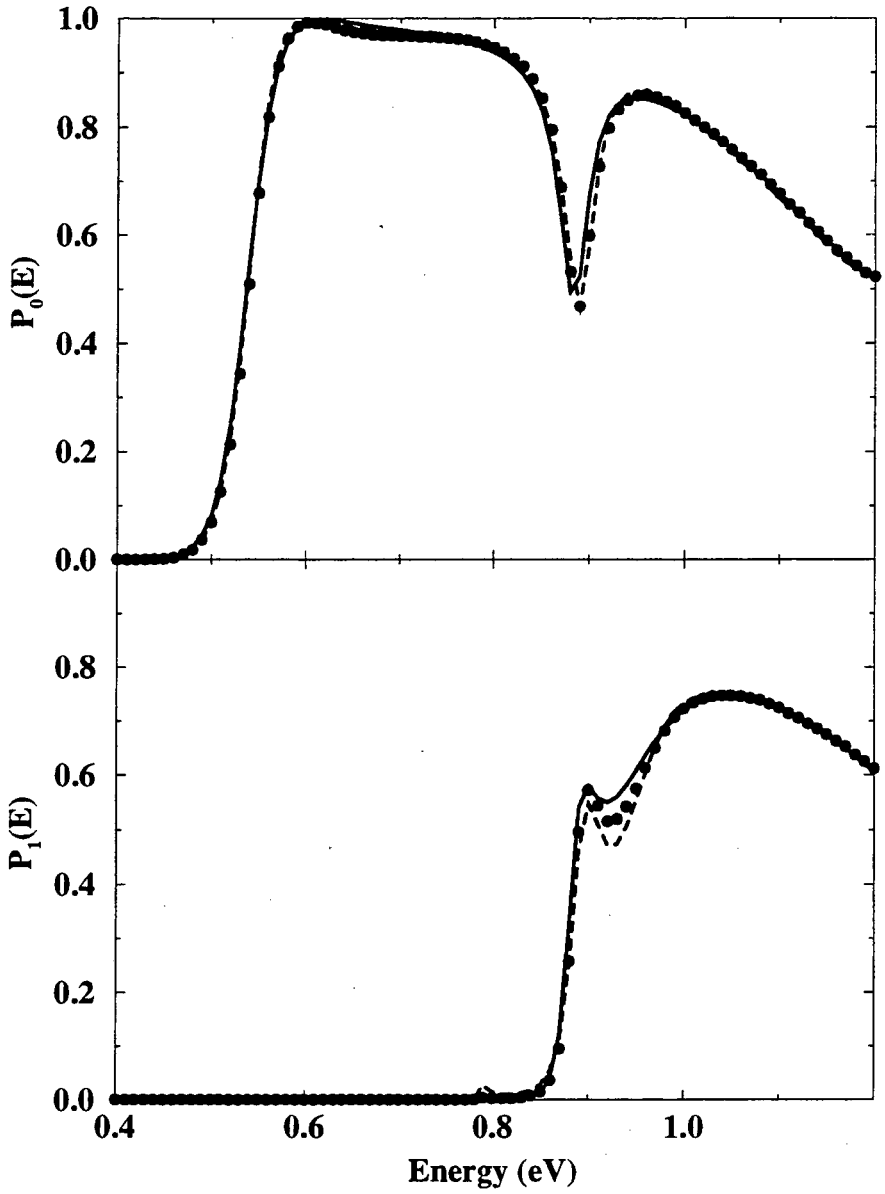

Figure 2.7: Initial state-selected reaction probabilities, $P_0(E)$ and $P_1(E)$, for the collinear H + H_2 reaction calculated with the DVR-ABC Green's function and using inelastic distorted waves. The solid line represents the results of Bondi and Connor (Ref. 69), the present results with $R_{r,max} = 5.5$ a.u., and $R_{r,max} = 6.5$ a.u. are shown as the dashed line and the filled circles, respectively.

2.4 The OH + H_2 Reaction

Quantum mechanical scattering calculations have advanced to the point that rigorous calculations are now possible for a number of atom-diatom reactions (A + BC → AB + C), and the first attempts at rigorous treatments of four atom reactions are beginning to appear.[75–89,61,62] Due to the light masses involved and the availability of a reasonable potential energy surface, the

$$OH + H_2 \rightarrow H_2O + H \tag{2.100}$$

reaction has become the benchmark of choice for exact quantum treatments of a diatom-diatom collision. Already, there have been two full dimensional state-selected time-dependent wavepacket calculations[88,89] on this system as well as a calculation of the cumulative reaction probability using a discrete variable representation (DVR) with absorbing boundary conditions (ABC) to represent the Green's function.[61,62]

Despite the advances of the last decade, exact quantum scattering calculations remain unfeasible for systems with five or more atoms and indeed, for most four atom reactions. At the same time, it may not be necessary to treat all the degrees of freedom in a large system using rigorous quantum mechanics. An excellent example of this is the OH bond in reaction (2.100). *Ab initio* calculations show that the bond distance hardly changes throughout the entire reaction,[90] and the full dimensional dynamics calculations show that freezing this bond has a minimal effect on the reaction probabilities.[88,89] The logical approach to treating a large system "rigorously" may lie in reduced dimensionality, mixed quantum-classical,[91–93] or mixed quantum-semiclassical approaches.[94]

The DVR-ABC formalism for calculating the full reactive scattering Green's function was first introduced by Seideman and Miller[9] and applied to cumulative reaction probabilities. Subsequently it was shown to be an efficient method for calculating *state-specific* reaction probabilities.[95,96] The purpose of this paper is twofold: 1) to test the DVR-ABC method on a large multidimensional reactive scattering system, and 2) to show how the same formalism can be used to efficiently calculate photodetachment intensities.

2.4.1 Review of Previous Work

Reaction (2.100) and its reverse reaction

$$H + H_2O \rightarrow OH + H_2, \tag{2.101}$$

(and their isotopic variants) have been of great interest to the chemical dynamics community over the past two decades. In particular, Reaction (2.101) has been extensively studied as a (and so far *the*) primary example of mode-selective chemistry, one of the "holy grails" of chemical research. This reaction also represents an excellent example of the predictive ability of theoretical chemistry as this mode-selective behavior was first seen in the quasiclassical trajectory calculations of Schatz and coworkers. In this section we present a review of the experimental and theoretical work that has been carried out on these two reactions to this date.

Light and Matsumoto first reported the effect of the vibrational excitation of OH and H_2 as measured in a flow tube.[97] They obtained upper limits for the rate constants (at T = 298 K) of the reactions

$$\begin{aligned} OH(v=0) + H_2(v=1) &\rightarrow H_2O + H, \quad k_{01} \\ OH(v=1) + H_2(v=1) &\rightarrow H_2O + H, \quad k_{11} \end{aligned} \tag{2.102}$$

and were able to extract the ratio of these rates with that for the reaction between OH($v = 0$) and H_2($v = 0$) (denoted k_{00} - we will use the notation $k_{v_{OH}v_{H_2}}$). They found that $k_{01}/k_{00} \leq 1000$ and $k_{11}/k_{00} \leq 1600$ indicating that while exciting the H_2 reactant with one quantum of vibrational energy increases the rate significantly, similar excitation of the OH reactant has little effect on the rate. The same qualitative result was subsequently obtained by Zellner and Steinert in another flow tube experiment.[98] They obtained a ratio of $k_{01}/k_{00} = 1.2\ (\pm 0.4) \times 10^2$ at T = 300 K. This is consistent with the upper limit established by Light and Matsumoto. However, Zellner and Steinert characterize this enhancement in the rate as "moderate" since placing the same amount of energy in translation would increase the rate by a factor $\sim 5 \times 10^3$. Note that the transition state for this reaction is almost collinear, with an $O - H - H$ angle of about 164°, and the barrier is "early" (with a height

of $\sim$ 0.26 eV), consistent with the exoergic character (by $\sim$ 0.64 eV) of the reaction (Hammond's postulate). In such a case, Polanyi's rules[99,100] predict that translational energy would be more effective than H_2 vibration in promoting the reaction. Thus, this experimental result confirms the expectation formed from these simple guidelines. Around the same time, Glass and Chaturvedi[101] measured the ratio k_{01}/k_{00} as 155 ($\pm$ 38), in excellent agreement with Zellner and Steinert. They also found that k_{10}/k_{00} and $k_{20}/k_{00} \leq 1.5$ which is consistent with the results of Light and Masumoto.[97]

The first theoretical calculations on these reactions began about the same time with *ab initio* calculations of the potential energy by Walch and Dunning[90] and the thermal rate constant (from transition state theory) for Reaction (2.100) by Schatz and Walch.[102] The *ab initio* potential energy calculations give a planar transition state which is almost collinear with an O-H-H angle of 15° pointing *cis* with the H-O-H angle at 98°. The reaction is found to be exoergic by $\sim$ 0.7 eV with an early barrier of about 0.27 eV.[90] The transition state theory rate constants obtained by Schatz and Walch are in very good agreement with the experimental results once the Wigner tunneling correction is incorporated. A potential energy surface was obtained by Schatz and Elgersma[103] as an analytical fit to the *ab initio* points (See Figure 2.8). This surface is often referred to as the Walch-Dunning-Schatz-Elgersma, or WDSE, surface. The surface does suffer from some inaccuracies, however. The transition state geometry is given as a *trans* configuration and there is a spurious well just before the barrier on the OH + H_2 side. The problem of the well has been addressed by a modification of the surface introduced by Clary.[75]

Quasiclassical trajectory studies of the system were first carried out by Schatz and co-workers. Schatz and Elgersma first reported calculations on the reaction of ground state OH and H_2 and the resulting product energy partitioning. They found that the majority of the energy ($\sim$ 55%) was channeled into vibration of H_2O (as expected for an early barrier) with translation and rotation receiving 35% and 10% of the available energy, respectively. Following this, Schatz examined the effect of the vibrational excitation (by one quantum) of the reactants.[104] This quasiclassical trajectory study found the rate constant at 300 K was enhanced by a factor of only 1.28 upon excitation of the OH bond. On the other hand, exciting the

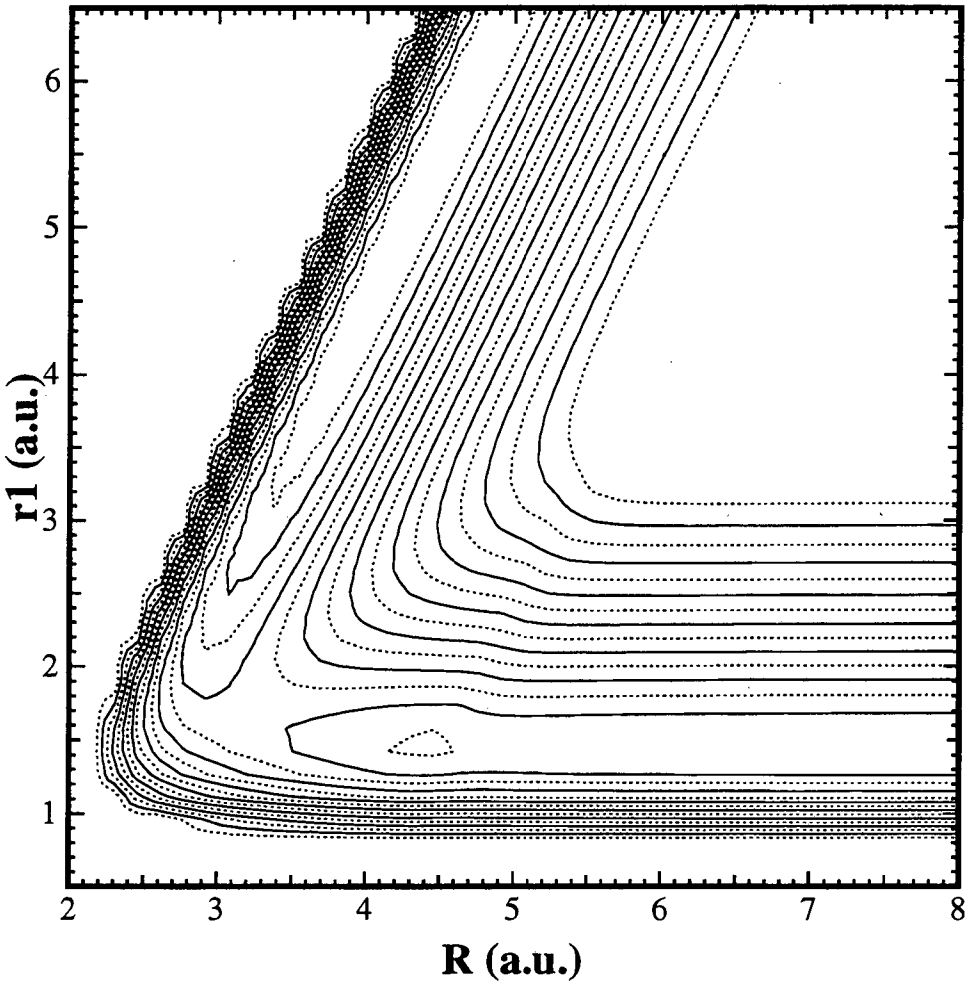

Figure 2.8: Contour plot of the WDSE potential energy surface for the OH + H_2 system. Here R is the distance between the OH and H_2 centers-of-mass and r_1 is the H_2 bond distance. All other coordinates are set to their values at the transition state.

H_2 diatom resulted in a rate 393 times greater. More significantly, the first hint of mode-specific chemistry for this reaction was seen in the product vibrational energy distribution. When H_2 was excited the extra energy went into the vibrations of H_2O and was randomly distributed among the modes. However, when OH was excited, the extra energy went into the vibrations of H_2O but almost completely into the OH stretch modes. Schatz, Colton, and Grant[105] performed a quasiclassical trajectory study on the H + HOD $\rightarrow$ H_2 + OD reaction and found that the rate is 10-1000 times larger when the OH bond is excited with five quanta of energy than when the OD bond is excited with the same amount of energy. This was the first observation, theoretical or experimental, of mode-specificity in this system.

Within the last six years, numerous reduced and full dimensionality quantum mechanical calculations have been carried out on the Reactions (2.100) and (2.101). In particular, Clary and co-workers[75–78] have calculated state-to-state S-matrix elements using the rotating bond approximation (RBA) and obtained good agreement with experimental results.[78] In the RBA, the H_2 bond axis is held fixed relative to the vector joining the centers-of-mass of the two diatoms and the moment of inertia is modified to give the proper asymptotic rotational energy levels of the reactants and products.[75] Within this approximation they were able to calculate reaction probabilities, cross sections, and rate constants. In addition, Clary compared the three degree of freedom calculations (where the H_2 bond, the OH bend, and the diatom translational coordinate are treated explicitly) to four degree of freedom calculations in which the OH vibration is included.[76] The slight differences indicate that the OH bond does indeed act as a spectator to the reaction.

Echave and Clary have carried out a full planar calculation.[79] Their approach differs significantly from the four degree of freedom calculations to be introduced in Section 2.4.3. Namely, they treat the OH and H_2 diatoms as plane rotors with angles in the range $(0, 2\pi)$ and eigenfunctions of the form $e^{im\varphi}$. This approach is similar to that of Kuppermann and co-workers who presented the first exact calculation of planar atom-diatom scattering.[106,107] On the other hand, we employ a planar approximation in which the diatoms are treated as three-dimensional rotors with the projection quantum number constrained to equal zero. The different results obtained

with these two choices will be discussed in Section 2.4.4. Recently, Palma and Echave carried out a planar quasiclassical trajectory study of the OH + H_2.[108]

Wang and Bowman have carried out an investigation of both reactions[80–82] within the adiabatic bend approximation.[109,110] In this reduced dimensionality method, the calculation is carried out on an effective potential formed by minimizing the potential with respect to the bending angles and adding the adiabatic bending energy. The result is a three-dimensional calculation involving only radial degrees of freedom. This allows for investigation of vibrationally state-specific effects but limits the information that can be obtained regarding the rotational degrees of freedom to adiabatic models. Wang and Bowman find good qualitative agreement with the experimental results indicating a significant enhancement of (in this case) the reaction probability upon H_2 excitation but little change for OH excitation.

Baer and co-workers have treated the reaction using a sudden approximation for the angular degrees of freedom and obtained state-to-state reaction probabilities for Reactions 2.100 and 2.101.[83–86] Their cross sections show qualitative agreement with experiment and more accurate theoretical calculations except in calculations in which the four atoms are constrained to be collinear.

While most of the quantum mechanical calculations have been carried out on the OH + H_2 reaction (due to the smaller number of reactant states and the simpler form of the reactant eigenfunctions) most of the recent experiments have examined the H + H_2O reaction (because of its properties of mode- and bond-selective chemistry). These experiments have primarily been performed by two groups. Crim and co-workers have looked at reaction of H atoms with H_2O and HOD molecules which have overtone excitation in the local mode OH stretch.[111–115] They found, for example, that exciting the fourth overtone of the OH stretch in HOD before reacting with H gives OD + H as products more than two orders of magnitude more frequently than OH + D. They also found that if one OH bond in H_2O is excited to the third overtone and the other to the first, the resulting OH product is eight times more likely to be vibrationally excited than not. On the other hand, less than 5% is excited if the initial H_2O has the fourth overtone excited in one bond and none in the other. These experiments validate this reaction as the principle example to this point of

r_1	r_2	R	γ_1	γ_2	φ
1.64 a.u.	1.86 a.u.	3.16 a.u.	169.4°	122.3°	0°

Table 2.1: The values of the reactant Jacobi coordinates at the transition state geometry for the OH + H_2 reaction.

mode- and bond-selective chemistry. Zare and co-workers have shown that the same qualitative results are observed in reactions where the H_2O has only one overtone of excitation in the OH bond rather than four (with the difference in energy made up in translation.[116–119]

Recently, the first molecular beam experiment for the D_2 + OH → HOD + D reaction was performed by Alagia *et al.*[120] They measured the angular distribution and found predominantly backscattered products which is consistent with a nearly collinear transition state. Clary's three degree of freedom RBA calculations are in excellent agreement with the experimental distribution.[78]

There have been many more theoretical and experimental studies on the H_2O + H ↔ OH + H_2 system and its isotopic variants that we have not reported here.

Finally, we should note that in addition to the immense theoretical interest in Reaction (2.100) as the prototypical four-atom reactive system and its reverse reaction as the primary example of mode-specific chemistry, it also is of interest as part of the mechanism for H_2 combustion.[121]

2.4.2 Two Degree of Freedom Calculations

We have carried out calculations for the OH + H_2 reaction similar to that for collinear H + H_2. These are two degree of freedom calculations in which the translational scattering coordinate, R, and the H_2 bond distance, r_1 are treated dynamically. These coordinates are taken as Cartesian and the Hamiltonian is given by

$$\hat{H} = -\frac{\hbar^2}{2\mu_R}\frac{\partial^2}{\partial R^2} - \frac{\hbar^2}{2\mu_1}\frac{\partial^2}{\partial r_1^2} + V_{2d}(r_1, R), \tag{2.103}$$

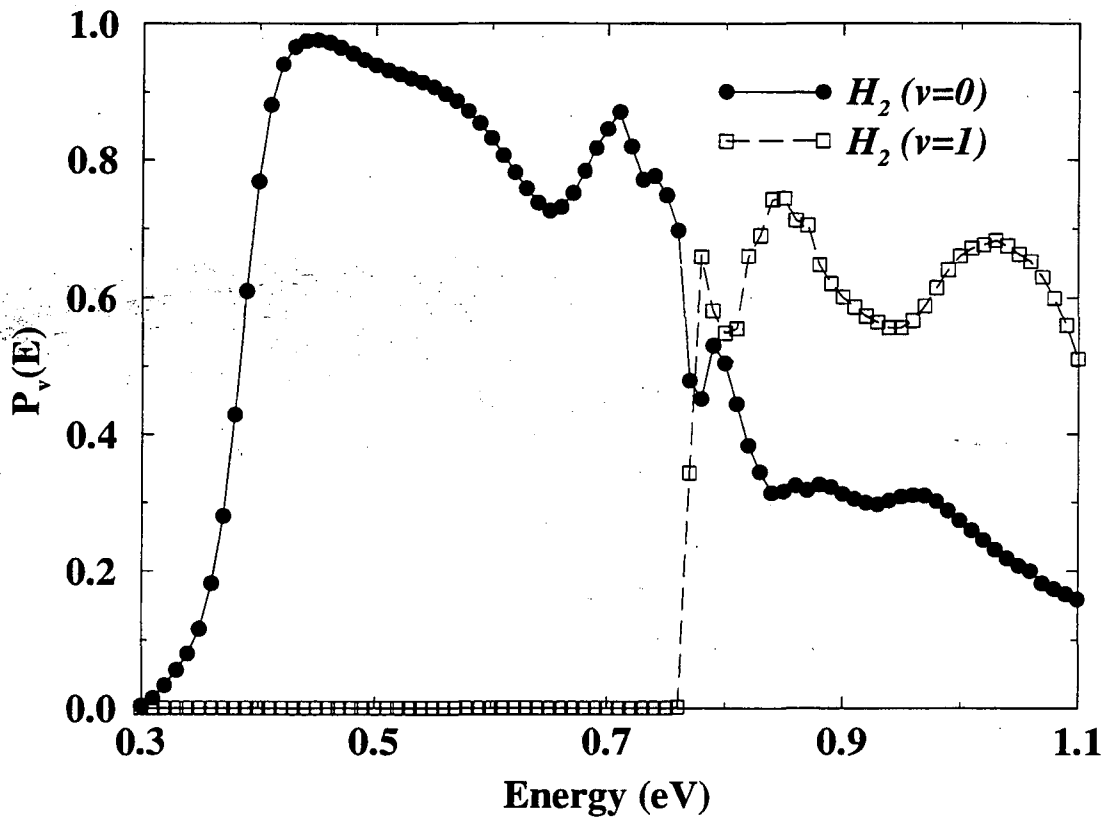

Figure 2.9: The initial state-selected reaction probabilities for the two degree of freedom $OH + H_2(v = 0, 1)$ reaction as a function of total energy relative to bottom of the $OH + H_2$ asymptotic valley.

where the reduced masses are

$$\begin{aligned} \mu_R &= \frac{(m_O + m_H)(m_H + m_H)}{m_O + m_H + m_H + m_H}, \\ \mu_1 &= \frac{m_H m_H}{m_H + m_H}, \end{aligned} \tag{2.104}$$

and the two-dimensional potential is obtained by evaluating the full potential at fixed values of the angles and OH bond distance:

$$V_{2d}(r_1, R) = V(r_1, r_2^0, R, \gamma_1^0, \gamma_2^0, \varphi^0). \tag{2.105}$$

In the present calculations, the angles and OH bond distance were set to their values at the transition state geometry as given in Table 2.1. We note that the value of

γ_2 does not give the proper water geometry. Thus, in this two degree of freedom potential surface does not contain the correct product valley; the potential becomes repulsive for large values of r_1. This gives a limited range of r_1 for which convergence can be achieved, though this does not present a significant problem.

As in the collinear H + H_2 case, we use the $(-\infty, \infty)$ sinc-function DVR of Colbert and Miller for the two coordinates. The reactant absorbing potential is a function of the translational coordinate, $\epsilon_r = \epsilon_r(R)$, while the product absorbing potential is a function of the H_2 bond distance, $\epsilon_p = \epsilon_p(r_1)$.

Figure 2.9 shows the two degree of freedom initial state-selected reaction probabilities for OH + $H_2(v = 0, 1)$ as a function of total energy. There are a number of things to note about these results. The $v = 0$ probability looks much like that for the collinear H + H_2 reaction. The probability first becomes significant due to tunneling below the threshold energy (which is the sum of the barrier height and the adiabatic H_2 vibrational energy). At energies near the threshold the probability rises rapidly to a maximum value very near one (this high value is almost certainly due to the constraint to two dimensions). After the maximum, $P_0(E)$ falls slowly before experiencing a sharp resonance around E = 0.77 eV corresponding to the opening of the $H_2(v = 1)$ channel. The OH + $H_2(v = 0)$ state does exhibit more structure in the probabilities than collinear H + H_2.

2.4.3 Four Degree of Freedom Calculations

The Hamiltonian and The Basis Set

Since we are interested in initial state-selected quantities, we have chosen to use the Jacobi coordinates of the reactants. This coordinate system is advantageous for describing the asymptotic states of the reactants. We denote the H_2 and OH bond distances by r_1 and r_2, respectively. The distance between the H_2 and OH centers-of-mass is R. γ_1 is the angle between $\mathbf{r}_1$ and $\mathbf{R}$, γ_2 the angle between $\mathbf{r}_2$ and $\mathbf{R}$, and φ is the torsional angle.

We have calculated reaction probabilities and photodetachment intensities explicitly treating four degrees of freedom. The OH bond distance is frozen at its

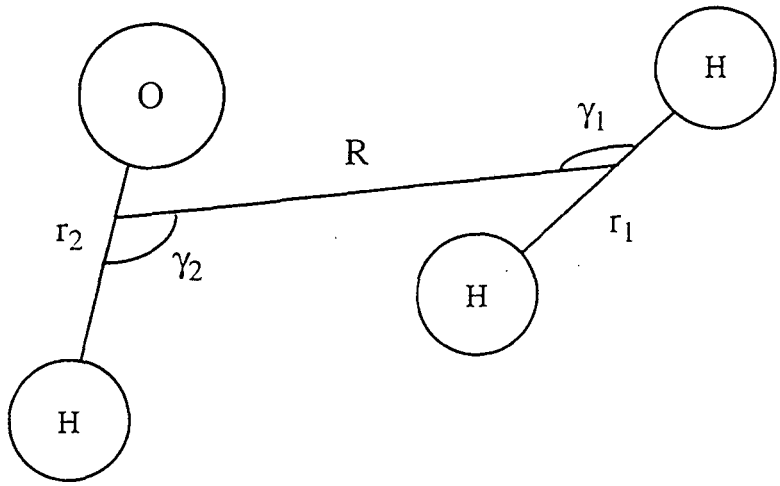

Figure 2.10: The Jacobi coordinates for the $OH + H_2$ arrangement. The out-of-plane torsional angle, φ, is not shown.

equilibrium value and the torsional angle is fixed at $\varphi = 0$, *i.e.*, the planar configuration. These give the proper transition state geometry for the reaction. The quality of these approximations can be seen in comparing our results to the higher dimensional reactive scattering calcuations. One can obtain the reduced dimensionality Hamiltonian in a straightforward way from the full Hamiltonian. The four degree of freedom Hamiltonian for $J = 0$ is given by

$$\begin{aligned}
\hat{H} &= -\frac{\hbar^2}{2\mu_1}\frac{1}{r_1}\frac{\partial^2}{\partial r_1^2}r_1 - \frac{\hbar^2}{2\mu_R}\frac{1}{R}\frac{\partial^2}{\partial R^2}R \\
&+ \left(\frac{1}{2\mu_1 r_1^2} + \frac{1}{2\mu_R R^2}\right)\hat{\mathbf{j}}_1^2 \\
&+ \left(\frac{1}{2\mu_2 r_{2,eq}^2} + \frac{1}{2\mu_R R^2}\right)\hat{\mathbf{j}}_2^2 \\
&+ \hat{V}(r_1, r_2 = r_{2,eq}, R, \gamma_1, \gamma_2, \varphi = 0),
\end{aligned} \tag{2.106}$$

where $\hat{\mathbf{j}}_1$ and $\hat{\mathbf{j}}_2$ are the angular momentum operators for the H_2 and OH rotation, respectively. We will use j_1 and j_{H_2} interchangeably for the H_2 rotation quantum

number and similarly j_2 and j_{OH}. The angular momentum operator $\hat{\mathbf{j}}_1^2$ is given by

$$\hat{\mathbf{j}}_1^2 = \frac{\partial^2}{\partial\gamma_1^2} + \cot\gamma_1 \frac{\partial}{\partial\gamma_1} = \frac{1}{\sin^{1/2}\gamma_1}\left[\frac{\partial^2}{\partial\gamma_1^2} + \frac{1+\sin^2\gamma_1}{4\sin^2\gamma_1}\right]\sin^{1/2}\gamma_1, \tag{2.107}$$

and similarly for $\hat{\mathbf{j}}_2^2$.

We have four independent variables in this case: r_1, R, γ_1 and γ_2. We want to define a direct product basis in these coordinates,

$$\tilde{\phi}_{jnml} = \tilde{u}_j(R)\,\tilde{v}_n(r_1)\,\tilde{f}_m(\gamma_1)\,\tilde{g}_l(\gamma_2). \tag{2.108}$$

Using this basis (assuming it is real), a given matrix element of the Hamiltonian has the form

$$\begin{aligned}
\langle j'n'm'l'|\hat{H}|jnml\rangle &= \int_0^\pi \sin\gamma_2\,d\gamma_2 \int_0^\pi \sin\gamma_1\,d\gamma_1 \int_0^\infty r_1^2\,dr_1 \int_0^\infty R^2\,dR \\
&\times \tilde{u}_{j'}(R)\,\tilde{v}_{n'}(r_1)\,\tilde{f}_{m'}(\gamma_1)\,\tilde{g}_{l'}(\gamma_2) \\
&\times \left\{-\frac{\hbar^2}{2\mu_1}\frac{1}{r_1}\frac{\partial^2}{\partial r_1^2}r_1 - \frac{\hbar^2}{2\mu_R}\frac{1}{R}\frac{\partial^2}{\partial R^2}R\right. \\
&+ \left(\frac{1}{2\mu_1 r_1^2} + \frac{1}{2\mu_R R^2}\right)\frac{1}{\sin^{1/2}\gamma_1}\left[\frac{\partial^2}{\partial\gamma_1^2} + \frac{1+\sin^2\gamma_1}{4\sin^2\gamma_1}\right]\sin^{1/2}\gamma_1 \\
&+ \left(\frac{1}{2\mu_2 r_{2,eq}^2} + \frac{1}{2\mu_R R^2}\right)\frac{1}{\sin^{1/2}\gamma_2}\left[\frac{\partial^2}{\partial\gamma_2^2} + \frac{1+\sin^2\gamma_2}{4\sin^2\gamma_2}\right]\sin^{1/2}\gamma_2 \\
&+ \left.\hat{V}(r_1,R,\gamma_1,\gamma_2)\right\}\,\tilde{u}_j(R)\,\tilde{v}_n(r_1)\,\tilde{f}_m(\gamma_1)\,\tilde{g}_l(\gamma_2).
\end{aligned} \tag{2.109}$$

We can rearrange Jacobian factors in the integral to obtain

$$\begin{aligned}
\langle j'n'm'l'|\hat{H}|jnml\rangle &= \int_0^\pi \sin\gamma_2\,d\gamma_2 \int_0^\pi \sin\gamma_1\,d\gamma_1 \int_0^\infty r_1^2\,dr_1 \int_0^\infty R^2\,dR \\
&\times R\tilde{u}_{j'}(R)\,r_1\tilde{v}_{n'}(r_1)\,\sin^{1/2}\gamma_1\tilde{f}_{m'}(\gamma_1)\,\sin^{1/2}\gamma_2\tilde{g}_{l'}(\gamma_2) \\
&\times \left\{-\frac{\hbar^2}{2\mu_1}\frac{\partial^2}{\partial r_1^2} - \frac{\hbar^2}{2\mu_R}\frac{\partial^2}{\partial R^2}\right. \\
&+ \left(\frac{1}{2\mu_1 r_1^2} + \frac{1}{2\mu_R R^2}\right)\left[\frac{\partial^2}{\partial\gamma_1^2} + \frac{1+\sin^2\gamma_1}{4\sin^2\gamma_1}\right] \\
&+ \left(\frac{1}{2\mu_2 r_{2,eq}^2} + \frac{1}{2\mu_R R^2}\right)\left[\frac{\partial^2}{\partial\gamma_2^2} + \frac{1+\sin^2\gamma_2}{4\sin^2\gamma_2}\right] \\
&+ \left.\hat{V}(r_1,R,\gamma_1,\gamma_2)\right\} \\
&\quad R\tilde{u}_j(R)\,r_1\tilde{v}_n(r_1)\,\sin^{1/2}\gamma_1\tilde{f}_m(\gamma_1)\,\sin^{1/2}\gamma_2\tilde{g}_l(\gamma_2).
\end{aligned} \tag{2.110}$$

This suggests that we can include the Jacobian factors into the basis functions, with the corresponding modification to the Hamiltonian operator (to that in the curly brackets). Thus, we define new basis functions as

$$\begin{aligned} u_j(R) &= R\tilde{u}_j(R) \\ v_n(r_1) &= r_1\tilde{v}_n(r_1) \\ f_m(\gamma_1) &= \sin^{1/2}\gamma_1\tilde{f}_m(\gamma_1) \\ g_l(\gamma_2) &= \sin^{1/2}\gamma_2\tilde{g}_l(\gamma_2), \end{aligned} \tag{2.111}$$

which have orthonormality relations given by

$$\int_0^\infty u_{j'}(R)\,u_j(R)dR = \int_0^\infty \tilde{u}_{j'}(R)\,\tilde{u}_j(R)R^2dR = \delta_{j',j}, \tag{2.112}$$

$$\int_0^\pi f_{m'}(\gamma_1)\,f_m(\gamma_1)\gamma_1 = \int_0^\pi \tilde{f}_{m'}(\gamma_1)\,\tilde{f}_m(\gamma_1)\sin\gamma_1 d\gamma_1 = \delta_{m',m}, \tag{2.113}$$

for example. We have used the sinc-function DVR of Colbert and Miller[37] for the r_1 and R coordinates since they represent the large-amplitude motions making up the reaction coordinate. A Gauss-Legendre DVR was used for the angles γ_1 and γ_2. However, the exchange symmetry of H_2 was exploited so that, for a given parity, only half the angular DVR points were needed for γ_1. It is the modified basis functions in Eq. (2.111), corresponding to the Hamiltonian in Eq. (2.110) that we are defining here as sinc-functions and Legendre polynomials which make up the finite basis representation (FBR) underlying the DVR. (The FBR, in which the integrals in the matrix elements are evaluated by quadrature, and DVR, with grid points defined by that quadrature, are related by a unitary transformation.[39])

In practice, a direct product (raw) grid is first laid down in these coordinates. The "refined" grid is then obtained by truncating the raw grid according to two criterion: (1) an energy cuttoff, *i.e.*, if the potential at a given DVR point is greater than some value V_{cut}, then that point is discarded, and (2) the boundaries of the absorbing potential in the reactant and product valleys. Then the matrix elements of the Hamiltonian are computed in the DVR. Finally, the linear system

$$(E\mathbf{I} - \mathbf{H} + i\boldsymbol{\epsilon}) \cdot \boldsymbol{\Psi}_{\mathbf{n}_r} = i\boldsymbol{\epsilon}_r \cdot \boldsymbol{\Phi}_{\mathbf{n}_r} \tag{2.114}$$

is solved to obtain the reactive scattering wavefunction. The Hamiltonian matrix is sparse in a multidimensional case, which allows the linear algebra to be solved using iterative methods (See Section 2.4.3) which makes large dimensional problems tractable when one cannot store the entire Hamiltonian matrix.

As pointed out above, the potential energy matrix elements are diagonal. The diagonal elements are simply the potential evaluated at the DVR grid point. The DVR matrix elements of the absorbing potential are also diagonal and similarly evaluated. The radial kinetic energy matrix elements can be expressed in closed form[37] as

$$(\hat{T})_{i,i'} = \frac{\hbar^2}{2\mu\Delta r^2}(-1)^{(i-i')} \left\{ \begin{array}{ll} \pi^2/3 - 1/2i^2, & i = i' \\ \frac{2}{(i-i')^2} - \frac{2}{(i+i')^2}, & i \neq i' \end{array} \right\}, \tag{2.115}$$

where Δr is the grid spacing. The $1D$ kinetic energy matrix elements for the angular DVR are given by a sum over Legendre polynomials:

$$(\hat{T}_{ang2})_{i,i'} = \sum_{j=0}^{N-1} \sqrt{w_i}\, P_j(\cos\gamma_{2i})\, j(j+1)\hbar^2 \sqrt{w_{i'}}\, P_j(\cos\gamma_{2i'}) \tag{2.116}$$

for the OH rotation, where N is the number of angular DVR points. For the H_2 rotation, the symmetrized matrix elements are given by

$$(\hat{T}_{ang1})^p_{i,i'} = \sum_{j=0}^{N-1} \sqrt{w_i}\, P_j(\cos\gamma_{1i})\, j(j+1)\hbar^2 \left[1 + (-1)^{(p+j)}\right] \sqrt{w_{i'}}\, P_j(\cos\gamma_{1i'}) \tag{2.117}$$

where p is the parity quantum number. Note that for the symmetrized case we use only half of the angular DVR points for γ_1. (Recall that the kinetic energy operators are those given in Eq. (2.110).

Typically we need 14 DVR points for the γ_2 and 7 points for the symmetrized γ_1 coordinate. We note that using as few as 10 and 5 angular points reduces the accuracy only slightly and produces a significant savings in the size of the basis. The number of radial DVR points are determined by specifying a grid constant, N_B, which is the number of grid points per de Broglie wavelength. A grid constant of 2.6 gives converged results. Depending on the scattering energy, the DVR basis consists of between 20000 to as many as 50000 points for the highest energies.

In our calculations we have used the potential energy surface fit by Schatz and Elgersma[103] to the *ab initio* results of Walch and Dunning[90] (the WDSE surface).

This surface also includes a modification by Clary[75] to remove a spurious well on the OH + H_2 side of the barrier.

The absorbing potential is taken to be a function of the translational Jacobi coordinate in the reactant arrangement, $\epsilon_r = \epsilon_r(R)$, and the H_2 bond distance in the product arrangement $\epsilon_p = \epsilon_p(r_1)$. There are several satisfactory choices for the functional form of the absorbing potential. However any choice must turn on slowly enough not to cause reflection, yet be strong enough to absorb all outgoing flux. We have found the quartic potential to work well,

$$\epsilon_\gamma(R_\gamma) = \lambda \left(\frac{R_\gamma - R_{0,\gamma}}{R_{max,\gamma} - R_{0,\gamma}} \right)^4 \tag{2.118}$$

where $\gamma = p, r$ is the arrangement index and $R_p = r_1$, $R_r = R$. $R_{0,\gamma}$ and $R_{max,\gamma}$ are the starting and ending points of the absorbing potential in the γ arrangement. λ is a strength parameter representing the maximum value of the absorbing potential, generally it is taken to be about 2 eV. The beginning of the absorbing strip is chosen such that the imaginary potential has significant value only where the interaction potential is small.

The Asymptotic State

The asymptotic state of the reactants can be defined by

$$\hat{H}_{asym} \Phi_{\mathbf{n}_r} = \varepsilon_{\mathbf{n}_r} \Phi_{\mathbf{n}_r}, \tag{2.119}$$

where $\hat{H}_{asym}$ is the asymptotic Hamiltonian for reactants given by

$$\hat{H}_{asym} = \lim_{R \to \infty} \hat{H}. \tag{2.120}$$

When the OH and H_2 diatoms are far apart, the eigenvalue problem defined by Eq. (2.119) is separable and becomes four, one-dimensional eigenvalue/eigenfunction problems. However, only for the H_2 vibrational eigenfunctions do we need to carry out a numerical calculation; for the translational coordinate R, spherical Hankel functions of the second kind are the solutions of the radial equation (including the centrifugal potential) with the proper asymptotic boundary conditions, and the OH and H_2

rotations are free rotors with Legendre polynomial eigenfunctions. Expressing the asymptotic state in a space-fixed axis, one has

$$\begin{aligned}\langle r_1, R, \gamma_1, \gamma_2 \mid \Phi_{\mathbf{n}_r} \rangle &= \varphi_v(r_1) \frac{1}{\sqrt{v_\mathbf{n}}} h_\ell^{(2)}(k_\mathbf{n} R) \sqrt{\frac{(2\ell+1)}{4\pi}} \langle j_1\, 0\, j_2\, 0 \mid j_1\, j_2\, J_{12}\, 0 \rangle \\ &\times \langle J_{12}\, 0\, \ell\, 0 \mid J_{12}\, \ell\, 0\, 0 \rangle \frac{1}{\sqrt{2}} [1 + (-1)^{(p+j_1)}]\, P_{j_1}(\cos\gamma_1)\, P_{j_2}(\cos\gamma_2)\end{aligned} \tag{2.21}$$

where we have noted $J = M = K = 0$. φ_v is the asymptotic H_2 vibrational eigenstate, and we have normalized the translational function with respect to the incoming flux; $k_\mathbf{n}$ and $v_\mathbf{n}$ are the translational wavevector and velocity, respectively. The Clebsch-Gordan coefficients are derived from the body-fixed to space-fixed transformation. J_{12} is the vector addition of the diatom angular momenta, j_1 and j_2, and $J = 0$ is obtained from the vector addition of J_{12} and ℓ. p defines the parity of the H_2 rotation, and l is the orbital angular momentum quantum number.

Iterative Methods

For a multidimensional problem, the Hamiltonian is often too large to store in core memory. There are several suitable iterative methods one can use which require only the ability to multiply the Hamiltonian onto a vector. For the reactive scattering calculations here we have used the Newton algorithm developed by Auerbach and Leforestier.[96,122] This method has the advantages that it requires very little core memory (our largest calculations use only $\approx$ 10 MB), displays rapid convergence, and gives the ability to "dial in" the allowed error.

2.4.4 Results and Discussion

We have calculated initial state-selected reaction probabilities over a range of energies for the OH(j_{OH}) + H_2(v, j_{H_2}) reaction for many sets of initial quantum numbers. In order to compare with full dimensional calculations, the reaction probabilities as a function of translational energy are shifted, as has been done previously by Clary.[75] The shift of 0.031 eV[75] is equal to the difference in zero point energy between the transition state and the asymptotic reactants of the neglected degrees of freedom, namely, the *OH* stretch and the torsional angle.

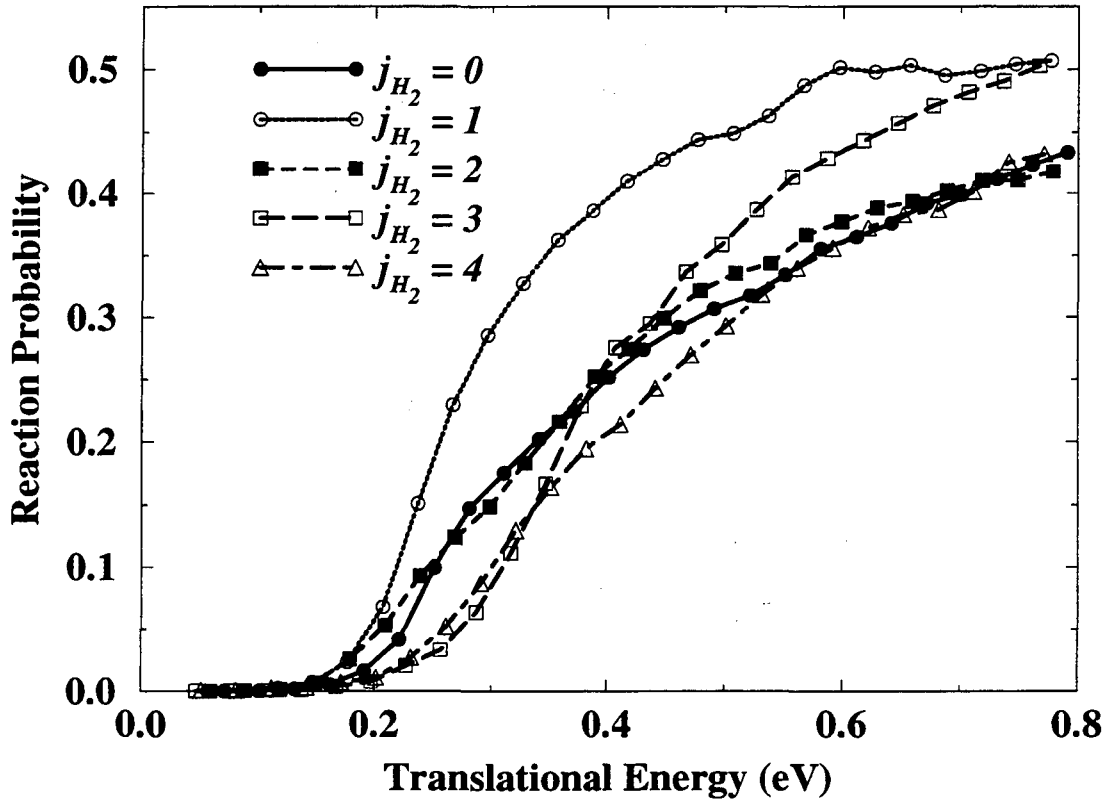

Figure 2.11: Initial state-selected reaction probabilities for the four degree of freedom $OH(j_{OH} = 0) + H_2(v = 0, j_{H_2})$ reaction, for different initial H_2 rotational states.

Figure 2.11 shows the reaction probabilities as a function of initial j_{H_2} for $v = 0$ and $j_{OH} = 0$. As for the $H + H_2$ reaction, the probability is largest for $j_{H_2} = 1$. Although there is not complete quantitative agreement, the reaction probabilities shown have the same qualitative dependence on initial rotational quantum number and translational energy as the five degree of freedom results of Zhang and Zhang in which only the OH bond is held frozen.[87] (We note that full dimensional calculations have shown that including the OH stretch changes the results minimally[88,89] and therefore comparing to the five degree of freedom results highlights the effect of the torsional angle.) Zhang and Zhang observe the $j_{H_2} = 1$ initial state give the largest reaction probability. At lower energies (less than about 0.4 eV) the next largest

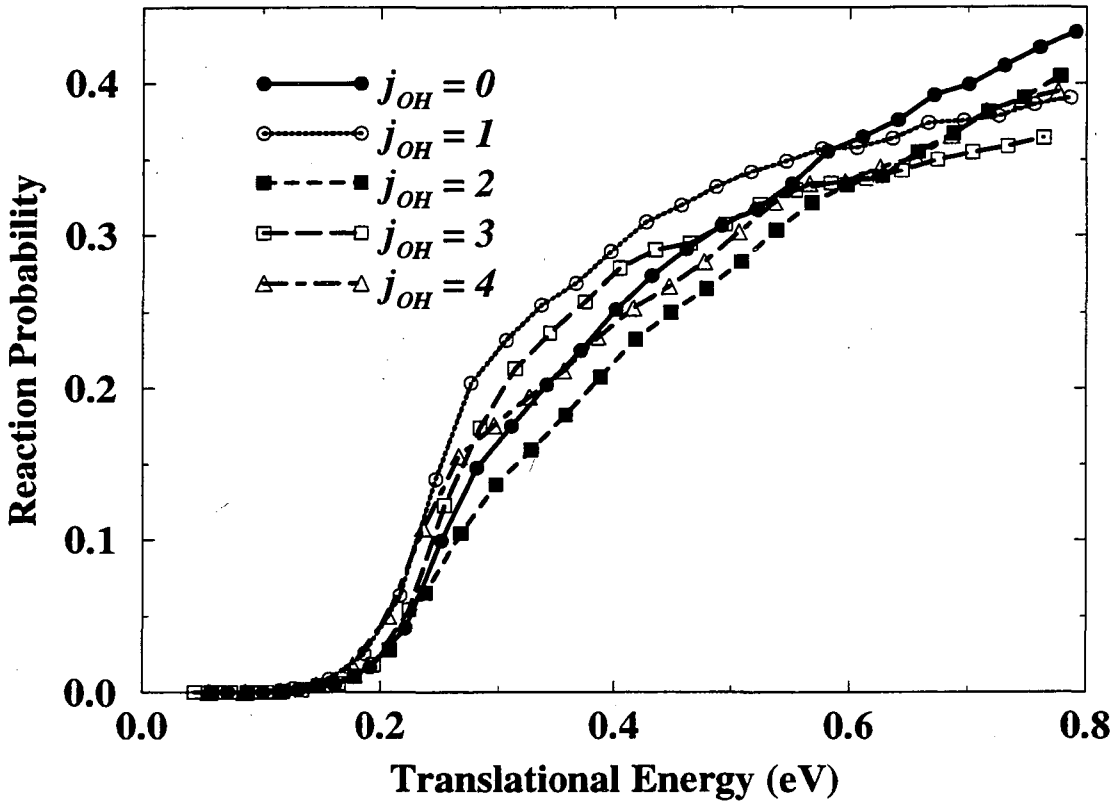

Figure 2.12: Initial state-selected reaction probabilities for the four degree of freedom $OH(j_{OH}) + H_2(v = 0, j_{H_2} = 0)$ reaction, for different initial OH rotational states.

probabilities are the $j_{H_2} = 2$ and 0 initial states. At higher energies, however, these probabilities do not rise as sharply and are overtaken by $j_{H_2} = 3$ and 4. This is a similar scenario to what we observe in Fig. 2.11 with the primary difference being that the present $j_{H_2} = 3$ reaction probability is significantly larger at higher energies than that seen by Zhang and Zhang. The absolute magnitude of the probabilities presented here is somewhat larger than that found in the five degree of freedom calculations,[87] roughly 10 % higher. In addition, the threshold to reaction is approximately the same in both reactions.

Our results are qualitatively different from the planar results of Echave and Clary[79] who observe a monotonic decrease in the reaction probability with initial j_{H_2}.

As discussed in Section 2.4.1, the difference between these two planar calculations can be found in the treatment of the diatom rotations. Echave and Clary represented the diatoms as plane rotors, whereas we have treated the diatoms as three dimensional rotors with the projection quantum number constrained to equal zero. The nature of such a planar calculation has previously been examined by Kuppermann and co-workers[106,107,1,2] for the H + H_2 reaction. They performed both planar and three-dimensional calculations and found two major differences. First, the threshold energy for the planar calculations was lower by about 0.06 eV, equal to the zero point energy in the bend at the transition state. They attribute this to double degeneracy of the linear H_3 bend at the transition state in the three-dimensional problem which does not exist in the planar system. Second, the maximum magnitude of the probabilities is larger for the planar case which they reason is due to the constraint to two-dimensions. They do not report effects on the rotational state dependence of the reaction probabilities. For the OH + H_2 reaction, Echave and Clary do observe a very slightly lower threshold but the maximum magnitude of the probabilities appears to be about the same as the present results, (though they only report probabilities up to translational energies of about 0.37 eV) which is slightly larger than the calculations of Zhang and Zhang.[87]

In Figure 2.12 we show the reaction probabilities for several different values of j_{OH} with $v = 0$ and $j_{H_2} = 0$. There is a very weak dependence on the initial OH rotational quantum number. This is not surprising since this rotation is not a major component of the reaction coordinate and thus should not affect the hydrogen atom transfer as strongly as the H_2 rotation. At low translational energies, the $j_{OH} = 1$ and 3 initial states give the largest reaction probabilities while $j_{OH} = 0$, 2, and 4 become larger at the higher energies (above about 0.6 eV). This is similar to the results of Zhang and Zhang[87] which show that $j_{OH} = 1$ and 3 give the largest probabilities up to 0.7 eV where the $j_{OH} = 0$ and 2 states give equal probabilities. (They do not report results for $j_{OH} = 4$ or for translational energies greater than 0.7 eV.) Again, the present planar calculations give probabilities which are larger by approximately 10-15% and the threshold to reaction is similar. The planar calculations of Echave and Clary find no easily discernable difference between intial states $j_{OH} = 0, 1, \ldots, 5$

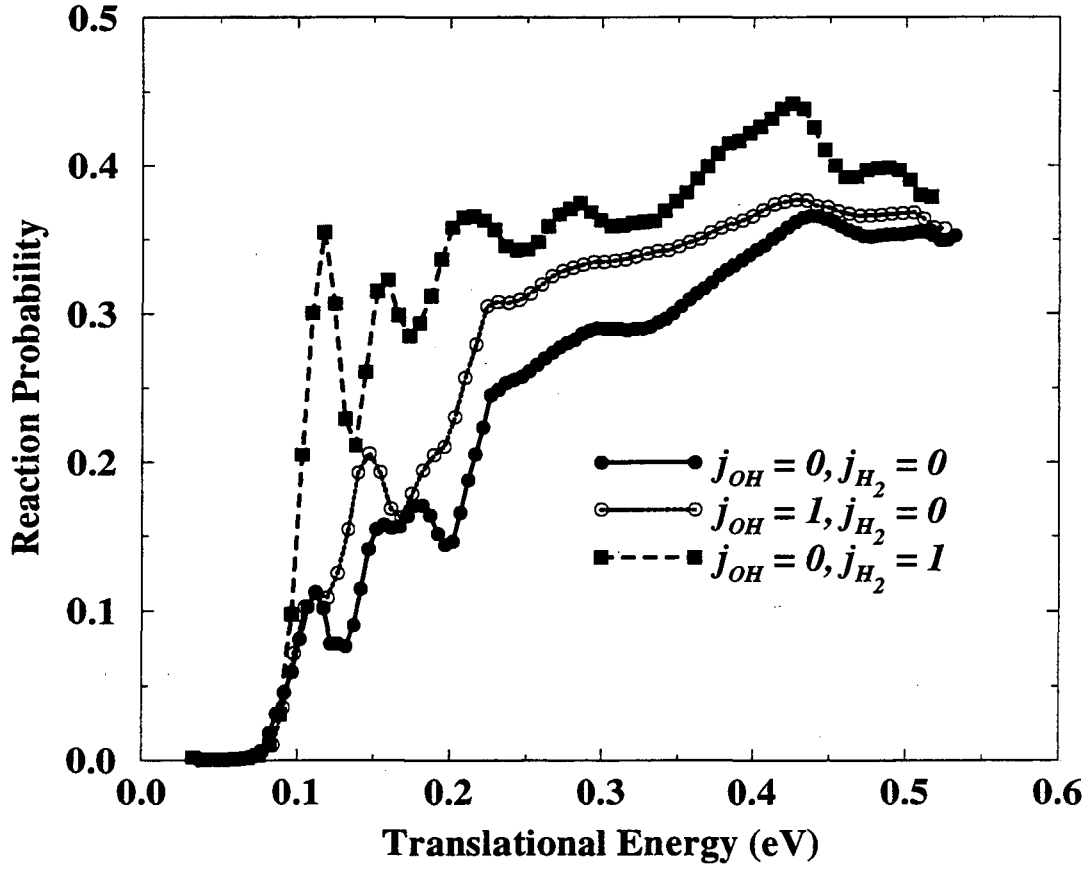

Figure 2.13: Initial state-selected reaction probabilities for the four degree of freedom $OH(j_{OH}) + H_2(v = 1, j_{H_2})$ reaction, for different initial H_2 rotational states.

over translational energies up to 0.37 eV.[79] Their reaction probabilities are somewhat larger than those in Fig. 2.12.

The small barrier for this reaction coupled with the relatively large vibrational spacing for H_2 means that $OH + H_2(v = 1)$ proceeds virtually without a barrier. This can be seen in the sharp threshold seen in the present probabilities shown in Figure 2.13. Thus the reaction probability is greatly enhanced by vibrational excitation of H_2, as noted above in Section 2.4.1. The full-dimensional calculations of Zhang and Zhang[88] and Neuhauser[89] find several strong resonance features in the reaction probabilities for initially vibrationally excited H_2 at translational energies below 0.2

eV. These features are also observed in our calculations as shown in Fig. 2.13. The lowest energy resonance is missing in our results (since we have shifted our probabilities) however the remaining features are well reproduced. We find that rotational excitation also enhances the reaction probability with the H_2 rotation being more effective at promoting reaction.

2.5 Concluding Remarks

In this Chapter we have shown how a localized, square-integrable representation of the Green's function can be achieved by the use of absorbing boundary conditions. This can be used, in conjunction with a discrete variable representation basis, to efficiently calculate both state-to-state and half state-selected reaction probabilities. In computing the S-matrix elements via Eq. (2.56), or the initial state-selected probabilities by Eq. (2.66), one has to solve the set of linear equations

$$(E\mathbf{I} - \mathbf{H} + i\boldsymbol{\epsilon}) \cdot \mathbf{x} = \boldsymbol{\epsilon}_r \cdot \boldsymbol{\Phi}_{n_r}, \tag{2.122}$$

to obtain

$$\mathbf{x} \equiv \mathbf{G} \cdot \boldsymbol{\epsilon}_r \cdot \boldsymbol{\Phi}_{n_r}. \tag{2.123}$$

A column of the S-matrix can then be obtained, giving the probability amplitude for reaction from reactant state n_r to all possible product states. Alternatively, the initial state-selected probability for state n_r can be obtained. This is less expensive (computationally) because the size of the DVR basis can be reduced by bringing in the absorbing potential in the product valley. This is possible because the product state selection is still being "determined" further out in the asymptotic valley than is the simpler question of reactivity.

Application to the collinear H + H_2 reaction demonstated the efficiency of these methods. In addition, it was shown how inelastic distorted waves can be used to reduce the size of the DVR basis in the initial state-selected calculation. The asymptotic wavefunction is then a solution of the Schrödinger equation closer in to the interaction region, and the size of the basis in which the linear system, Eq. (2.122), must be solved is reduced.

Initial state-selected reaction probabilities for the benchmark four atom OH + H_2 reaction have been calculated in reduced dimensionality. The OH bond was held fixed and the reaction constrained to a plane while the remaining four degrees of freedom were treated explicitly. The resulting reaction probabilities have all the qualitative features observed in full-dimensional calculation. This example displays the applicability of the present method to realistic systems.

2.6 Appendix I: Absorbing Potentials

As an *ad hoc* construction introduced (in this case) to make the Green's function localized in space, the absorbing potentials prompt many questions concerning their proper implementation: What properties are desired in an absorbing potential? How is the convergence of a calculation with respect to the absorbing potential obtained? How is accuracy balanced with efficiency? What functional forms are appropriate and what is the 'optimal' choice?

The purpose of this appendix is to address these frequently asked questions regarding absorbing potentials.

How Does an Absorbing Potential Work?

Consider a generic Hamiltonian, in one-dimension, with a negative imaginary potential added:

$$\hat{H}_\epsilon = \hat{H} - i\epsilon(x) = -\frac{\hbar^2}{2m}\frac{\partial^2}{\partial x^2} + V(x) - i\epsilon(x), \tag{2.124}$$

where the function ϵ is everywhere positive. Now the propagation of a wavefunction ψ under this Hamiltonian is given by

$$\psi(x,t) = e^{-i[\hat{H}-i\epsilon(x)]t/\hbar}\psi(x,0). \tag{2.125}$$

Now we can imagine looking at the probability density for this wavefunction which is given by

$$\begin{aligned} |\psi(x,t)|^2 &= \psi^*(x,0)e^{i[\hat{H}+i\epsilon(x)]t/\hbar}e^{-i[\hat{H}-i\epsilon(x)]t/\hbar}\psi(x,0), \\ &\simeq e^{-\epsilon(x)t/\hbar}|\psi(x,0)|^2, \end{aligned} \tag{2.126}$$

where in the last equality here we have assume the Hamiltonian and absorbing potential commute. While this is generally not true, the qualitative illustration of the properties of this negative imaginary is still valid. We see first that under the modified Hamiltonian, probability is not conserved. The norm of the wavefunction is reduced exponentially with ϵ. In addition we see that the "absorbed" amplitude is position dependent: the amplitude is not damped where $\epsilon(x) = 0$ and is damped more strongly where $\epsilon(x)$ is larger.

Necessary Properties and Convergence

The desired property of an absorbing potential is simply stated: an optimal absorbing potential must absorb all outgoing flux without causing reflection. This succinct description, however, does not immediately lead to an obvious method for choosing an appropriate absorbing potential. It should be clearly stated that there is not a *unique*, optimal absorbing potential. In fact, different choices of functional form, or even different parameters for the same functional form may work just as well for a specific problem. The goal in the present work is to obtain reaction probabilities to moderate ($\sim$ 3 or 4 significant digits, less than 1% error) rather than high accuracy ($\sim$ 6 or more significant digits). Thus, obtaining appropriate absorbing potentials for this purpose does not necessitate a complex scheme for minimizing reflection, but rather one wishes simple guidelines for choosing an adequate and easily converged potential.

One key consideration is that low translational energies present a more severe test in that the amplitude is much more easily reflected. These energies therefore require a very smoothly and slowly increasing absorbing potential to avoid reflection. This is in strong contrast to the case of high translational energy where the absorbing potential must turn on strongly in order to absorb all the flux before the end of the grid is reached. In fact, both of these cases can occur at the same time. Consider the collinear H + H_2 reaction for the case where an initial state-selected probability is desired. If the total energy is about 0.8 eV, then the translational energy for the $H_2(v = 0)$ state is very high, about 0.53 eV while for $H_2(v = 1)$ the translational

energy is less than 0.02 eV. Indeed, the probabilities for energies near the threshold for an excited state are the hardest to converge. An optimal absorbing potential in this situation must simultaneously satisfy the two, seemingly contradictory, criterion mentioned above.

Convergence is obtained by, loosely speaking, taking the $\epsilon \rightarrow 0^+$ limit. If the absorbing potential is taken as an infinitesimal constant everywhere, the correct Green's function will result but only if the "finite" basis is extended infinitely far into the asymptotic valleys. One can picture "rolling up" the asymptotic edges of the absorbing potential and moving them inward until the absorbing potential begins to interfere with the dynamics. Convergence is typically achieved by doing the reverse — the absorbing potential is placed close to the interaction region and moved outward and made shallower until the calculated result no longer changes. As a rough guideline, this procedure usually places the beginning of the absorbing strip at the point where the interaction potential, $V - V_{asym}$, equals zero. The maximum value of the potential is typically taken to be one to two times the scattering energy and the answer is often relatively insensitive to this.

Functional Forms

The most frequently used functional form for absorbing potentials in time-dependent and time-independent problems seems to be a power law dependence. That is, the absorbing potential is given roughly as

$$\epsilon_n(R) = \lambda \left(\frac{R - R_0}{R_{max} - R_0} \right)^n , \tag{2.127}$$

where typically n is between 1 and 6. In the present work we have used a quartic potential ($n = 4$). This potential has a slow initil turn on, to prevent reflection of the low translational energy components, and then rises strongly to absorb the higher energy amplitude.

The Woods-Saxon potential,

$$\epsilon_{WS}(R) = \frac{2\lambda}{1 + \exp[(R_{max} - R)/\eta]}, \tag{2.128}$$

is another useful form for the absorbing potential. In this case, the absorbing potential is not explicitly zero in the interaction region but is exponentially decaying (though it is usually set to zero). While the Woods-Saxon potential levels off at large R (it is a prelimit Heaviside step function) the end of the grid is placed where the potential equals λ. A drawback with this potential is the sensitivity to the parameter η which can make convergence somewhat more difficult.

2.7 Appendix II: Semiclassical Reaction Probabilities

In Section 2.2.3 we have shown that, within the absorbing boundary conditions formalism, the initial state-selected reaction probability can be expressed as

$$P_{n_r}(E) = \frac{2}{\hbar} \langle \Phi_{n_r} \mid \hat{\epsilon}_r \, \hat{G}^{+*}(E) \, \hat{\epsilon}_p \hat{G}^{+}(E) \, \hat{\epsilon}_r \mid \Phi_{n_r} \rangle. \tag{2.129}$$

In this Appendix we wish to evaluate this expression using a semiclassical approximation for the outgoing wave Green's function. This work is an outgrowth of the research carried out by Keshavamurthy and Miller[94] in calculating the elements of the S-matrix semiclassically and Spath and Miller[123] who calculated the semiclassical cumulative reaction probability using absorbing boundary conditions.

To illustrate how the semiclassical probability is obtained, we first insert a pair of completeness relations in the position representation:

$$P_{n_r}(E) = \frac{2}{\hbar} \int dx_1 \int dx_2 \langle \Phi_{n_r} \mid \hat{\epsilon}_r \, \hat{G}^{+*}(E) \mid x_1 \rangle \langle x_1 \mid \hat{\epsilon}_p \mid x_2 \rangle \langle x_2 \mid \hat{G}^{+}(E) \, \hat{\epsilon}_r \mid \Phi_{n_r} \rangle. \tag{2.130}$$

Noting that the operator $\hat{\epsilon}_p$ is a function only of position and therefore $\langle x_1 \mid \hat{\epsilon}_p \mid x_2 \rangle = \epsilon(x_1) \, \delta(x_2 - x_1)$, we obtain

$$\begin{aligned} P_{n_r}(E) &= \frac{2}{\hbar} \int dx_1 \langle \Phi_{n_r} \mid \hat{\epsilon}_r \, \hat{G}^{+*}(E) \mid x_1 \rangle \; \epsilon_p(x_1) \; \langle x_1 \mid \hat{G}^{+}(E) \, \hat{\epsilon}_r \mid \Phi_{n_r} \rangle \\ &= \frac{2}{\hbar} \int dx_1 \; \epsilon_p(x_1) \; \left| \langle x_1 \mid \hat{G}^{+}(E) \, \hat{\epsilon}_r \mid \Phi_{n_r} \rangle \right|^2 . \end{aligned} \tag{2.131}$$

Insertion of another completeness relation inside the absolute square gives

$$P_{n_r}(E) = \frac{2}{\hbar} \int dx_1 \; \epsilon_p(x_1) \left| \int dx_2 \; \langle x_1 \mid \hat{G}^{+}(E) \mid x_2 \rangle \epsilon_r(x_2) \, \Phi_{n_r}(x_2) \right|^2 . \tag{2.132}$$

for the reaction probability.

At this point we introduce the semiclassical approximation for the Green's function. Recall that the Green's function can be expressed (with the absorbing potential included) as

$$\langle x_1 | \hat{G}^+(E) | x_2 \rangle = \frac{1}{i\hbar} \int_0^\infty dt \, \langle x_1 | e^{i(E-\hat{H}+i\hat{\epsilon})t/\hbar} | x_2 \rangle. \tag{2.133}$$

The semiclassical approximation for the propagator (obtained by evaluating the Feynman path integral propagator within the stationary phase approximation) is given by

$$\begin{aligned} \langle x_1 | e^{-i(\hat{H}-i\hat{\epsilon})t/\hbar} | x_2 \rangle &= \sqrt{\frac{\partial^2 S(x_1,x_2,t)}{\partial x_2 \partial x_1}/2\pi i\hbar} \\ &\times \exp\left\{ iS(x_1,x_2,t)/\hbar - \frac{1}{\hbar}\int_0^t \epsilon(x_2(t'))\,dt' \right\}, \end{aligned} \tag{2.134}$$

where $S(x_1, x_2, t)$ is the classical action associated with a trajectory going from x_1 to x_2 in time t. We note, however, that

$$\frac{\partial S(x_1,x_2,t)}{\partial x_1} = p_1 \quad \Rightarrow \quad \frac{\partial^2 S(x_1,x_2,t)}{\partial x_2 \partial x_1} = \frac{\partial p_1}{\partial x_2}, \tag{2.135}$$

which gives the initial state-selected probability as

$$\begin{aligned} P_{n_r}(E) &= \frac{2}{\hbar} \int dx_1 \, \epsilon_p(x_1) \left| \frac{i}{\hbar} \int dx_2 \int dt \sqrt{\frac{\partial p_1}{\partial x_2}/2\pi i\hbar} \right. \\ &\times \left. \exp\left\{ iS(x_1,x_2,t)/\hbar - \frac{1}{\hbar}\int_0^t \epsilon(x_2(t'))\,dt' \right\} \epsilon_r(x_2)\,\Phi_{n_r}(x_2) \right|^2. \end{aligned} \tag{2.136}$$

This expression requires that one find trajectories that start in the product absorbing strip ($\epsilon_p(x_1) \neq 0$) and end up in the reactant absorbing strip ($\epsilon_r(x_1) \neq 0$) after time t. The integrals are computed over starting positions (x_1), ending positions (x_2), and transit times (t). This approach is somewhat lacking in that it specifies trajectories by double-ended boundary conditions: $x(t; x_1, x_2)$. Thus one has to solve the notorious root search problem of finding $x(t; x_1, p_1) = x_2$ for p_1, where p_1 is the initial momentum of the trajectory. While this can be accomplished for one, two, and possibly three degrees of freedom it becomes increasingly difficult as the size of the system increases, and for large systems is not feasible.

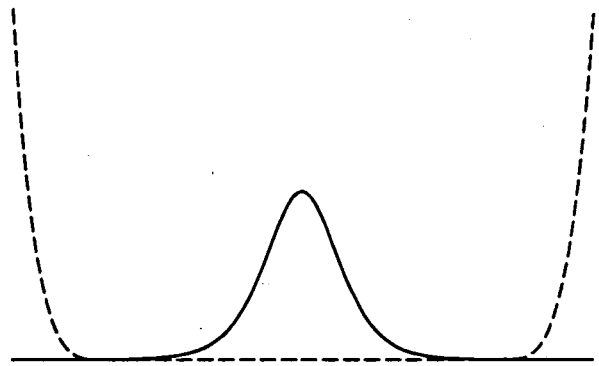

Figure 2.14: A plot of the Eckart barrier and the absorbing potential used in the calculation of the semiclassical initial state-selected reaction probabilities. The Eckart potential is shown as the solid line and the absorbing potential as the dashed line. For reference, the barrier is centered at $s = 0$ and the absorbing potentials here begin at $s = 4$ a.u. and end at $s = 6$ a.u.

Fortunately an approach is available to circumvent this problem — the initial value representation (IVR). Simply put, one makes a change of variables from x_1 and x_2 to x_1 and p_1. Then the integral over x_2 becomes

$$\int dx_2 = \int dp_1 \left| \frac{\partial x_2}{\partial p_1} \right|, \tag{2.137}$$

where $|\partial x_2/\partial p_1|$ is the Jacobian factor for the transformation. Inserting this in the expression for $P_{n_r}(E)$ gives the probability as

$$\begin{aligned} P_{n_r}(E) &= \frac{2}{\hbar^3} \int dx_1 \, \epsilon_p(x_1) \left| \frac{i}{\hbar} \int dp_1 \int dt \sqrt{\frac{\partial x_2(x_1,p_1,t)}{\partial p_1}} / 2\pi i\hbar \right. \\ &\times \exp\left\{ iS(x_1,p_1,t)/\hbar - \frac{1}{\hbar}\int_0^t \epsilon(x_2(x_1,p_1,t'))\, dt' \right\} \\ &\times \left. \epsilon_r(x_2(x_1,p_1,t))\, \Phi_{n_r}(x_2(x_1,p_1,t)) \right|^2 . \end{aligned} \tag{2.138}$$

Now the procedure is simpler. Trajectories, $x_2(t)$ are started in the product absorbing strip with initial conditions x_1, p_1 and the time integral is evaluated along the course

of the trajectory. Note that the trajectories will not contribute until they have reached the reactant absorbing strip, *i.e.*, until they have "reacted."

We have applied this semiclassical method to the one-dimensional symmetric Eckart barrier,

$$V(x) = V_0 \operatorname{sech}^2\left(\frac{q}{a}\right), \tag{2.139}$$

with $V_0 = 0.425$ eV, $a = 1$, and a mass of 1060. These parameters are intended to represent the profile along the reaction path of the $H+H_2$ potential. The potential and absorbing potential are shown in Figure 2.14. In this one-dimensional problem there is only one asymptotic reactant channel and the wavefunction is given by (defining reactants to the left and products to the right)

$$\Phi_E(x) = \frac{e^{ikx}}{\sqrt{v}}, \tag{2.140}$$

where $v = \hbar k/\mu = \sqrt{2E/\mu}$. This wavefunction is normalized to have unit incident flux.

Figure 2.15 shows the reaction probability as a function of energy for the Eckart barrier. The lower panel highlights the results in the deep-tunneling regime by showing the probability on a semilog plot. The semiclassical calculation reproduces the exact probability well at energies near threshold. The agreement is good over the energy range 0.25-0.8 eV. The semilog plot shows that accurate tunneling probabilities as low as $\sim 10^{-4}$ can be obtained with this method.

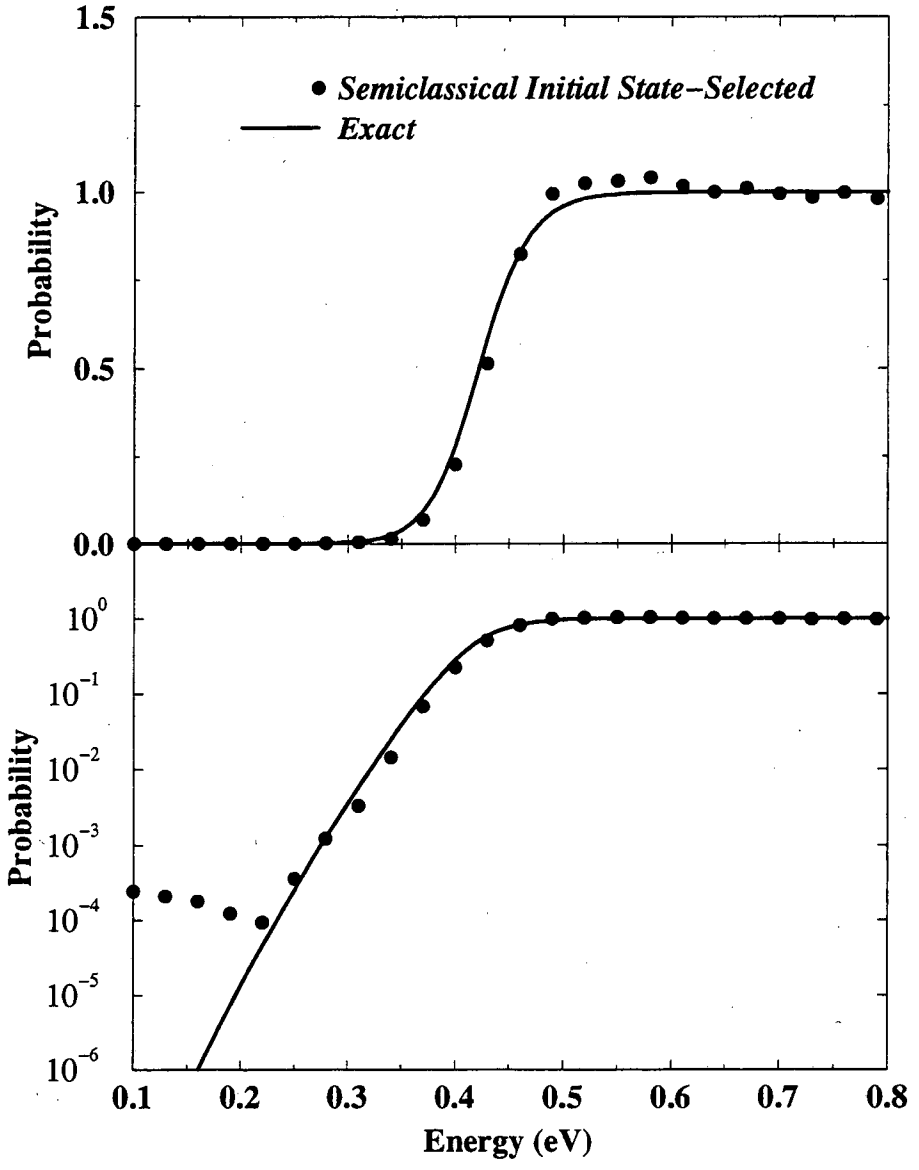

Figure 2.15: Initial state-selected probability vs. energy for the one-dimensional Eckart barrier. The semiclassical probability is shown as the filled circle, the exact results as the solid line. The upper panel shows the probability on a linear scale while the lower panel plots the results on a semilog scale to better view the agreement in the deep-tunneling regime.

Chapter 3

Photodetachment Intensities

3.1 Introduction

Photoelectron spectroscopy of negative ions has proved to be a powerful tool for probing the reaction dynamics and the potential energy surface of the corresponding neutral molecular system.[13,14] In a typical experiment, the stable anion ABC^- is photodetached by a fixed freqency laser and the kinetic energy distribution (spectrum) of the detached electron measured. In a fortuitous case, the equilibrium geometry of the anion lies directly below the transition state region of the neutral potential energy surface. Then, in the spirit of transition state theory, one would predict that the spectrum consists of a series of peaks, each corresponding to a state of the activated complex of the ABC neutral and with an intensity proportional to the Franck-Condon overlap of that state with the anion wavefunction. Since the activated complex is not a stable species (decaying to produce either the neutral products or reactants), these states have a finite lifetime which gives rise to broadening of the peaks in the spectrum. Thus the kinetic energy distribution of the detached electron gives detailed information about the the transient activated complex which is the gateway to reaction. Comparison with theoretical predictions of the spectrum constitutes a stringent test of an *ab initio* surface and provides for a detailed assessment of the crucial features of the transition state region which cannot be obtained by a comparison of reactive scattering results.

Calculations for this process were first carried out by Schatz[124] to study the hydrogen atom exchange reaction between halogen atoms, $X + HX' \rightarrow XH + X'$. More recently,[125] comparison of theoretical and experimental results were used to great effect for the $F + H_2$ reaction, leading to the accurate characterization of the transition state for that reaction. As noted in Section 2.4 the reaction

$$OH + H_2 \rightarrow H_2O + H \tag{3.1}$$

has become the benchmark of choice for quantum treatments of a four-atom reaction. Recently, de Beer *et al.*[15] have carried out photodetachment experiments and simulations of H_3O^- and D_3O^- providing information on the potential energy surface of Reaction (3.1). Despite the flurry of recent experimental and theoretical work on the $OH + H_2$ reaction, the best available potential surface[103] still contains multiple flaws. For example, the surface gives the transition state geometry as a *trans* configuration though *ab initio* calculations predict it to be *cis*; it also contains a spurious well just before the barrier on the $OH + H_2$ side, which has been partially corrected by Clary.[75] Thus, comparison of theoretical calculations on this surface with experiment may provide information useful for evaluating and improving this surface (or for producing a new potential energy surface).

The photodetachment spectroscopy of H_3O^-, however, has some aspects which make it a difficult problem. The anion has two stable geometries, $H^- \cdots H_2O$ and $HO^- \cdots H_2$ structures, neither of which lies close to the geometry of the neutral transition state.[15,126] The two anion species lead to distinctly different spectra at different laser polarizations,[15] and furthermore, excited vibrational states of the anion are delocalized over both geometries and can give Franck-Condon overlap with the transition state. An additional difficulty is the lack of knowledge of both the anion and neutral surfaces. The interpretation of the spectra is simplified if one surface is known well (or alternatively, if the spectra are insensitive to one surface), but if both surfaces are not well determined, one is limited to making statements about the similarities and differences between the surfaces.

3.2 Theory

The photodetachment intensity is given within the Franck-Condon approximation by

$$I(E) = \sum_{\mathbf{n}_\tau=\mathbf{n}_r,\mathbf{n}_p} \rho(E) \mid \langle \Psi_{\mathbf{n}_\tau}(E) \mid \phi_b \rangle \mid^2, \tag{3.2}$$

where ϕ_b is the bound state of the anion and $\Psi_{\mathbf{n}_\tau}$ is the scattering wavefunction on the neutral surface. The density of states, $\rho(E)$, is associated with the normalization of the scattering wavefunction, which for our choice of normalization is $\rho(E) = (2\pi\hbar)^{-1}$. This approximation has been shown to be very useful and accurate.[124]

In the DVR-ABC approach outlined in Section 2.2.3, the Lippmann-Schwinger-type equation

$$\mathbf{\Psi}_{\mathbf{n}_\tau}(E) = i\mathbf{G}^+(E) \cdot \boldsymbol{\epsilon}_\tau \cdot \mathbf{\Phi}_{\mathbf{n}_\tau}(E), \tag{3.3}$$

is used to obtain the reactive scattering wavefunction. The bound state DVR vector can be obtained by solving a vibrational eigenvalue problem on the anion potential energy surface using the same basis as for the scattering wavefunction. The Franck-Condon intensity is then given by

$$I(E) = \frac{1}{2\pi\hbar} \sum_{\mathbf{n}_\tau=\mathbf{n}_r,\mathbf{n}_p} \boldsymbol{\phi}_b^\dagger \cdot \mathbf{G}^*(E) \cdot \boldsymbol{\epsilon}_\tau \cdot \mathbf{\Phi}_{\mathbf{n}_\tau}^\dagger \mathbf{\Phi}_{\mathbf{n}_\tau} \cdot \boldsymbol{\epsilon}_\tau \cdot \mathbf{G}(E) \cdot \boldsymbol{\phi}_b. \tag{3.4}$$

However, one can make use of the closure relation derived in Section 2.2.3 to obtain the following simpler result,

$$I(E) = \frac{1}{\pi} \boldsymbol{\phi}_b^\dagger \cdot \mathbf{G}^*(E) \cdot \boldsymbol{\epsilon} \cdot \mathbf{G}(E) \cdot \boldsymbol{\phi}_b, \tag{3.5}$$

for the total photodetachment intensity. Moreover, since the full absorbing potential can be written as the sum of the absorbing potentials in the reactant and product arrangements, $\boldsymbol{\epsilon} = \boldsymbol{\epsilon}_r + \boldsymbol{\epsilon}_p$, one can divide the intensity into the parts due to the neutral dissociating into reactants and the part dissociating into products (that is, *arrangement-selected* intensities). Then the contribution to the photodetachment intensity from a given arrangement τ is given by

$$I_\tau(E) = \frac{1}{\pi} \boldsymbol{\phi}_b^\dagger \cdot \mathbf{G}^*(E) \cdot \boldsymbol{\epsilon}_\tau \cdot \mathbf{G}(E) \cdot \boldsymbol{\phi}_b. \tag{3.6}$$

The total intensity can subsequently be obtained as

$$I(E) = \sum_{\tau} I_{\tau}(E). \tag{3.7}$$

Alternatively, starting again from Eq. (3.2), we can use the completeness relation for the scattering wavefunction:

$$\sum_{\mathbf{n}_\tau = \mathbf{n}_r, \mathbf{n}_p} \rho(E) \mid \Psi_{\mathbf{n}_\tau}(E)\rangle\langle\Psi_{\mathbf{n}_\tau}(E) \mid = \delta(E - \hat{H}). \tag{3.8}$$

The right hand side is just the microcanonical density operator which can be expressed in terms of the outgoing wave Green's function

$$\delta(E - \hat{H}) = -\frac{1}{\pi}\mathrm{Im}\ \hat{G}^{+}(E). \tag{3.9}$$

This gives us an alternative, direct way to calculate the total photodetachment intensity. In the DVR-ABC formulation this is given by

$$I(E) = -\frac{1}{\pi}\mathrm{Im}\ \boldsymbol{\phi}_b^{\dagger} \cdot \mathbf{G}^{+}(E) \cdot \boldsymbol{\phi}_b. \tag{3.10}$$

Note that both Eq. (3.6) and Eq. (3.10) require the same amount of computational work: the action of the Green's function onto a single vector. Thus, the direct and arrangement-selected photodetachment intensities can be computed simultaneously with no extra work. Additionally, the intensity obtained from Eq. (3.7) can be compared to that from Eq. (3.10) as a test of the convergence of the Green's function.

3.3 Eckart Barrier Model

An illustrative example is provided by calculating photodetachment intensities for a model one-dimensional system where the anion is represented by a harmonic oscillator and the neutral by the Eckart barrier potential. (Recall the Eckart barrier with an absorbing potential is pictured in Fig. 2.14.) We have used the method described above in Section 3.2 to obtain the total and arrangement-selected photodetachment spectra for this model problem. The parameters used for the Eckart barrier are the same as given in Section 2.7 and the anion harmonic oscillator frequency is taken to be 3000 cm^{-1}.

Figure 3.1 shows the calculated total and arrangement-selected photodetachment spectra for this model problem. The spectra have been calculated for different positions of the anion equilibrium distance, r_0, relative to the top of the barrier. The barrier is centered at $s = 0$ and for $r_0 = 0$ the equilibrium geometry of the harmonic oscillator anion coincides with the top of the barrier. For $r_0 = 1$ and 2 a.u., the anion equilibrium geometry is displaced towards products. A check on the convergence of the calculated spectra is the integral of the total photodetachment intensity — this should be one with the energy in atomic units (or 27.21 eV if the energy is given in electron volts as shown here).

The spectra for r_0 has several interesting features. The total intensity is a single broad peak centered at about E = 0.43 eV. Recall that the barrier height in this case is 0.425 eV. This is expected as the scattering wavefunctions on the neutral surface will have exponentially decaying tails in the region of the barrier for energies below the barrier height. Since the Franck-Condon overlap in this case is predominantly in the barrier region, one might predict that the intensity would be largest at an energy above the barrier height. Note that the intensity has a somewhat longer tail at higher energies than at lower energies. Another interesting feature involves the arrangement-selected intensities which in this case are identical. This is due to the symmetry of both the barrier and the anion wavefunction about $s = 0$ in this case.

An interesting development is observed when the anion equilibrium geometry is displaced towards products. A nodal structure appears in the spectra, the maximum intensity moves to lower energies, and the highest energy at which intensity is observed is smaller. In addition, the intensity leading to reactants decreases dramatically and is virtually zero for the $r_0 = 2$ a.u. case. All of these features can be explained by a simple picture of the changing Franck-Condon overlap as the anion geometry is displaced. The Franck-Condon overlap becomes stronger with the scattering wavefunction of the neutral at lower energies as the anion geometry is moved away from the barrier. Thus, the intensity peaks at lower energies and reactants can be formed only by tunneling. Note that the reactant-selected intensity for the $r_0 = 1$ a.u. case begins around E = 0.38 eV. The nodal structure can be attributed

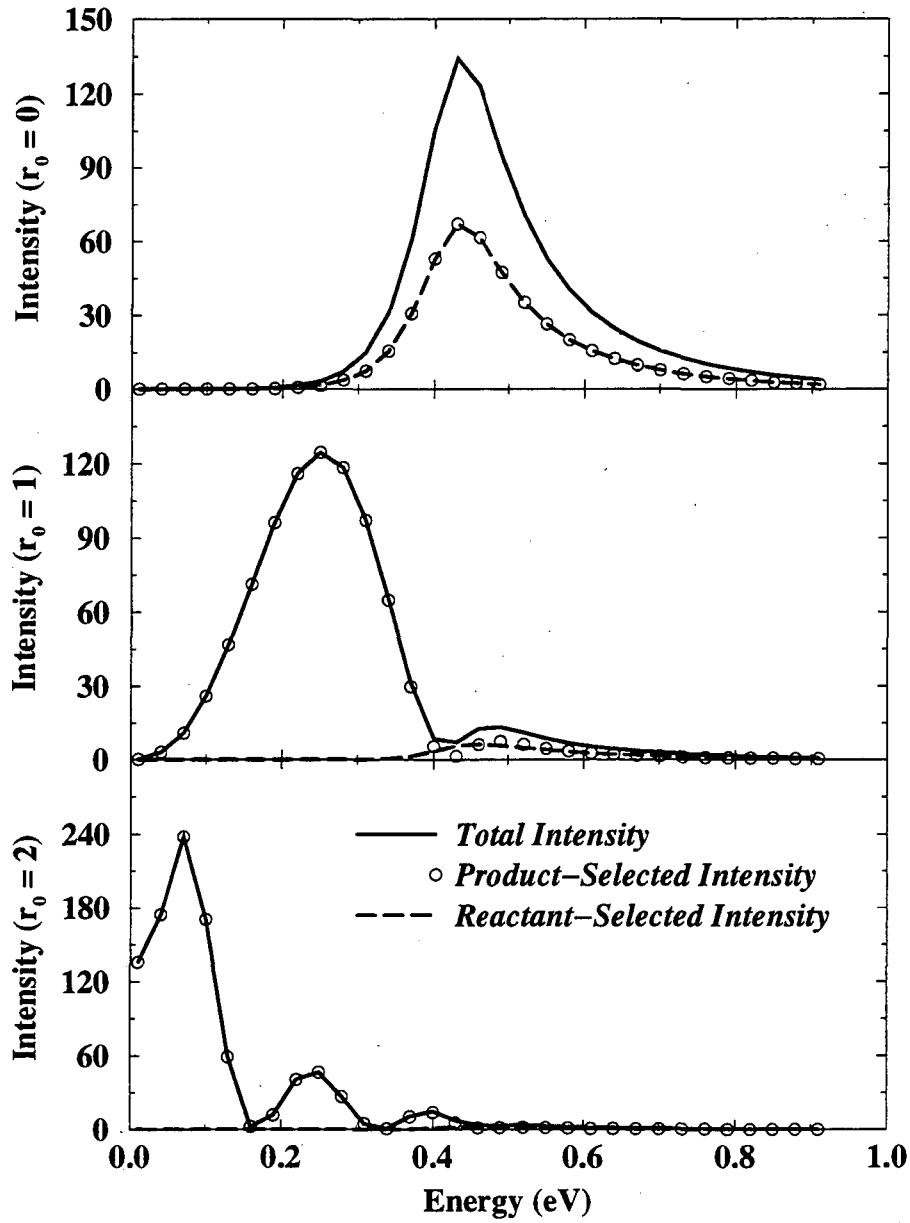

Figure 3.1: Photodetachment spectra for the one-dimensional model problem with a harmonic oscillator anion and a neutral potential given by the Eckart barrier. The spectra are given for different values of the anion equilibrium distance, r_0, relative to the top of the Eckart barrier. Note that for $r_0 = 0$, the product- and reactant-selected spectra are indistinguishable.

to interference between amplitude which reflects off the barrier and amplitude which directly moves off towards products. The same pattern, including the increasing number of nodes with larger displacement, can be observed in the case where the neutral potential is replaced by a free particle potential with an infinite wall at $s = 0$.

3.4 Photodetachment of H_3O^-

3.4.1 Details of the Calculation

We have chosen to use the Jacobi coordinates of the reactants as shown in Figure 2.10: r_1 and r_2 denote the H_2 and OH bond distances, respectively, R the distance between the H_2 and OH centers-of-mass, γ_1 the angle between $\mathbf{r}_1$ and $\mathbf{R}$, γ_2 the angle between $\mathbf{r}_2$ and $\mathbf{R}$, and φ the torsional angle.

The calculations presented here treat either two or four degrees of freedom explicitly. In all cases, the OH bond distance is frozen at its equilibrium value, $r_2^0 = 1.8633$ $a.u.$ and the torsional angle is fixed at $\varphi^0 = 0$, *i.e.*, the planar configuration. These values give the proper transition state geometry for the reaction. As shown in Section 2.4, calculations of reaction probabilities with these coordinates fixed give all the qualitative features of a full six degree of freedom treatment. Here we make no attempt to incorporate the effects of these two neglected coordinates under the assumption that the zero point energies are the same in the anion and neutral.

Our calculations have used the WDSE potential energy surface for the neutral. (See Fig. 2.8.) For the anion surface, we have used the surface of de Beer *et al.*[15], shown in Fig. 3.2, that provides a global anharmonic description of the two coordinates r_1 and R. This anion surface has two minima. The global minimum is an $H^- \cdots H_2O$ structure under the $H + H_2O$ (product) valley of the neutral surface. The other local minimum lies under the $OH + H_2$ (reactant) valley at an $HO^- \cdots H_2$ structure. The energy of the local minimum with the $HO^- \cdots H_2$ geometry is 0.085 eV higher than that of $H^- \cdots H_2O$.[15] The ground state wavefunction on this potential energy surface is localized in the $H^- \cdots H_2O$ well, while excited states with $\nu \geq 2$ are delocalized across both wells. Very little information is available about the potential

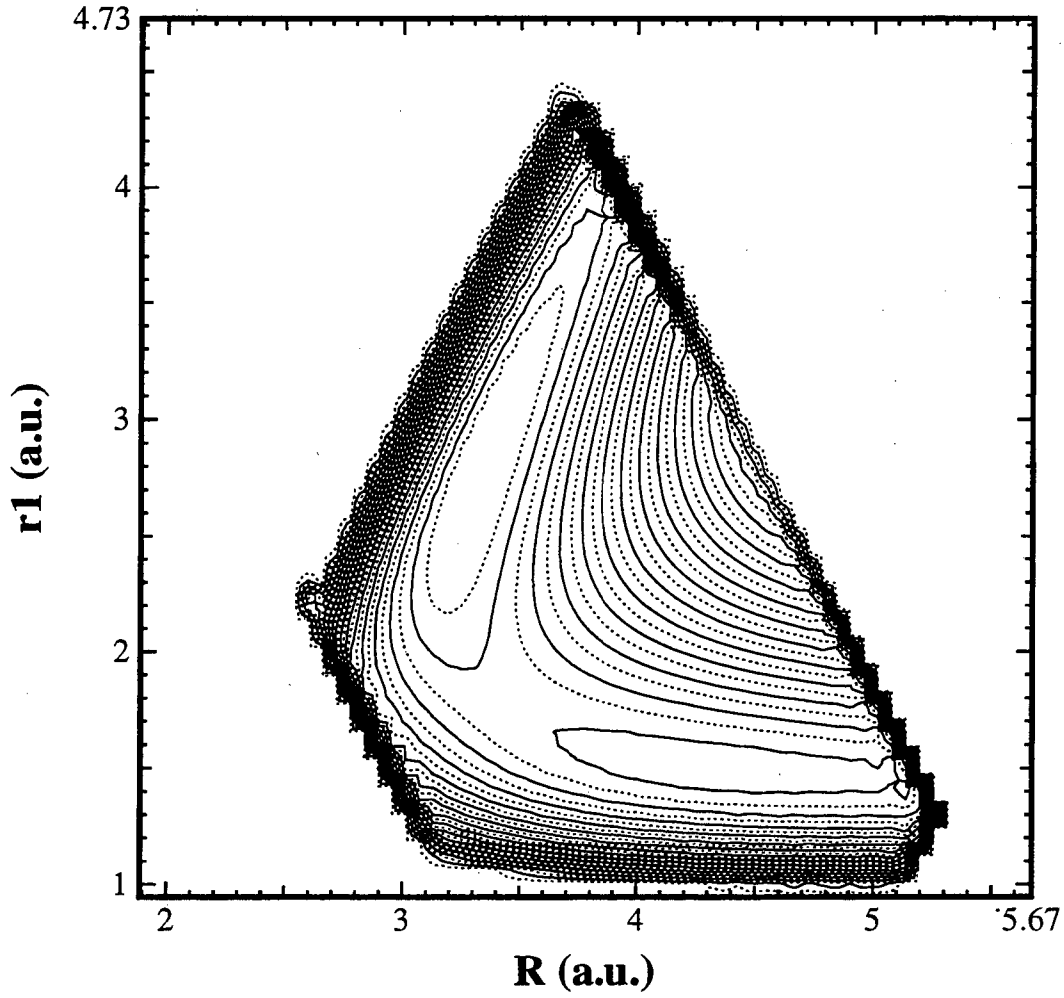

Figure 3.2: Two degree of freedom contour plot of the H_3O^- anion potential energy surface. Here R is the distance between the OH and H_2 centers-of-mass and r_1 is the H_2 bond distance. The contour spacing is 0.06 eV.

in the angular (bending) coordinates. Consequently, we use separable harmonic oscillator bending potentials. The frequencies are taken from the *ab initio* calculations of Xantheas and Dunning.[126] The equilibrium bending angles are varied, and the effects on the resulting spectra are discussed below.

In addition to these calculations on the H_3O^- potential, *ab initio* results at the CCSD(T) aug-cc-pVTZ level by Mielke[127] find the equilibrium geometries in good agreement with those of de Beer *et al.*[15]

Clary and co-workers have carried out reduced-dimensionality *ab initio* calculations for the anion and neutral potentials including two stretching modes (the H_2 vibration and the scattering coordinate of OH + H_2) and the OH bend. They have obtained the photodetachment spectrum on these two surfaces using the rotating bond approximation.[128] They find good agreement between their theoretical spectra and that of the experiment. Of particular note is the excellent match between the calculated and experimental electron binding energies. This is presumably due to the higher quality *ab initio* results.

No fit exists for the anion surface, only the value of the potential on a grid of points in the r_1 and R coordinates. We have used interpolation to obtain the potential at points within the boundary of the grid. Points outside the boundary are set to a large (constant) value.

For the two and four degree of freedom calculations of the photodetachment intensities presented here we have used the same Hamiltonians, basis sets, and absorbing potentials as described in Sections 2.4.2 and 2.4.3.

Acting the Green's Function

To calculate the photodetachment spectra one needs to evaluate the action of a Green's operator onto $\phi_{\mathbf{b}}$, the anion bound state,

$$\mathbf{G}^+(E) \cdot \phi_{\mathbf{b}} = \mathbf{x} \tag{3.11}$$

which can be done by solving the linear system

$$(E - \mathbf{H} + i\epsilon) \cdot \mathbf{x} = \phi_{\mathbf{b}} \tag{3.12}$$

For multidimensional problems the size of the Hamiltonian is often too large to be stored in core memory. When this is the case, sparse matrix methods provide a useful solution. In particular, Krylov subspace methods such as the generalized minimal residual[129] (GMRES) and the quasi-minimal residual[130] (QMR) methods have been found to be quite effective. They are based on the matrix-vector multiplication. A Krylov space is formed by multiplying the matrix repeatedly onto a vector and the required linear algebra problem is solved in this space (see the discussion of the Lanczos method in Section 4.2.2). The DVR basis is well suited for such schemes as the Hamiltonian is sparse in a multidimensional case. A practical difference between these two methods (for the more fundamental differences, we refer the reader to the literature[129–131]) is that each Krylov vector in GMRES is explicitly orthogonalized to every previous vector (all of which are stored). In the QMR approach, each Krylov vector is only orthogonalized with the last few preceeding vectors. While this means GMRES displays faster convergence with the number of iterations (Krylov vectors), it also requires more memory and each iteration is slower than the previous one. Hence, in this work we have chosen to use the QMR method.

A special feature of the photodetachment spectra calculations is that the intensity is required for many energies ($\sim 130 - 300$). In addition, the action of the Green's function is only required onto one vector, the anion bound state. Thus, such a system is amenable to a multiply-shifted QMR[132] (MSQMR) approach. In this method, a single, common Krylov basis is formed and used to obtain $\mathrm{G}^+(E) \cdot \phi_b$ for all the desired energies. This is possible because the Krylov basis is invariant under shifts by a scalar. Convergence can be checked using an upper bound to the residual that provides a good estimate of the true error.

The two degree of freedom photodetachment intensities shown were calculated for 300 energies at one time. The CPU time on a RISC/6000 Model 590 was approximately 2 minutes. This represents a reduction by a factor of at least 40 in CPU time as compared to running each energy independently. The four degree of freedom intensities were calculated at about 130 energies. The total energy range was broken up into four or five segments for which up to 50 energies were computed at one time. These smaller energy ranges were required by the larger spectral range of

the 4D Hamiltonian whichs slows convergence.

Obtaining the Anion Bound State

We have used a Lanczos scheme[133] applicable to a fully coupled potential to obtain the bound state wavefunction. (See Section 4.2.2 for a description of the Lanczos algorithm.) A new Hamiltonian is formed, $\hat{H}_{anion}$ which has the same kinetic energy as $\hat{H}$ but the neutral potential is replaced by $V_{anion}(r_1, R, \gamma_1, \gamma_2; \gamma_1^0, \gamma_2^0)$. Here γ_1^0 and γ_2^0 are the equilibrium bending angles for the anion. Note that this Hamiltonian is real symmetric. A Krylov space is formed with reorthogonalization to all previous vectors. The Lanczos algorithm is used to obtain the lowest eigenvalues and eigenvectors. (Typically the number of Lanczos iterations needed is between 100 and 140.) The eigenvectors are examined to determine the vibrational state in the coupled r_1 and R coordinates.

3.4.2 Results and Discussion

Recently, de Beer *et al.*[15] presented experimental photodetachment spectra of H_3O^- and D_3O^- as well as two degree of freedom simulation results. The experimental spectra were taken at two laser polarizations $\theta = 0^o$ and $\theta = 90^o$. The $\theta = 0^o$ spectra was attributed to the $H^- \cdots H_2O$ anion structure and consist of three peaks at electron binding energies of 1.53, 2.00, and 2.38 eV. (For $D^- \cdots D_2O$ the peaks occur at 1.53, 1.88, and 2.17 eV.) These peaks were assigned to the stretching progression of the $OH(OD)$ local mode stretch in the neutral and denoted (000), (001), and (002), respectively. [This is the notation for H_2O vibrations: (n_1, n_2, n_3) where n_1 is the symmetric stretch, n_2 the bend, and n_3 the asymmetric stretch quantum number.] The peak lineshapes have some asymmetry indicating possible excitation of the n_2 bending mode. The $\theta = 90^o$ spectra are qualitatively different with broad peaks at 1.53 and 2.05 eV. These peaks are not shifted upon deuteration.

The simulations of de Beer *et al.*[15] explicitly treated the $HO-H$ and $H-H$ bonds. They performed *ab initio* calculations to obtain the anion potential as a function of these two coordinates. Their simulated spectra reproduce the main features

of the experimental results. The $\theta = 0^o$ spectra correspond to the photodetachment from the $\nu = 0$ state of the anion which is completely localized in the $H^- \cdots H_2O$ well. In contrast, the $\theta = 90^o$ spectra are attributed to the $v = 2$ state of the anion; this is the first state delocalized across both geometries of the anion. The peak at 2.05 eV is due to excitation from the $HO^- \cdots H_2$ structure. In this section we present the theoretical photodetachment spectra obtained from explicitly treating two and four degrees of freedom as described in Sections 2.4.2 and 2.4.3.

Clary and co-workers have carried out reduced-dimensionality *ab initio* calculations for the anion and neutral potentials including two stretching modes (the H_2 vibration and the scattering coordinate of OH + H_2) and the OH bend. They have obtained the photodetachment spectrum on these two surfaces using the rotating bond approximation.[128] They find good agreement between their theoretical spectra and that of the experiment. Of particular note is the good agreement between the (absolute) electron binding energies in the calculated and experimental spectra. This may be due to the more accurate *ab initio* calculations.

Two Degrees of Freedom

We have performed the two degree of freedom calculations described in Section 2.4.2 for the few lowest eigenstates of the anion. The purpose of presenting two degree of freedom results here is twofold: (1) to show that, though the coordinates and method are different, our results are consistent with those of de Beer *et al.*,[15] and (2) to illustrate the basic features of the photodetachment spectra which can be compared with higher dimensional results.

Figure 3.4 shows the 2D total and arrangement-selected photodetachment spectra from the $\nu = 0$ state of the anion for (a) H_3O^-, and (b) D_3O^-. Note that the energy of the separated reactants $OH + H_2$ is the zero of energy on the neutral potential energy surface. The lowest possible scattering energy is then -0.64 eV which is the exoergicity of the reaction.[103] For these calculations the OH and H_2 angles were set equal to the equilibrium values for the $H^- \cdots H_2O$ structure, $\gamma_1^0 = 175.9^o$ and $\gamma_2^0 = 104.8^o$. A contour plot of the $\nu = 0$ anion bound state wavefunction is shown

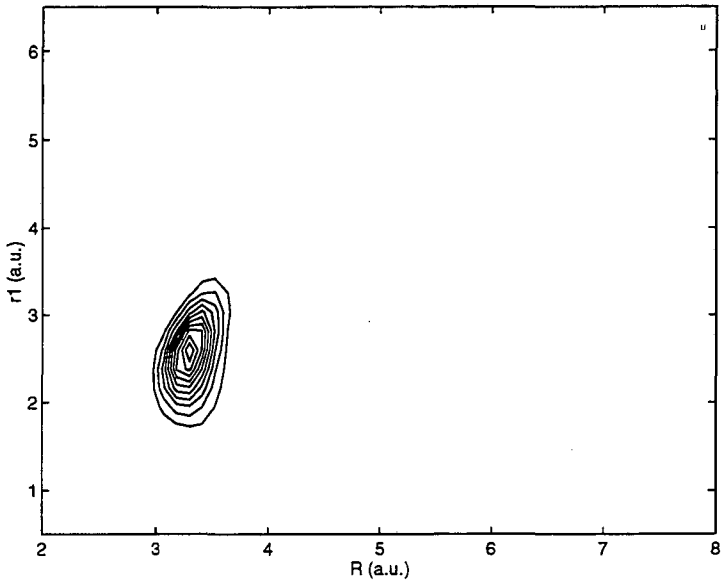

Figure 3.3: Two degree of freedom contour plot of the $\nu = 0$ bound state wavefunction for the H_3O^- anion.

in Figure 3.3. Comparing this with Fig. 2.8 shows that this anion state is localized under the $H + H_2O$ valley.

The spectra in Fig. 3.4 show the three peaks attributed to the local mode $OH(OD)$ stretch in the neutral H_2O (D_2O). The experimentally observed (000) $\rightarrow$ (001) and (001) $\rightarrow$ (002) peak spacings are 0.47 and 0.38 eV (0.35 and 0.29 eV) for the H_3O^- (deuterated) spectrum. Our calculated spectra are in good agreement giving spacings of 0.46 and 0.30 eV (0.36 and 0.25 eV deuterated).

These spectra are in reasonable agreement with the simulations of de Beer *et al.*[15] indicating our choice of somewhat different coordinates is not significant. The primary difference is the relative intensity of the (001) peak in the H_3O^- spectrum is larger than they observed. (Both simulations show a larger relative intensity for this peak than seen in the experiment.) Another difference is the dip in the (002) peak of the H_3O^- spectrum. This dip appears at the energy of the $H_2(v = 1)$ vibrational level.

The arrangement-selected intensities show that most of the intensity leads to the formation of $H + H_2O$ products. This would be expected from the position of the Franck-Condon region. However, we do see some intensity leading to the formation

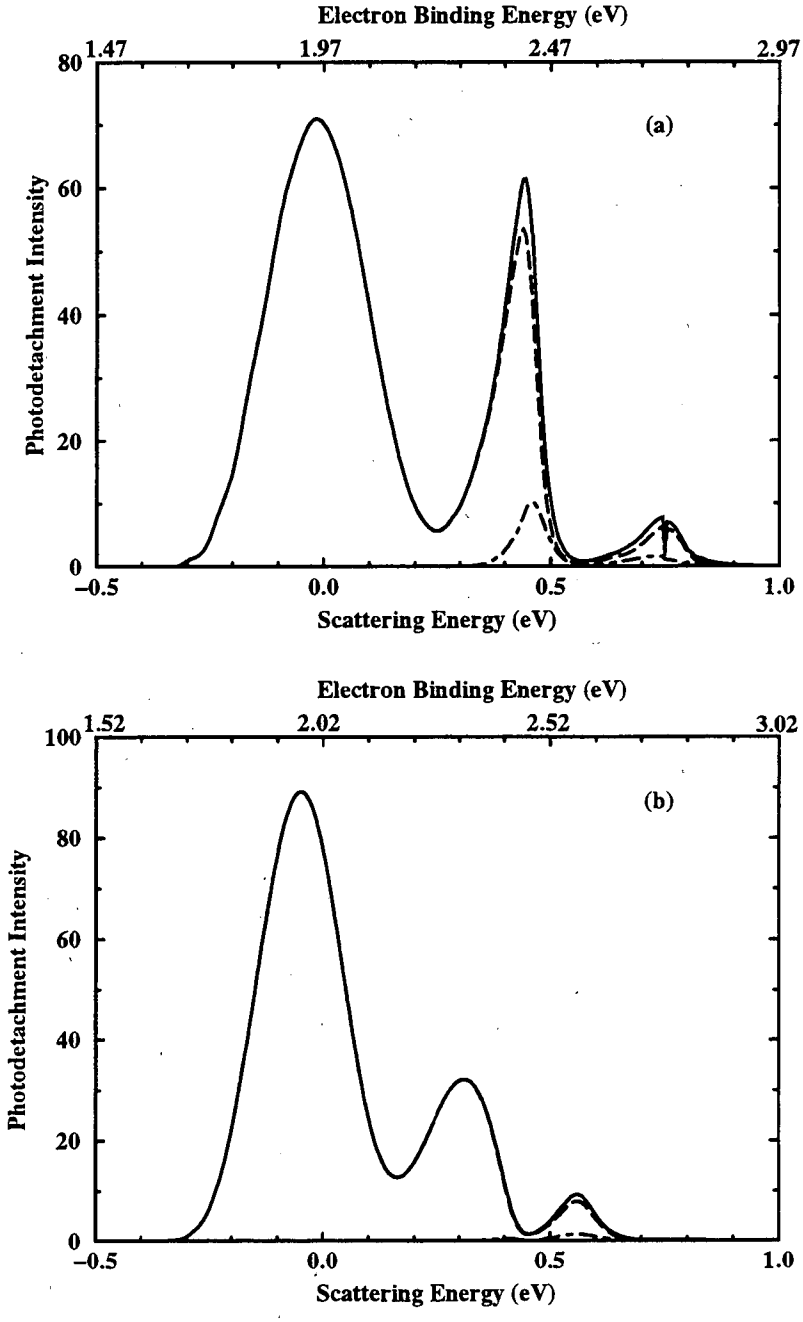

Figure 3.4: Two degree of freedom photodetachment intensities from the $\nu = 0$ state of the anion for (a) H_3O^- and (b) D_3O^-. The solid line is the total intensity, the dashed line is the product-selected intensity, and the dot-dashed line is the reactant-selected intensity.

of the $OH + H_2$ reactants. Since there is no Franck-Condon overlap on the reactant side of the barrier in this case this must occur by passing over the barrier. For the deuterated case virtually no reactants are formed. This can be explained by the fact that the energy local OD stretch levels are lower in energy thus most of the intensity is energetically forbidden from passing over the barrier.

The results of the experiment are given in electron binding energy (eBE). The conversion to the eBE from the scattering energy, E, is given by

$$eBE = E + E_A + D_e - E_\nu^-, \tag{3.13}$$

where E_A is the electron affinity of OH, D_e is the dissociation energy of $H^-(H_2O)$ to obtain $HO^- + H_2$, and E_ν^- is the vibrational energy of the anion. de Beer *et al.*[15] give $E_A = 1.83$ eV and $D_e = 0.325$ eV. Alternatively, the eBE can also be calculated by using the electron affinity of H, 0.75 eV, and the dissociation energy of $H^-(H_2O)$ to give $H_2O + H^-$, calculated to be 0.79 eV. This gives a slightly different number by about 0.03 eV. (We have used the first method.) The uncertainty lies in the dissociation energies as discussed by de Beer *et al.*[15] We will address this in Section 3.4.2. As seen from Fig. 3.4, our calculations give the first peak centered at 1.95 eV and 1.97 eV for H_3O^- and D_3O^-, respectively. This compares to the experimental value of 1.53 eV for both. We will discuss this discrepancy in Section 3.4.2.

The photodetachment spectra for (a) H_3O^- and (b) D_3O^- are shown in Figure 3.6 for the $\nu = 1$ state of the anion. The bending angles are the same as in Fig. 3.4. A contour plot of the anion wavefunction for the $\nu = 1$ state is shown in Figure 3.5. This state is mostly localized under the H + H_2O side of the neutral potential energy surface, though less so than the $\nu = 0$ wavefunction. The spectra are similar to those with $\nu = 0$ except the (000) peak is split into two. The (001) peak now leads to a greater fraction of reactants formed in the case of H_3O^-, and some formation of reactants for D_3O^-. In addition, we see sharp features in the reactant spectrum at the energy that the reactants become energetically accessible and at the energy of $H_2(v = 1)$.

Figure 3.8 is the same as Figs. 3.4 and 3.6 for the $\nu = 2$ state of the anion. These spectra are significantly different from those for $\nu = 0$ and $\nu = 1$. This anion

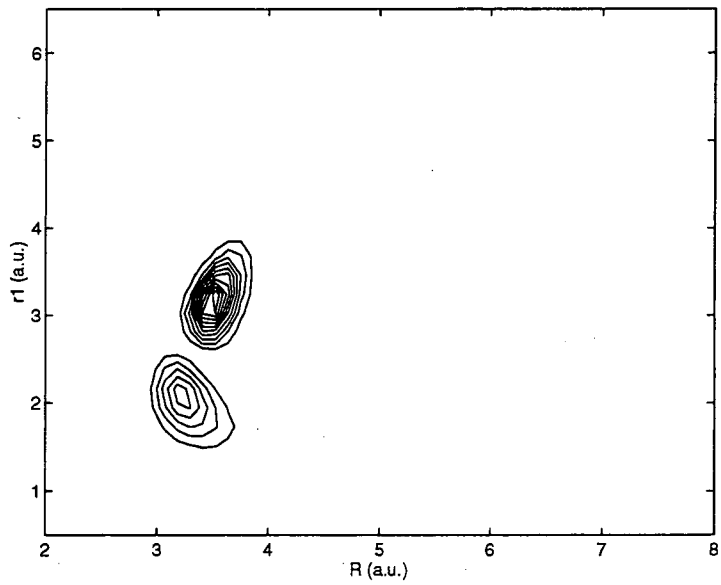

Figure 3.5: Two degree of freedom contour plot of the $\nu = 1$ bound state wavefunction for the H_3O^- anion.

wavefunction is delocalized over both the $H^- \cdots H_2O$ and $HO^- \cdots H_2$ wells as can be seen from the anion wavefunction shown in Figure 3.7. The product-selected spectra resemble somewhat that for the $\nu = 1$ state in Fig. 3.6. The spectra's dominating features are sharp and lead to the formation of reactants. This is in qualitative agreement with the results of de Beer *et al.*[15] The primary difference is the relative heights of the sharp peak at 0.29 eV and the broader peak centered around 0.4 eV. This sharp peak was attributed by de Beer *et al.* to the spurious well on the reactant side of the barrier. The feature at 0.75 eV (the energy of $H_2(v = 1)$) is observed in both calculations. We note that the broad peak is centered around 2.20 and 2.30 eV electron binding energy for H_3O^- and D_3O^-, respectively, compared with 2.05 eV as observed in the experiment.

Four Degrees of Freedom

Here we present calculations of the photodetachment intensity explicitly treating four degrees of freedom including the H_2 and OH bending angles γ_1 and γ_2 as described in Section 2.4.3. The equilibrium bending angles used for the anion

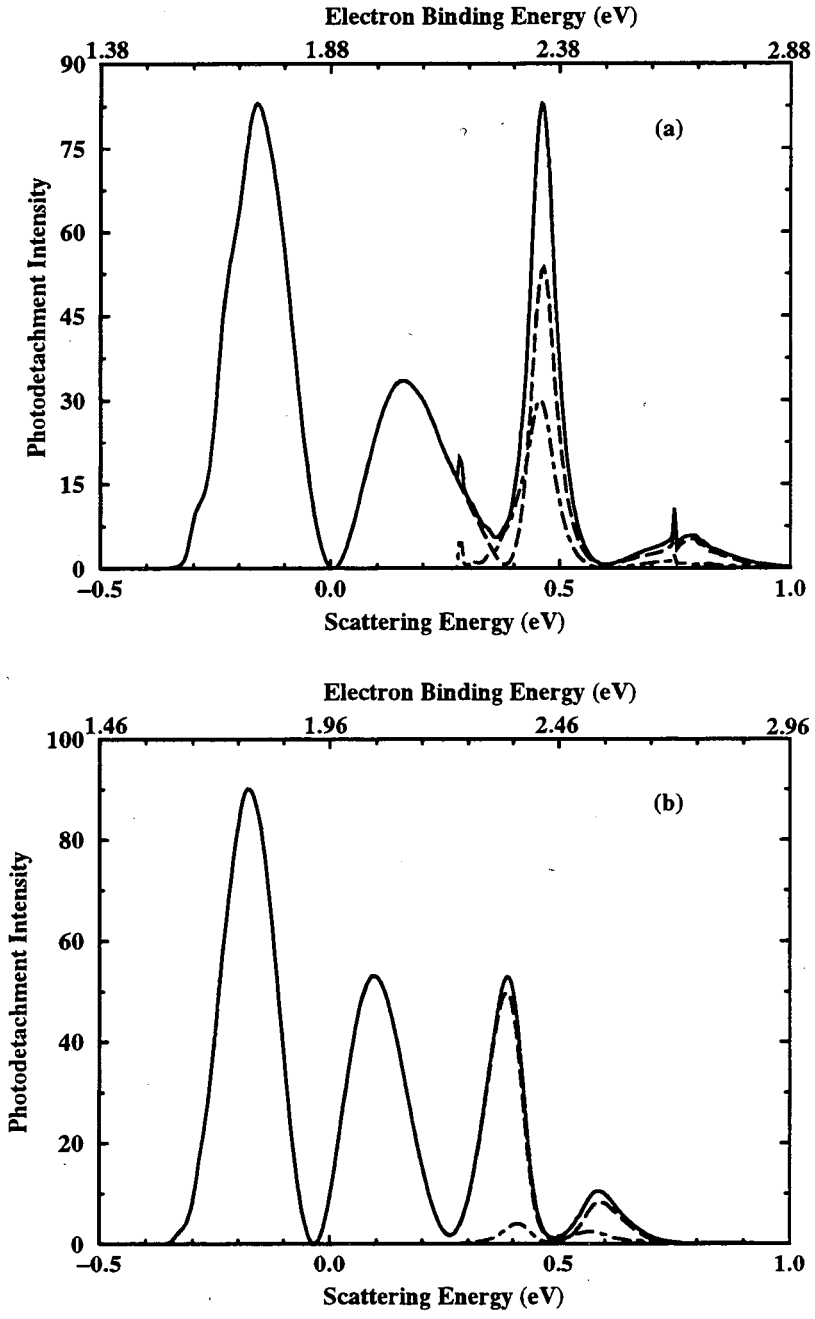

Figure 3.6: Two degree of freedom photodetachment intensities from the $\nu = 1$ state of the anion for (a) H_3O^- and (b) D_3O^-. The solid line is the total intensity, the dashed line is the product-selected intensity, and the dot-dashed line is the reactant-selected intensity.

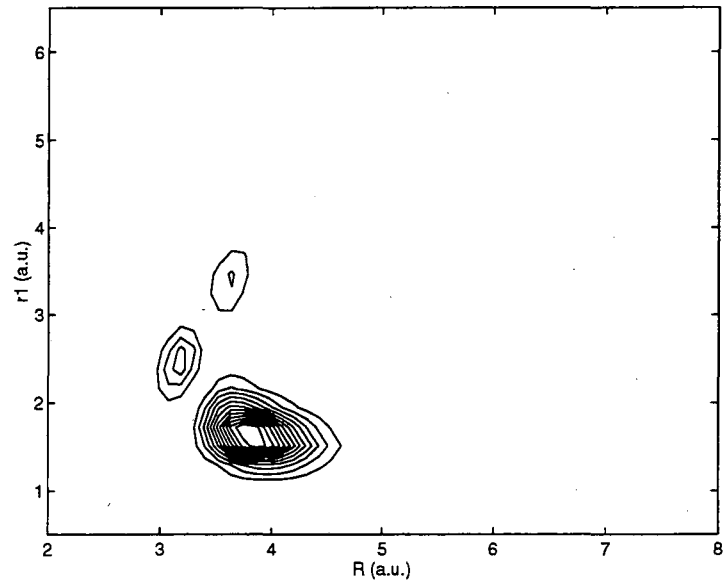

Figure 3.7: Two degree of freedom contour plot of the $\nu = 2$ bound state wavefunction for the H_3O^- anion.

potential are varied and we discuss the effect on the spectrum. All calculations were done for even parity (p=0). As mentioned above, the r_2 and φ coordinates are not expected to have a significant impact on the photodetachment spectrum. Thus the spectrum calculated with this Hamiltonian should represent the best theoretical prediction of the experimental spectrum (at least for the purposes of this paper). The comparison of the calculated spectrum with the experimental result then gives information about the accuracy (or inaccuracy) of the neutral and anion potential energy surfaces.

Figure 3.9 shows the $\nu = 0$ photodetachment spectra for (a) H_3O^- and (b) D_3O^- with anion equilibrium angles $\gamma_1^0 = 175.9^o$ and $\gamma_2^0 = 104.8^o$. The spectra are significantly different from the corresponding 2D results. The H_3O^- spectrum consists of the (000) and (001) peaks with a spacing of 0.45 eV but the peaks are much broader than in the 2D spectrum (Fig. 3.4) and there is superimposed structure due to excitation of the bending degrees of freedom. The (002) peak may be hidden by the bending progression off the (001) peak. The relative peak intensities are virtually the same as in the 2D case; the (000) peak is only slightly higher than the (001) peak. The reactant-selected intensity is small as in the 2D spectrum but is now a

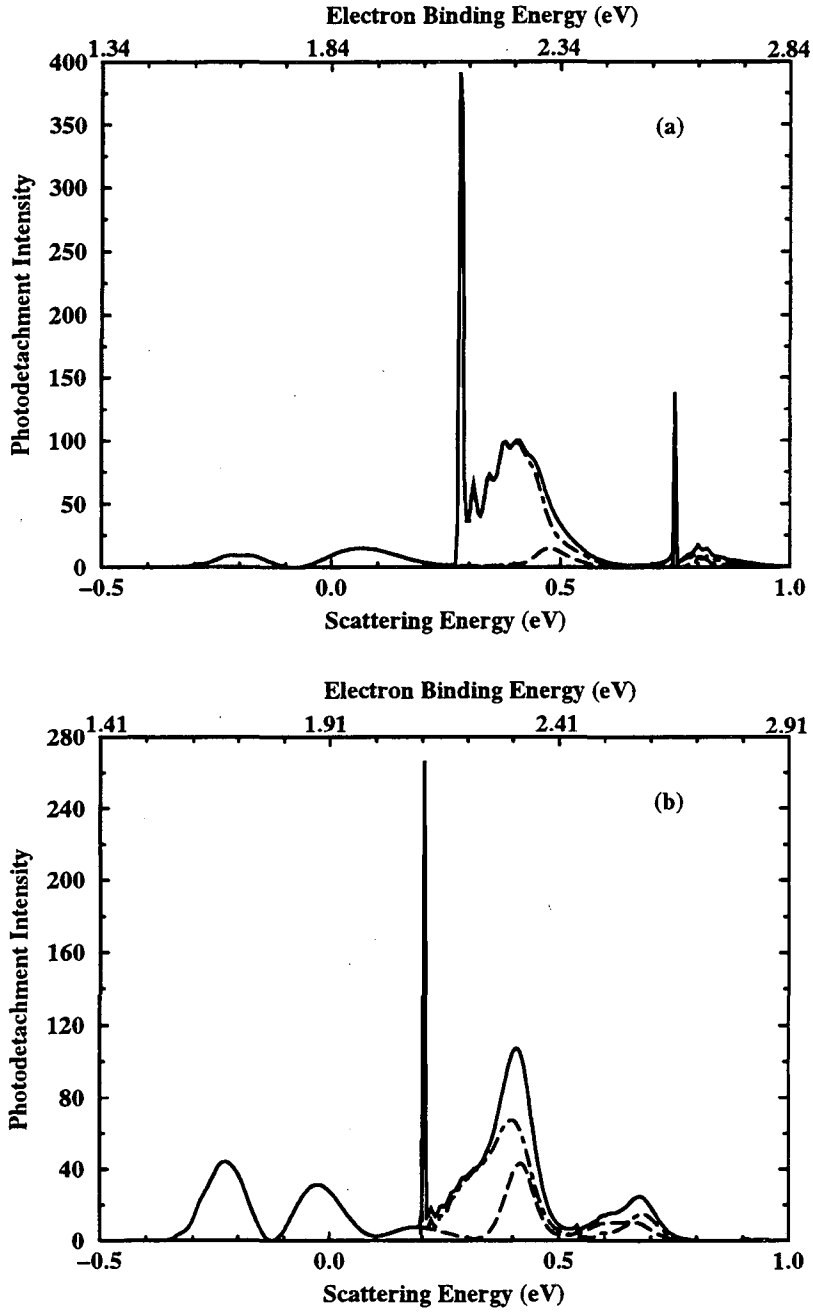

Figure 3.8: Two degree of freedom photodetachment intensities from the $\nu = 2$ state of the anion for (a) H_3O^- and (b) D_3O^-. The solid line is the total intensity, the dashed line is the product-selected intensity, and the dot-dashed line is the reactant-selected intensity.

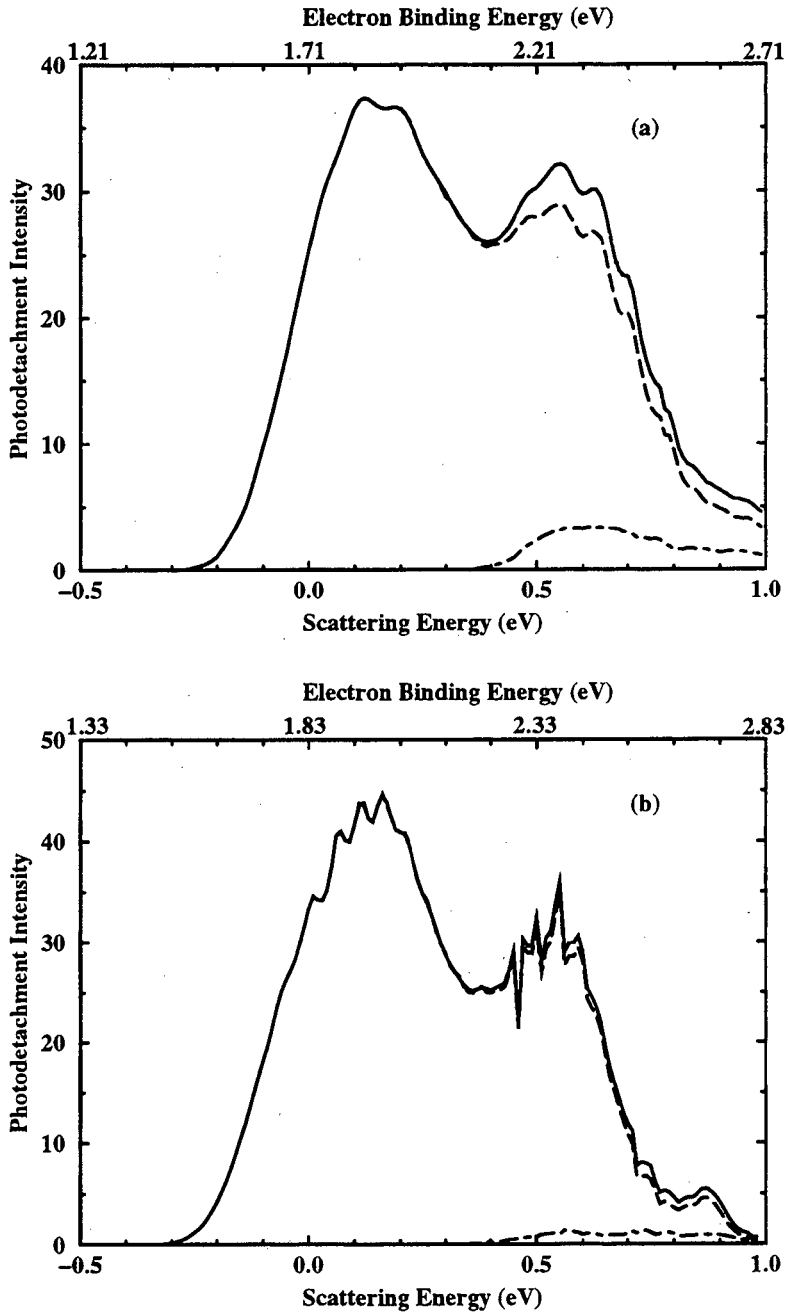

Figure 3.9: Four degree of freedom photodetachment intensities from the $\nu = 0$ state of the anion for (a) H_3O^- and (b) D_3O^-. The anion equilibrium bending angles are $\gamma_1^0 = 175.9°$ and $\gamma_2^0 = 104.8°$. The solid line is the total intensity, the dashed line is the product-selected intensity, and the dot-dashed line is the reactant-selected intensity.

single broad feature. In the deuterated spectrum all three peaks are observed with (000) → (001) peak spacings of 0.39 and 0.32 eV, respectively. These peak spacings are larger than those found in the 2D calculations. As in the case of H_3O^- the peaks are broadened with superimposed structure not seen in the 2D spectrum. The relative intensity of the (001) peak to the (000) peak is larger than that seen in the 2D results. Only a small fraction of the intensity leads to the formation of the reactants.

In Figure 3.10 we show the $\nu = 0$ spectrum with equilibrium angles $\gamma_1^0 = 169.0^o$ and $\gamma_2^0 = 122.0^o$ for (a) H_3O^- and (b) D_3O^-. These angles correspond to the transition state geometry of the neutral. The three peaks are observed as in the 2D spectra with (000) → (001) and (001) → (002) peak spacings of 0.45 and 0.33 eV for H_3O^- and 0.34 and 0.29 eV for D_3O^-, in excellent agreement with experiment. The peak spacings are somewhat different than those in the 2D spectra and the 4D spectra in Fig. 3.9 indicating that they are sensitive to the constraint to two degrees of freedom and the choice of anion equilibrium angles. The bending progression and broadened peaks seen in the spectra of Fig. 3.9 have disappeared but there is some asymmetry in the (001) peak in Fig. 3.10(a) which may be attributed to OH bending excitation. Asymmetry is not easily discerned in the other peaks and there is not the same degree of asymmetry as observed in the experiment. In these spectra the relative intensity of the (001) peak to the (000) peak is significantly reduced from the 2D spectra and the 4D spectra of Fig. 3.9. A small amount of reactants is formed in the H_3O^- case while no reactants are seen for D_3O^-. Again a dip at the energy of $H_2(v = 1)$ is observed.

The anion equilibrium angles were chosen to give greater Franck-Condon overlap with the neutral equilibrium geometries. The resulting decrease in bending excitation of the neutral gives better agreement with the observed experimental spectra. This indicates that these angles may be more similar in the neutral and anion than is given by the current potential energy surfaces. Comparison of Figs. 3.9 and 3.10 indicates that the relative intensities of the peaks are also affected by a change in the equilibrium angles. If the equilibrium angles for the anion are not near those for the neutral, then the region of Franck-Condon overlap sits higher up on the repulsive wall of the neutral potential where the excited vibrational states have greater

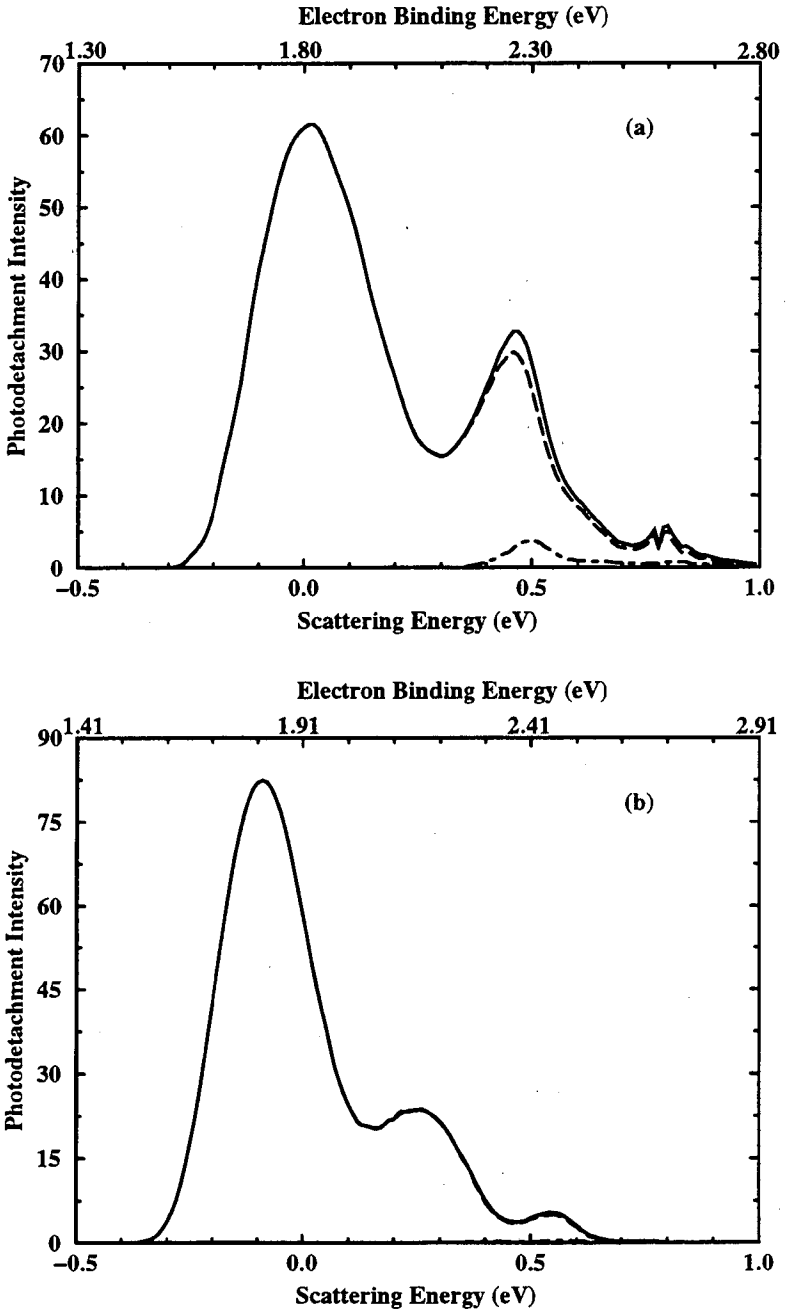

Figure 3.10: Four degree of freedom photodetachment intensities from the $\nu = 0$ state of the anion for (a) H_3O^- and (b) D_3O^-. The anion equilibrium bending angles are $\gamma_1^0 = 169°$ and $\gamma_2^0 = 122°$. The solid line is the total intensity, the dashed line is the product-selected intensity, and the dot-dashed line is the reactant-selected intensity.

amplitude.

The spectral features appear at lower electron binding energies than in the 2D calculations. The (000) peak occurs at 1.80 and 1.82 eV eBE for H_3O^- and D_3O^-, respectively. This is 0.27 and 0.29 eV higher than seen in the experiment. (We should note that this effect is seen in Fig. 3.9(a) as well with the first peak at 1.83 eV eBE.) A difference between the neutral and anion zero point energies in the bending degrees of freedom leads to these lower electron binding energies than seen in the 2D case.

Figure 3.11 shows the $\nu = 2$ spectrum for (a) H_3O^- and (b) D_3O^- with the anion equilibrium angles $\gamma_1^0 = 175.9^o$ and $\gamma_2^0 = 104.8^o$. The same basic structure is seen as in Fig. 3.8: a narrow peak followed by a very broad feature. There are however, large differences between these spectra and the 2D results. The narrow peak is much less dominant and in the deuterated spectrum is not identifiable as a separate feature. The broad peak has a bending progression superimposed on it. As in the 2D case, the majority of the intensity leads to the formation of reactants. This anion state has the majority of its Franck-Condon overlap with the $OH + H_2$ side of the neutral surface leading to these reactant-dominated features. There is still some Franck-Condon overlap on the product side of the neutral surface which is seen as a small background in the spectrum. We note that the broad feature is centered at an electron binding energy of about 2.09 eV for H_3O^- and 2.17 eV for D_3O^-. These values are 0.04 and 0.12 eV higher than observed in the experiment.

As discussed by deBeer *et al.*,[15] the differences in electron binding energies may in part be attributed to the difference between the calculated value of the dissociation energy of $H^- \cdots H_2O$ to give $H_2O + H^-$ (0.79 eV) and the experimentally measured value (0.62 ± 0.04 eV). This would put the (000) peak in the $\nu = 0$ spectra as 0.10 eV higher than observed in the experiment. The broad peak in the $\nu = 2$ spectrum would be 0.13 eV *lower* than is seen in the experiment. [We note that the calculated spectra have larger peak widths than those in the experiment. Thus the electron binding energies of the onsets of the spectra are closer to the experiment than the peak positions.] deBeer *et al.* have suggested that the barrier is too "late" in the WDSE surface, and should be moved earlier into the $OH + H_2$ valley. Our results

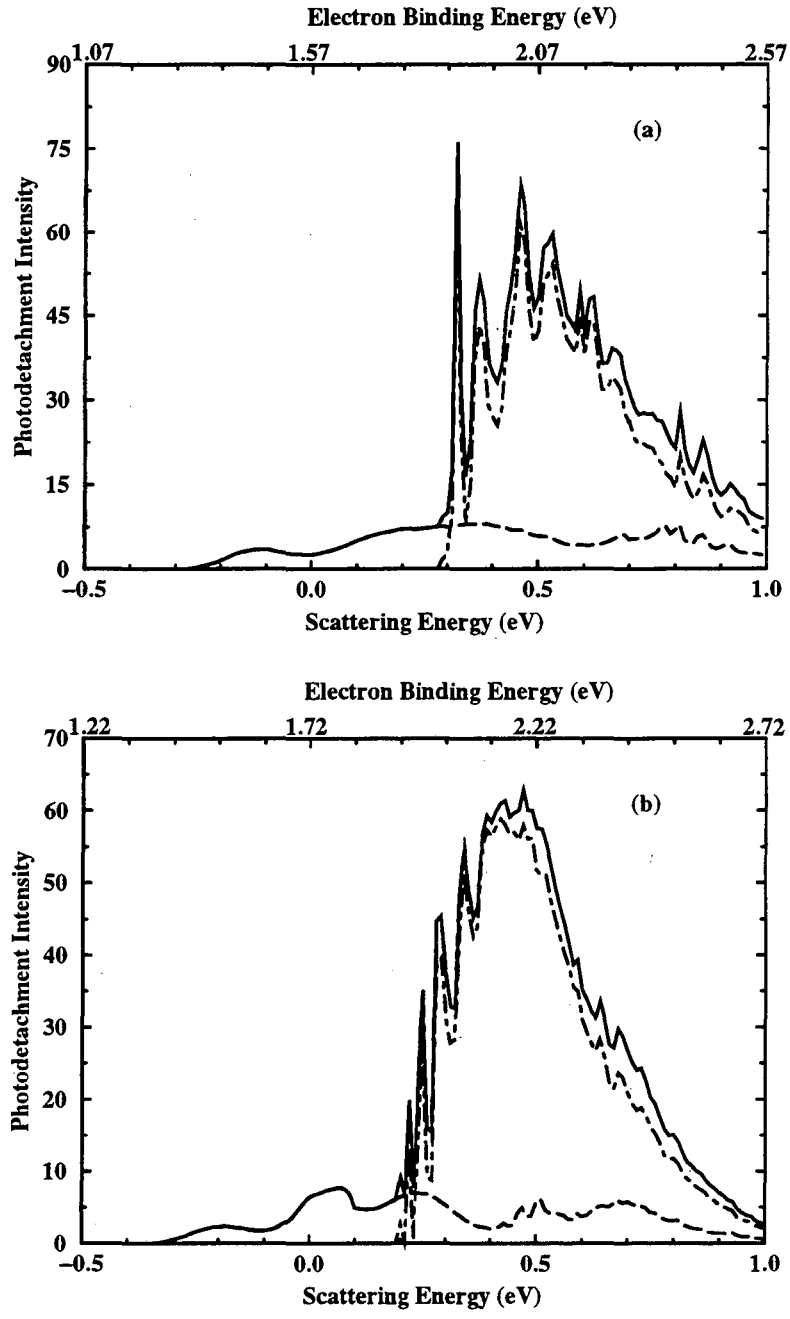

Figure 3.11: Four degree of freedom photodetachment intensities from the $\nu = 2$ state of the anion for (a) H_3O^- and (b) D_3O^-. The anion equilibrium bending angles are $\gamma_1^0 = 175.9°$ and $\gamma_2^0 = 104.8°$. The solid line is the total intensity, the dashed line is the product-selected intensity, and the dot-dashed line is the reactant-selected intensity.

are consistent with this conclusion. Moving the barrier later would reduce the zero point energy of the $H_2O\cdots H$ neutral thus shifting the peak positions to lower energy in the $\nu = 0$ spectra. It might also increase the zero point energy of the $HO\cdots H_2$ neutral thus shifting the broad peak in the $\nu = 2$ spectrum to higher energies.

3.5 Concluding Remarks

We have shown how the DVR-ABC formalism for generating the Green's function can be used to obtain total and arrangement-selected photodetachment intensities simultaneously. We have presented the results of this method applied to two and (planar) four degree of freedom calculations of the photodetachment spectra of H_3O^- and D_3O^-. In addition a multiply-shifted quasi-minimal residual (MSQMR) method was used to obtain the Green's function for many energies at once, producing a significant savings in computational time.

The H_3O^- anion has two local minima, one of the form $H_2O\cdots H^-$ (the global minimum) which lies under the product side of the neutral surface, and the other of the form $HO^-\cdots H_2$ lying under the reactant side of the neutral surface. As a result the photodetachment spectra are highly sensitive to the initial vibrational state of H_3O^-; the $\nu = 0$ state is localized in the $H_2O\cdots H^-$ well and results primarily in the formation of products while the $\nu = 2$ state is delocalized over both wells and results primarily in the formation of reactants.

We have performed the two degree of freedom calculations to illustrate the basic nature of the spectra and to demonstrate agreement with 2D calculations by de Beer *et al.*[15] Our 2D spectra are in good agreement with those of de Beer *et al.* despite the use of somewhat different coordinates. The four degree of freedom calculations represent our best prediction of the experimental spectra. That is, if the potential energy surfaces we used were the "true" ones, we would expect the 4D spectra to be in excellent agreement with the experiment. Since the spectra are not in excellent agreement, we can analyze the differences to obtain information about the "true" potential energy surfaces.

The $\nu = 0$ spectrum consists of three peaks which are assigned to the local

mode OH stretch in the neutral H_2O of the products.[15] In the case where the anion equilibrium bending angles for OH and H_2 are given the values obtained from *ab initio* results by de Beer *et al.* the four degree of freedom spectra in Fig. 3.9 spectra have the same basic structure but have different peak spacings and broader peak widths than the two degree of freedom results. In addition significant bending excitation of the neutral is observed. Changing the angles to that of the transition state geometry of the neutral eliminates most of the bending excitation and lowers the intensity of the (001) peak relative to the (000) peak giving a spectrum in good agreement with experiment. Since neither the neutral nor anion potential are accurately known, it is not possible to state whether it is the anion or the neutral bending potentials which are in error. The conclusion that can be drawn is that the angles are more similar in the two potentials than given by the current surfaces.

The $\nu = 2$ spectrum is dominated by a broad peak leading to the formation of reactants. The large narrow peak which was observed in the two degree of freedom calculations, is much less dominant in the four degree of freedom spectra. The four degree of freedom spectra also have a bending progression superimposed on the broad peak which is not observed in the two degree of freedom results. The calculated intensities are in good agreement with the experimental spectra assigned to the $HO^- \cdots H_2$ anion minimum. The theoretical spectrum does have a small background leading to products due to the delocalized nature of the $\nu = 2$ eigenstate across both anion minima.

Finally, the theoretical calculations give the electron binding energy of the $\nu = 0$ spectra as too high relative to the experimental results. While for the for the $\nu = 2$ spectra, the electron binding energy is too low compared to experiment. This disagreement between the theoretical and experimental results is consistent with the suggestion by de Beer *et al.*[15] that the barrier on the neutral WDSE potential energy surface is too "late" and should be moved earlier into the $OH + H_2$ valley.

Chapter 4

Thermal Rate Constants

4.1 Introduction

The last decade has seen great progress in theoretical methods for treating chemical reaction dynamics. Full quantum scattering calculations are now routinely carried out for numerous three atom systems (atom-diatom collisions). Indeed, full-dimensionality scattering calculations have been carried out for some four atom systems[88,89,134–140] (most notably the OH + H_2 reaction). However, such large systems still present a major challenge and methods are needed to make reactions involving many atoms (> 3) more amenable to theoretical calculations. To this end, this work has focused on *directly* calculating the dynamical quantity of interest. While the S-matrix elements ($S_{n_p,n_r}(E)$) provide the most detailed information obtainable for a chemical reaction (resolution on the full state-to-state and amplitude level), frequently one is not interested in this extreme amount of detail. As discussed in Chapter 2, often more averaged quantities , such as the initial state-selected reaction probability,

$$P_{n_r}(E) = \sum_{n_p} |S_{n_p,n_r}(E)|^2, \tag{4.1}$$

or the cumulative reaction probability,

$$N(E) = \sum_{n_p,n_r} |S_{n_p,n_r}(E)|^2, \tag{4.2}$$

are desired. In many cases, it is the "velocity" of the reaction at constant *temperature* that is of interest, the thermal rate constant,

$$k(T) = \frac{1}{2\pi\hbar Q_r(T)} \int_0^\infty e^{-\beta E} \sum_{n_p,n_r} |S_{n_p,n_r}(E)|^2 \, dE, \tag{4.3}$$

where $Q_r(T)$ is the reactant partition function and $\beta = 1/k_b T$. The recent progress achieved in the direct calculation of initial state-selected[11,96,141] is discussed in Chapter 2. Methods for directly obtaining the thermal rate constant have existed for over 35 years[142] and have been the focus of much attention[47,58,91,143–168] for the last two decades. This chapter describes some of the latest advances in the technology for the direct (but fully correct) calculation of the thermal rate constant for a chemical reaction.

The exact thermal rate constant for a system obeying classical mechanics is given by

$$k_{CL}(T) = \frac{1}{Q_r(T)h^F} \int d\mathbf{p} \int d\mathbf{q} \, e^{-\beta H(\mathbf{p},\mathbf{q})} \, \delta[f(\mathbf{q})] \frac{df(\mathbf{q})}{d\mathbf{q}} \cdot \frac{\mathbf{p}}{m} \, \chi(\mathbf{p},\mathbf{q}), \tag{4.4}$$

where $\mathbf{p}$ and $\mathbf{q}$ are the momenta and coordinates of the classical system of F degrees of freedom governed by the Hamiltonian $\mathrm{H}(\mathbf{p},\mathbf{q})$. The equation $f(\mathbf{q}) = 0$ defines a dividing surface which separates reactants and products. $\chi(\mathbf{p},\mathbf{q})$ is known as the *characteristic function* and is equal to 1 for reactive trajectories and 0 for nonreactive trajectories. Practically, one runs a trajectory with initial conditions $\mathbf{p}$ and $\mathbf{q}$ (which must lie on the dividing surface by virtue of the $\delta[f(\mathbf{q})]$ factor) backward in time to determine if it started as reactants in the infinite past; starting with the same initial conditions the trajectory is run forward in time to determine if it ends up as products in the infinite future. (Here "infinite" refers to times long enough to ensure the trajectory will not return to the interaction region.) A trajectory which positively satisfies these two criteria is reactive. This is the point of departure for various dynamical approximations, most notably transition state theory[169–174] (TST). In TST the characteristic function is assumed to be given by $\chi(\mathbf{p},\mathbf{q}) = h(p_s)$ where $h(x)$ is the Heaviside step function equal to 1 if $x > 0$ and 0 if $x < 0$, and p_s is the momentum perpendicular to the dividing surface $f(\mathbf{q}) = 0$. Thus, trajectories crossing the dividing surface are assumed never to come back — there is *no recrossing*

of the dividing surface.[170] Thus, TST provides an upper bound to the classical rate constant and a variational principle exists in which the best dividing surface is that which gives the lowest rate (*i.e.*, the fewest recrossing trajectories).

Transition state theory is the most used and useful model in chemical reaction rate theory. However, strictly speaking there is no (single) quantum mechanical transition state theory in the sense that the fundamental TST assumption is stated in terms of (recrossing) trajectories; this cannot be straightforwardly interpreted in the context of quantum mechanics. In addition, a strict, meaningful upper bound to the exact quantum rate constant has never been provided by any quantum mechanical version. There are, however, many quantum mechanical *analogues* to (or generalizations of) transition state theory (providing both exact and approximate rates). All these approaches invoke, in some way, the spirit of TST: reactivity is determined at the transition state (or in the case of quantum mechanics and the uncertainty principle, in a small area around the transition state).

In this Chapter quantum mechanical methods for obtaining rate constants are presented which are evocative of this spirit. However, the goal here is to obtain the exact rate constant and therefore the current approach is more akin to the method described above for calculating exact classical rate constants. That is, if one is interested in obtaining the exact classical rate, a straightfoward approach would be to start trajectories with initial conditions as reactants and run them forward in time to see if they react. With the wisdom of TST in hand, we would follow the procedure described above and trajectories would only have to be followed for short(er) times (in practice) forward and backward. In addition, trajectories which never reach the transition state, and are thus destined not to react, would not be followed at all. Similarly, if the quantum mechanical rate constant is desired, it can be obtained by calculating all the reactive S-matrix elements and then averaging away all that detail as indicated in Eq. (4.3). However, the lesson of TST would tell us that a simpler, direct route to the rate constant would be to somehow measure the net reactive flux through the transition state.

4.2 Direct Calculation of Rates

4.2.1 Flux Correlation Functions

Though Yamamoto was the first to derive a direct expression for the thermal rate constant,[142] the present approach is best described from the point of view of later work by Miller.[143] For completeness, we summarize here the relevant points of Miller's derivation.

As given in Eq. (4.3), the thermal rate constant can be expressed in terms of the state-to-state S-matrix elements as

$$k(T) = \frac{1}{2\pi\hbar Q_r(T)} \sum_{n_p,n_r} \int_0^\infty dE\ e^{-\beta E} |S_{n_p,n_r}(E)|^2, \tag{4.5}$$

where Q_r is the reactant partition function

$$Q_r(T) = \left(\frac{2\pi\mu k_b T}{h^2}\right)^{3/2} \sum_{n_r} g_{n_r}\, e^{-\beta\epsilon_{n_r}}. \tag{4.6}$$

Here, μ is the reduced mass for the relative translation of the reactants, the ϵ_{n_r} are the energy levels of the reactant internal degrees of freedom, and g_{n_r} is the degeneracy of reactant state n_r. Starting with this expression Miller showed[143] that the rate constant can be expressed as

$$k(T) = \frac{1}{2\pi\hbar Q_r(T)} \sum_{n_r} \int_{-\infty}^0 dP\ \langle \Psi_{P,n_r} | \hat{F} e^{-\beta\hat{H}} | \Psi_{P,n_r} \rangle, \tag{4.7}$$

where Ψ_{P,n_r} is the full scattering wavefunction corresponding to an initial incoming wave in the reactant channel n_r with translational momentum P. $\hat{F}$ is the symmetrized flux operator for any dividing surface separating reactants and products. This expression for the rate constant is much more appealing than Eq. (4.5) from an intuitive standpoint. It states that the rate is given by the Boltzmann average of the contributions from each of the asymptotic reactant states. The contribution of a given state is just the expectation value of the flux through some (any) surface dividing the reactants and products.

Note that in Eq. (4.7) the integral over initial momenta includes only negative values. Clearly this must be true as a positive relative momentum would move

the reactants further apart instead of towards a (possibly reactive) collision. However, this is important in that the completeness relation,

$$\frac{1}{2\pi\hbar}\sum_{n_r}\int_{-\infty}^{\infty} dP\,|\Psi_{P,n_r}\rangle\langle\Psi_{P,n_r}| = 1, \tag{4.8}$$

requires integration over all momenta from $-\infty$ to $+\infty$. Therefore the trace of an operator $\hat{A}$ is given by

$$\mathrm{tr}[\hat{A}] = \frac{1}{2\pi\hbar}\sum_{n_r}\int_{-\infty}^{\infty} dP\,\langle\Psi_{P,n_r}|\hat{A}|\Psi_{P,n_r}\rangle. \tag{4.9}$$

This can be used to express the rate constant in terms of a quantum mechanical trace if we first define a projection operator $\hat{\wp}$ which projects onto only those scattering states with negative asymptotic momenta. That is, $\hat{\wp}$ is defined to have the property

$$\mathrm{tr}[\hat{A}] = \frac{1}{2\pi\hbar}\sum_{n_r}\int_{-\infty}^{\infty} dP\,\langle\Psi_{P,n_r}|\hat{A}\hat{\wp}|\Psi_{P,n_r}\rangle, \tag{4.10}$$

$$= \frac{1}{2\pi\hbar}\sum_{n_r}\int_{-\infty}^{0} dP\,\langle\Psi_{P,n_r}|\hat{A}|\Psi_{P,n_r}\rangle. \tag{4.11}$$

Then, Eq. (4.7) for the rate constant can be rewritten simply as a quantum mechanical trace

$$k(T) = \frac{1}{Q_r}\mathrm{tr}[e^{-\beta\hat{H}}\hat{F}\hat{\wp}], \tag{4.12}$$

using this projection operator. This is a central result in the derivation of a useful expression for the thermal rate constant which does not depend on state-selected (or energy-dependent) quantities.

Some discussion must now be devoted to the nature of the projection operator. Recall that in the expression for the exact classical rate constant given in Eq. (4.4), $\chi(\mathbf{p},\mathbf{q})$ is the most crucial factor as it contains the dynamical information of the system. The operator $\hat{\wp}$ plays the same role in the quantum mechanical expression as does $\chi(\mathbf{p},\mathbf{q})$ in the classical one. Whereas $\chi(\mathbf{p},\mathbf{q})$ projects onto the reactive part of the phase space, $\hat{\wp}$ projects onto the reactive part of the Hilbert space.

Such a projection operator can be written down in multiple forms. The simplest, which immediately arises from the above derivation, is obtained by projecting onto only those scattering eigenstates which can produce reaction:

$$\hat{\wp} = \frac{1}{2\pi\hbar}\sum_{n_r}\int_{-\infty}^{0} dP\,|\Psi_{P,n_r}\rangle\langle\Psi_{P,n_r}|. \tag{4.13}$$

Using this form for the projection operator in Eq. (4.12) and evaluating the trace in the basis $\{|\Psi_{P,n_r}\rangle\}$ it is easily seen that Eq. (4.7) for the rate constant is recovered.

An alternative, but formally equivalent, expression for the projection operator, originally proposed by Miller,[143] is given by

$$\hat{\wp} = \lim_{t\to-\infty} e^{i\hat{H}t/\hbar} h(\hat{P}_r) e^{-i\hat{H}t/\hbar}, \tag{4.14}$$

where h is the Heaviside step function, $h(\xi) = 1$ for $\xi > 0$ and $h(\xi) = 0$ otherwise. Here, the momentum $\hat{P}_r$ is the translational momentum of the reactants. This operator selects out those components of the basis which have momentum in the direction towards products in the infinite past (at $t \to -\infty$). The relation to Eq. (4.13) can be easily identified. It is not difficult to see that a very similar projection operator can be defined as

$$\hat{\wp} = \lim_{t\to\infty} e^{i\hat{H}t/\hbar} h(\hat{P}_p) e^{-i\hat{H}t/\hbar}, \tag{4.15}$$

where $\hat{P}_p$ is the translational momentum of the products. This can be viewed as projecting onto the components of the basis which have positive momentum in the infinite future.

Miller, Schwartz, and Tromp[58] have shown that these projection operators are equivalent to one based on the position step function:

$$\hat{\wp} = \lim_{t\to-\infty} e^{i\hat{H}t/\hbar} h(-\hat{s}) e^{-i\hat{H}t/\hbar}, \tag{4.16}$$

in the long time limit indicated. For simplicity of notation we will often refer to a generic reaction coordinate s, satisfying $s = f(\mathbf{q}) = 0$, with negative s lying on the reactant side of the dividing surface. This latter projection operator selects out those components of the basis which were on the reactant side of the barrier at $t \to -\infty$. Again, another projection operator can be defined within this spirit as

$$\hat{\wp} = \lim_{t\to\infty} e^{i\hat{H}t/\hbar} h(\hat{s}) e^{-i\hat{H}t/\hbar}, \tag{4.17}$$

which projects onto that part of the basis which is on the product side of the dividing surface in the infinite future.

Using the projection operators in Eqs. (4.14) and (4.16), and the property $[\hat{H}, \hat{\varphi}] = 0$,[143] the exact thermal rate constant can be expressed as

$$k(T) = \frac{1}{Q_r} \lim_{t\to\infty} \mathrm{tr}[h(\hat{p}) e^{i\hat{H}t_c^*/\hbar} \hat{F} e^{-i\hat{H}t_c/\hbar} h(\hat{p})], \tag{4.18}$$

or equivalently as

$$k(T) = \frac{1}{Q_r} \lim_{t\to\infty} \mathrm{tr}[h(-\hat{s}) e^{i\hat{H}t_c^*/\hbar} \hat{F} e^{-i\hat{H}t_c/\hbar} h(-\hat{s})], \tag{4.19}$$

where we have combined the propagators with the Boltzmann operator to obtain a single propagator in complex time, $t_c = t - i\beta\hbar/2$, and also used the property of the step function $h(\xi) * h(\xi) = h(\xi)$ in order to express $k(T)$ as the trace of an Hermitian operator. From these expressions we define the flux-momentum correlation function,

$$C_{fp}(t) = \mathrm{tr}[h(\hat{p}) e^{i\hat{H}t_c^*/\hbar} \hat{F} e^{-i\hat{H}t_c/\hbar} h(\hat{p})], \tag{4.20}$$

and the flux-position (sometimes called the flux-step or flux-side) correlation function,

$$C_{fs}(t) = \mathrm{tr}[h(-\hat{s}) e^{i\hat{H}t_c^*/\hbar} \hat{F} e^{-i\hat{H}t_c/\hbar} h(-\hat{s})], \tag{4.21}$$

so that the thermal rate constant is given by

$$k(T) = \frac{1}{Q_r} \lim_{t\to\infty} C_{fp}(t) = \frac{1}{Q_r} \lim_{t\to\infty} C_{fs}(t). \tag{4.22}$$

An important feature of this approach is that these correlation functions only need to be evaluated at a single (long) time to obtain the rate constant. (Here "long" refers to the time needed for amplitude to cross the barrier which, as will be seen in the applications can be quite short, *sim* 5-70 fs.)

If we note that the flux operator can be written as

$$\hat{F} = \frac{i}{\hbar} [\hat{H}, h(\hat{s})], \tag{4.23}$$

and thus,

$$e^{i\hat{H}t/\hbar} \hat{F} e^{-i\hat{H}t/\hbar} = \frac{d}{dt} \left\{ e^{i\hat{H}t/\hbar} h(\hat{s}) e^{-i\hat{H}t/\hbar} \right\}, \tag{4.24}$$

then from the flux-position correlation function we can define a left-right (sometimes called the step-step) correlation function

$$C_{ss}(t) = \mathrm{tr}[h(-\hat{s}) e^{i\hat{H}t_c^*/\hbar} h(\hat{s}) e^{-i\hat{H}t_c/\hbar} h(-\hat{s})]. \tag{4.25}$$

by replacing the time-evolved flux operator with this expression and pulling the derivative outside the trace. Then the rate constant is obtained as the long time limit of the derivative of the left-right correlation function.

$$k(T) = \frac{1}{Q_r} \lim_{t\to\infty} \frac{d}{dt} C_{ss}(t). \tag{4.26}$$

Note that this requires obtaining the correlation function at two or more (long) times in order to evaluate the derivative.

If the flux-position correlation function is written with the projection operator in Eq. (4.17) (with some rearrangement),

$$\tilde{C}_{fs}(t) = \mathrm{tr}[e^{-\beta\hat{H}/2}\hat{F}e^{-\beta\hat{H}/2}\, e^{i\hat{H}t/\hbar}h(\hat{s})e^{-i\hat{H}t/\hbar}], \tag{4.27}$$

then we can use Eq. (4.24) to define the flux-flux correlation function

$$C_{ff}(t) = \mathrm{tr}[e^{-\beta\hat{H}/2}\hat{F}e^{-\beta\hat{H}/2}\, e^{i\hat{H}t/\hbar}\hat{F}e^{-i\hat{H}t/\hbar}], \tag{4.28}$$

as its time derivative. The rate constant is then given by the time integral of the derivative so that

$$k(T) = \frac{1}{Q_r} \int_0^\infty C_{ff}(t)\, dt. \tag{4.29}$$

The flux-flux correlation function must be evaluated at many times in order to compute the required time integral.

4.2.2 Evaluation of the Trace

The efficient calculation of the thermal rate constant for a chemical reaction using any of the correlation functions just described lies in the evaluation of the quantum mechanical trace. In this work we concentrate on obtaining the rate via the flux-position and flux-flux correlation functions. In the following, we first describe how the flux-flux correlation function can be obtained by taking advantage of the physics involved in the chemical reaction. Then the same principle is applied to the flux-position correlation function with a few changes.

The Flux-Flux Correlation Function

The evaluation of the quantum mechanical trace to obtain $C_{ff}(t)$ is the computational bottleneck. This is because to obtain a matrix element of the operator inside the trace, propagation must be carried out in both real time and imaginary time (the Boltzmann operator). However, the trace can be calculated efficiently by evaluating it in an optimum basis (since the trace is independent of the basis in which it is computed). In the case of the flux-flux correlation function the operator inside the trace is of low rank. It has previously been shown that if the flux operator in one-dimension is diagonalized in a finite basis, there will be only two nonzero eigenvalues.[158,159,175] These two eigenvalues are of equal magnitude but opposite sign, corresponding to motion forward and backward across the dividing surface. In a multidimensional case the flux operator is *not* of low rank as this pair of positive and negative eigenvalues will be repeated for every state in the perpendicular degrees of freedom (the degrees of freedom that are parallel to the dividing surface). However, the Boltzmannized flux operator

$$\hat{F}(\beta) = e^{-\beta\hat{H}/2}\,\hat{F}\,e^{-\beta\hat{H}/2}, \tag{4.30}$$

is of low rank in many dimensions. This is because the Boltzmann factor restricts the number of states accessible in the perpendicular degrees of freedom (though this number naturally rises with temperature). Thus, the rank of this operator will be approximately equal to twice the number of states in the perpendicular degrees of freedom that are significantly populated thermally at temperature T. If the dividing surface is placed at the saddle point then this can be thought of as twice the number of states of the "activated complex." To see this, suppose for illustrative purposes that the reaction coordinate (the one degree of freedom for motion normal to the dividing surface) were separable from all the degrees of freedom for motion on the dividing surface (the activated complex); $\hat{F}(\beta)$ would then be given by

$$\hat{F}_{sep}(\beta) = \hat{F}_{1d}\,e^{-\beta\hat{H}^{\ddagger}} = \hat{F}_{1d}\sum_{n^{\ddagger}} |n^{\ddagger}\rangle\langle n^{\ddagger}|e^{-\beta E_{n^{\ddagger}}}, \tag{4.31}$$

where $\hat{F}_{1d}$ is the one dimensional flux operator (of rank 2)[175] and $\hat{H}^{\ddagger}$ the Hamiltonian for the activated complex, with eigenfunctions $|n^{\ddagger}\rangle$ and eigenvalues $E_{n^{\ddagger}}$. The effective

rank of $\hat{F}_{sep}(\beta)$ is thus twice the number of states, $|n^{\ddagger}\rangle$ for which $e^{-\beta E_{n^{\ddagger}}}$ is significant. One expects the rank of the true Boltzmannized flux operator to be similar. We note that a slightly different version of the Boltzmannized flux operator was first defined by Park and Light.[159]

If we could somehow obtain the eigenvaules $\{f_n\}$ and eigenfunctions $\{|n\rangle\}$ of the Boltzmannized flux operator,

$$\hat{F}(\beta)|n\rangle = e^{-\beta\hat{H}/2}\,\hat{F}\,e^{-\beta\hat{H}/2}|n\rangle = f_n|n\rangle, \tag{4.32}$$

this would constitute the ideal basis in which to evaluate the trace in Eq. (4.28). In fact, there is a method which can do just that: the iterative Lanczos algorithm[133] obtains only the largest (in absolute value) eigenvalues (and the corresponding eigenfunctions) of an operator. The procedure is to first choose a random vector $|v_0\rangle$. (We continue to use bra-ket notation, though this procedure is carried out within a finite basis set. In a such a representation, the states become vectors and operators become matrices.) A Krylov basis is formed by repeated application of $\hat{F}(\beta)$ onto $|v_0\rangle$:

$$\begin{aligned} |v_1\rangle &= \hat{F}(\beta)\,|v_0\rangle + S.O. \\ |v_2\rangle &= \hat{F}(\beta)\,|v_1\rangle + S.O. \qquad (4.33) \\ &\vdots \\ |v_{M-1}\rangle &= \hat{F}(\beta)\,|v_{M-2}\rangle + S.O. \qquad (4.34) \end{aligned}$$

where $S.O.$ implies Schmidt orthogonalization to all previous vectors. In this process the matrix of $\hat{F}(\beta)$ in the Krylov basis $\{|v_0\rangle, |v_1\rangle, \ldots, |v_{M-1}\rangle\}$ is automatically obtained. Diagonalizing this Krylov space version gives the M largest (in absolute value) eigenvalues $\{f_n\}_{n=1}^{M}$ and eigenvectors $\{|n\rangle\}_{n=1}^{M}$ of $\hat{F}(\beta)$ in the full basis.

Once these eigenvalues and eigenvectors are in hand, the rate constant is given by

$$k(T) = Q_r(T)^{-1} \sum_{n=1}^{M} f_n \int_0^{\infty} \langle n|\, e^{i\hat{H}t/\hbar}\,\hat{F}\,e^{-i\hat{H}t/\hbar}\,|n\rangle\, dt. \tag{4.35}$$

Thus the cost of calculating the rate constant is propagation in imaginary time (applying $\hat{F}(\beta)$) M-1 times, where M is the rank of $\hat{F}(\beta)$, plus propagation in real time of the resulting M eigenfunctions. Note that in general M is much, much smaller than

the total size of the basis since it is roughly equal to twice the number of thermally accessible states of the activated complex. In carrying out the real time propagation, it is advantageous to introduce an imaginary absorbing potential:[41–46,48–55]

$$\hat{H} \rightarrow \hat{H} - i\hat{\epsilon}, \tag{4.36}$$

where $\hat{\epsilon} = \epsilon(\mathbf{q})$ is zero in the interaction region and "turns on" in the reactant and product valleys. By including ϵ the outgoing flux is absorbed before it can undergo unphysical reflection from the edge of the finite basis set. The absorbing potential actually has two desirable consequences: (1) Its inclusion guarantees that the flux-flux correlation function will go to zero at long times. And, (2) it allows the edge of the finite basis to be moved in closer to the interaction region in the reactant and product valleys, thus reducing the size of the basis. Absorbing potentials have previously been used by Brown and Light[47] in calculating the flux-flux autocorrelation function.

The rate constant now becomes

$$k(T) = Q_r(T)^{-1} \sum_{n=1}^{M} f_n \int_0^\infty dt \, \langle n | \, e^{i(\hat{H}+i\hat{\epsilon})t/\hbar} \, \hat{F} \, e^{-i(\hat{H}-i\hat{\epsilon})t/\hbar} \, | n \rangle. \tag{4.37}$$

Since the rate constant is given by the time integral of the flux-flux correlation function, the time propagator in Eq. (4.37) should be carried out with a method which gives the result at all intermediate times for the same effort as propagating to one long time. The split operator propagation scheme satisfies this requirement. For a small time, Δt, the propagator is approximated as

$$e^{-i(\hat{H}-i\hat{\epsilon})\Delta t/\hbar} \simeq e^{-i\hat{T}\Delta t/2\hbar} \, e^{-i(\hat{V}-i\hat{\epsilon})\Delta t/\hbar} \, e^{-i\hat{T}\Delta t/2\hbar}. \tag{4.38}$$

(See Section 4.3.3 for the precise form of the split operator propagator used in the present applications.) Thus, an eigenstate $|n\rangle$ is propagated in steps of Δt by successive application of this split operator:

$$|n(t+\Delta t)\rangle = e^{-i\hat{T}\Delta t/2\hbar} \, e^{-i(\hat{V}-i\hat{\epsilon})\Delta t/\hbar} \, e^{-i\hat{T}\Delta t/2\hbar} \, |n(t)\rangle. \tag{4.39}$$

Note that the $\langle n(t)|$ is given by the complex conjugate of $|n(t)\rangle$ so it is only necessary to propagate the ket state. The correlation function is thereby obtained at all the

intermediate times (needed to perform the integral) for the same cost as finding it at the largest time. (The same propagation scheme is used in imaginary time for the Boltzmann operator.) Each eigenstate of the Boltzmannized flux operator is propagated and its contribution to the flux-flux correlation function, and hence the rate, is obtained. Writing out the expression for the rate constant explicitly with some integration scheme for the time integral gives

$$k(T) = Q_r(T)^{-1} \sum_{n=1}^{M} f_n \sum_{\ell=0} w_\ell \langle n(\ell\Delta t)| \hat{F} |n(\ell\Delta t)\rangle, \tag{4.40}$$

where the w_ℓ are the weights in the time integration scheme.

The Flux-Position Correlation Function

In applying this same Lanczos method for evaluating the trace in the case of the flux-position correlation function, some differences arise. First, absorbing potentials cannot be used in the time propagation with the flux-position correlation function. If they are included, the correlation function will tend to zero at long times. Since the rate is equal the correlation function at long times (within a factor of the reactant partition function), the absorbing potentials cannot solve the problem of unphysical reflection from the edge of the finite basis in this case. Second, the correlation function is only needed at a single (long) time, making a scheme such as the Chebychev polynomial expansion (which does not yield intermediate times) a useful propagation method for this approach. This is also made feasible by the elimination of the absorbing potential (giving a real Hamiltonian).

The same reasons for which the Boltzmannized flux operator is of low rank imply a similar low rank for the entire operator $\hat{C}_{fs}(t)$,

$$\hat{C}_{fs}(t) = h(-\hat{s}) e^{i\hat{H}t_c^*/\hbar} \hat{F} e^{-i\hat{H}t_c/\hbar} h(-\hat{s}). \tag{4.41}$$

the trace of which is the rate constant (for large enough t). This is more akin to Manthe and Miller's[12] treatment of the microcanonical case, where the CRP $N(E)$ was expressed as the trace of a matrix/operator of low rank (the eigenvalues of which they called the *eigenreaction probabilities*). The same Lanczos algorithm described

above is used to obtain the eigenvalues and of $\hat{C}_{fs}(t)$ (the eigenfunctions are not needed).

When applying the operator/matrix $\hat{C}_{fs}(t)$ to a vector, each operator in $\hat{C}_{fs}(t)$ operates sequentially (from the right). Thus two operations of the time evolution operator — by far the most time consuming part of the calculation — $exp(-i\hat{H}t_c/\hbar)$ and $exp(i\hat{H}t_c^*/\hbar)$, are required for each operation of $\hat{C}_{fs}(t)$.

The Chebychev polynomial expansion approximates the propagator as[176]

$$e^{-i\mathbf{H}t_c/\hbar} \cong e^{-i\bar{\mathrm{H}}t_c/\hbar} \sum_{n=0}^{N_c} (2-\delta_{n,0})\, i^{-n}\, J_n\left(\frac{\Delta \mathrm{H} t_c}{2\hbar}\right)\, T_n\left(\frac{\mathbf{H}-\bar{\mathrm{H}}}{\Delta \mathrm{H}/2}\right), \tag{4.42}$$

where $\mathbf{H}$ is the Hamiltonian matrix in some finite basis, N_c is the order of the highest Chebychev polynomial, the J_n are Bessel functions, and the T_n are the Chebychev polynomials[177] obtained by the recursion relation

$$T_{n+1}(x) = 2xT_n(x) - T_{n-1}(x). \tag{4.43}$$

ΔH is the spectral range of the Hamiltonian and $\bar{\mathrm{H}}$ is the average value of the Hamiltonian. This scaling of the Hamiltonian is necessary to place the range within (-1,1) for the argument of the Chebychev polynomials. Specifically, if λ_{max} and λ_{min} are the largest and smallest eigenvalues of $\mathbf{H}$, then

$$\Delta \mathrm{H} = \lambda_{max} - \lambda_{min}, \tag{4.44}$$

and

$$\bar{\mathrm{H}} = \frac{\lambda_{max} + \lambda_{min}}{2}. \tag{4.45}$$

In cases where the Hamiltonian can be stored in core memory, we explicitly diagonalize the Hamiltonian to obtain λ_{min} and λ_{max}. When this is not the case (as for the D + H_2 reaction in Section 4.3.3), we estimate λ_{min} and λ_{max} from a low order Lanczos calculation using a sparse Hamiltonian matrix multiply.

The number of Chebychev polynomials needed depends on the spectral range and the propagation time. This relation occurs because the Bessel functions become exponentially damped as the order n becomes larger than the argument. In our case this implies the guideline

$$N_c > \frac{\Delta \mathrm{H}|t_c|}{2\hbar}. \tag{4.46}$$

The Chebychev expansion for the propagator provides several advantages. It is an efficient representation and allows one to combine the operation of the time evolution operator and the Boltzmann operator. Intermediate results and restarting are not required. We are primarily interested in the case of large multidimensional systems where the Hamiltonian matrix cannot be stored directly. The Chebychev propagation only requires the storage of three complex vectors, and one can make use of a sparse matrix multiplication routine for applying the Hamiltonian matrix onto a vector.

4.3 Applications

In order to demonstrate the utility of the direct calculation of thermal rate constants from the flux correlation functions we have applied these methods to several systems. The flux-position correlation function has been used to calculate rates for the one-dimensional Eckart barrier, the two-dimensional collinear H + H_2 reaction, and the three-dimensional D + H_2 reaction for $J = 0$. The flux-flux correlation function approach has been tested on the same D + H_2 system as well as the O + HCl reaction.

4.3.1 The Eckart Barrier

As a starting point, consider the one-dimensional Eckart barrier,

$$V(s) = V_0 \operatorname{sech}^2(s/a), \tag{4.47}$$

with $V_0 = 0.425$ eV, $a = 0.734$ a.u. and a mass of 1061 a.u. These parameters model the collinear H + H_2 reaction. We have chosen to use the $(-\infty, \infty)$ sinc-function discrete variable representation of Colbert and Miller[37] as the finite basis. The basis is specified by N_B and Q_{max}, where N_B is the grid constant used to determine the spacing of the DVR grid points, Δx:

$$\Delta x = \frac{2\pi}{N_B} \left(\frac{2\mu k_b T}{\hbar^2} \right)^{-1/2}. \tag{4.48}$$

For the present applications we have found $N_B = 10 - 14$ to be sufficiently large. Q_{max} defines the extent of the basis; the DVR grid is truncated for $|s| > Q_{max}$.

The flux operator for a dividing surface defined by $f(\mathbf{q}) = 0$ can be expressed as

$$\hat{F} = \frac{1}{2}\{\delta[f(\mathbf{q})]\mathbf{n}_f \cdot \hat{\mathbf{p}} + \hat{\mathbf{p}} \cdot \mathbf{n}_f \delta[f(\mathbf{q})]\}, \tag{4.49}$$

where $\mathbf{n}_f$ is the unit vector normal to the dividing surface and $\hat{\mathbf{p}}$ is the momentum operator. However, this flux operator may be equivalently be written in the form of a commutator:

$$\hat{F} = \frac{i}{\hbar}[\hat{H}, h(f(\mathbf{q}))]. \tag{4.50}$$

We note that these two expressions for the flux operator do not have identical numerical properties in an L^2 basis representation. In particular, for a one-dimensional case it can be proven that the form in Eq. (4.49) is of rank two in a finite basis. This cannot be shown for the commutator form, however in practice the rank is quite low and often effectively two. We have chosen to use the form in Eq. (4.50) because it is more straightforwardly generalized to higher dimensions and is easily applied with a sparse matrix multiply routine as mentioned above.

The DVR matrix elements of the flux operator in Eq. 4.50 are easily evaluated. They are given by

$$\mathbf{F}_{j,j'} = \frac{i}{\hbar}\mathbf{T}_{j,j'}[h(s_{j'}) - h(s_j)] \tag{4.51}$$

where $h(s_j)$ is the step function evaluated at the j^{th} DVR point, and $\mathbf{T}_{j,j'}$ is the kinetic energy matrix. This can be easily applied in a sparse matrix-multiplication scheme as required in the following multidimensional applications.

For simple barrier crossing reactions, such as the present example, one expects that $C_{fs}(t)$ will reach a constant value (a "plateau") at times on the order of $\hbar\beta$, giving the correct rate constant. At longer times, reflection from the edge of the grid gives spurious results. Thus, we determine the real propagation time, t, by specifying a unitless time factor, τ, according to the relation

$$t = \tau\, \hbar\beta. \tag{4.52}$$

The number of Chebychev terms, N_c, depends on the propagation time and can also be specified by a single factor, η,

$$N_c = \eta \frac{\Delta \mathrm{H}|t_c|}{2\hbar}. \tag{4.53}$$

In order to evaluate the efficiency of the method, we are interested in examining (1) the time needed to reach the plateau value of the correlation function, (2) the grid size necessary to obtain a reasonably wide plateau period, (3) the number of Chebychev terms needed in the expansion, and particularly important, (4) the number of Lanczos iterations necessary to converge the rate constant.

Fig. 4.1 shows the rate constant obtained from $C_{fs}(t)$ as a function of t for (a) T = 200 K, (b) T = 300 K, and (c) T = 1000 K for different grid sizes. ($k(T;t) = C_{fs}(t)/Q_r(T)$) Note that the plateau begins around 25 fs for T = 200 K and around 18 fs for T = 300 K, while for these temperatures $\hbar\beta \sim 38$ fs and 25 fs, respectively. In contrast, for T = 1000 K the plateau occurs at about $t = 10$ fs while $\hbar\beta \sim 7$. This behavior has previously been observed by Tromp and Miller[146,147] in the flux-flux autocorrelation function. At higher temperatures, the plateau time depends on the temperature-dependent dynamics of crossing the barrier, while at lower temperatures, the rate is dominated by tunneling. However, the tunneling time depends strongly on the barrier frequency but only weakly on the temperature (as shown for the harmonic barrier by Miller, Schwartz, and Tromp[58]).

For all temperatures we see that the plateau region may be extended by making the grid larger. This is particularly an issue at lower temperatures. Because we have a Boltzmann distribution of translational energies, at low temperatures there is a contribution from energies above the barrier even though the rate is dominated by tunneling. Reflection from the edges of the grid occurs at these higher energies which cross the barrier at times less than the tunneling time. Thus, lower temperatures require grids which extend farther away from the barrier. In Fig 4.1(a), for T = 200 K with $Q_{max} = 7.0$ a.u., a grid of 31 DVR points is necessary. For $Q_{max} = 8.0$ and 9.0 a.u. at the same temperature, 35 and 39 DVR points are required, respectively. At T = 1000 K, 39 DVR points are required for $Q_{max} = 4.0$ a.u., 49 points for $Q_{max} = 5.0$ a.u., and 59 points for $Q_{max} = 6.0$ a.u. We note that the grid sizes necessary for these

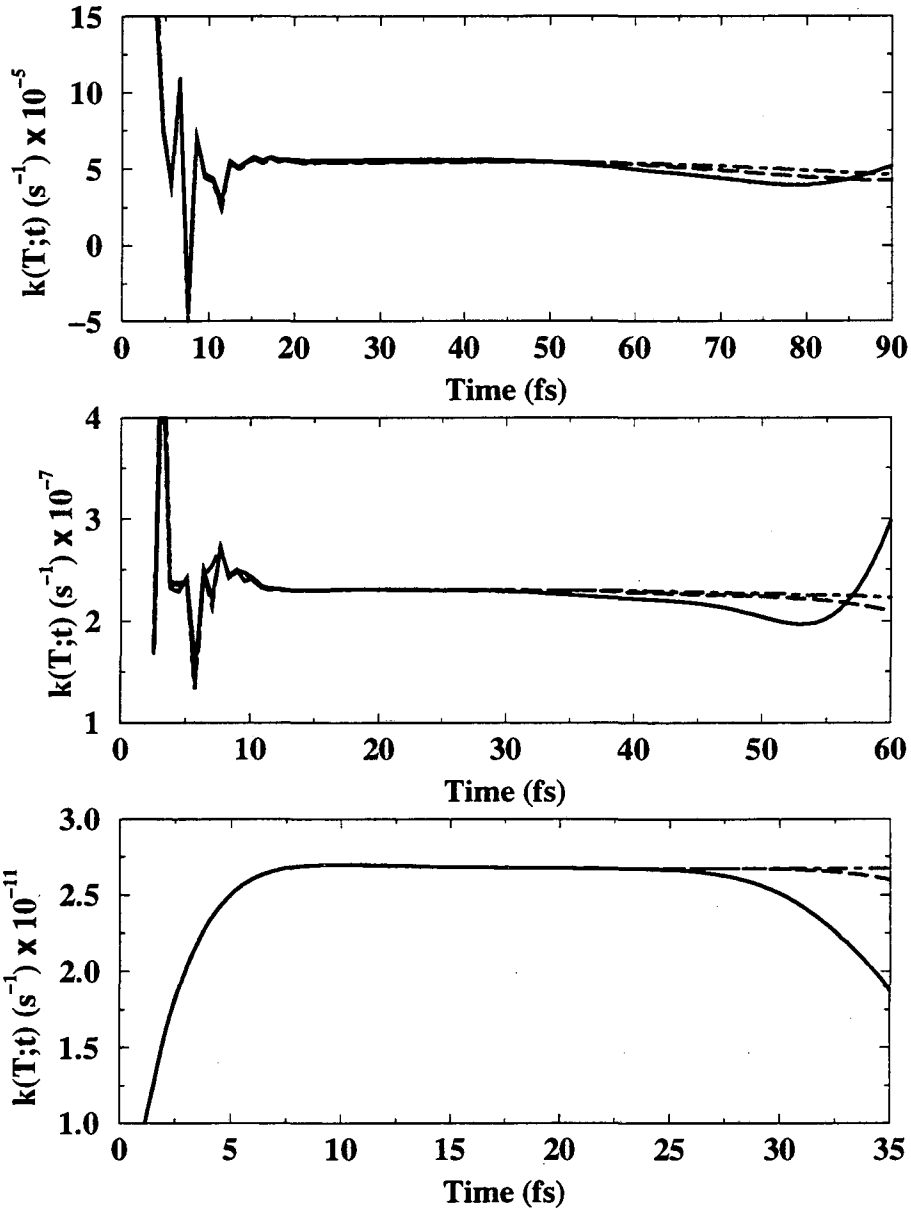

Figure 4.1: Thermal rate constants k(T;t) for the one-dimensional Eckart barrier calculated as a function of time from the flux-position correlation function for (a) T = 200 K, (b) T = 300 K, and (c) T = 1000 K. In (a) results are shown for grid sizes of Q_{max} = 7.0 a.u. (solid line), 8.0 a.u. (dashed line), and 9.0 a.u. (dot-dashed line). In (b) grid sizes of Q_{max} = 5.0 a.u. (solid line), 6.0 a.u. (dashed line), and 7.0 a.u. (dot-dashed line) are shown. And (c) shows results for grid sizes of Q_{max} = 4.0 a.u. (solid line), 5.0 a.u. (dashed line), and 6.0 a.u. (dot-dashed line).

calculations compare favorably with those used by Seideman and Miller[9] for direct calculations of the cumulative reaction probability.

For all the results shown, we have used $\eta = 1.3$ to determine the number of Chebychev terms. We have found this to give accurate results while minimizing the computational effort. For the results shown for the Eckart barrier in Fig. 4.1 we have used a maximum of about 230 Chebychev terms (for 1000 K at the longest times). The number of Lanczos iterations needed is 4 for all but the lowest temperatures. This implies a rank of 2, as an additional 2 iterations are needed to insure the trace is converged. At lower temperatures, approximately 10 eigenvalues are needed. This is due to our choice of the form of the flux operator. As discussed above, it is possible to express the flux operator as a dyadic,[175] so $\hat{C}_{fs}(t)$ will be of rank 2 at all temperatures. Eq. (4.50) does not guarantee this low rank, but we have chosen to use it because it is more easily applied to higher dimensions.

4.3.2 The Collinear H + H_2 Reaction

The collinear H + H_2 reaction serves as a standard test problem for reactive scattering methods and presents us with the first step to treating multidimensional systems. An accurate potential energy surface exists[66–68] and many exact calculations are available for comparison.[47,155,159]

We have used a DVR grid in the normal mode coordinates (q_1, q_2) of the transition state. In these coordinates, the optimum dividing surface is defined by $q_2 = 0$, where q_2 is the asymmetric stretch and q_1 is the symmetric stretch normal mode. The raw grid is truncated according to an energy cutoff: if the potential energy at a given DVR point is greater than a specified cutoff energy, V_{cut}, then that DVR point is discarded. The grid is also truncated in the asymptotic reactant and product valleys in the following manner: points are omitted if the translational Jacobi coordinate, $R(q_1, q_2)$ is larger than a specified value, R_{max}. The reactant partition function is given by

$$Q_r(T) = \left(\frac{\mu}{2\pi\hbar^2\beta}\right)^{1/2} \sum_v e^{-\beta\epsilon_v}, \tag{4.54}$$

where μ is the reduced mass associated with the relative translation of H and H_2. The ε_v are the vibrational energy levels of H_2 calculated numerically.

Fig. 4.2 shows the time dependence of $C_{fs}(t)$ for different grid sizes for (a) T = 300 K, (b) T = 500 K, and (c) T = 1000 K. At 300 K, the convergence is virtually the same as for the Eckart barrier; the plateau begins around 18 fs and is lengthened by increasing the extent of the grid. For T = 500 K and T=1000 K the plateau begins around 15 fs ($\hbar\beta \sim 15$ fs) and 13 fs, respectively. This is a slightly longer time at 1000 K than for the Eckart barrier. Again, for the lower temperatures, the time is determined by the tunneling time.

The size of the DVR grid for the results shown varies from 82 points for $R_{max} = 6.0$ at 300 K to 364 for $R_{max} = 6.0$ and T = 1000 K. Realistically, one needs a grid of around 100 points at 300 K, 150 points for 500 K, and 300 points for 1000 K to obtain converged results. This is on the order of the size of the basis used by Seideman and Miller[9] for calculating cumulative reaction probabilities. The number of Chebychev terms needed for the propagation in complex time was less that 700 for all cases. However, around 300 terms are usually sufficient for convergence.

Table 4.1 compares the results obtained from the flux-position correlation function with the results of Rom *et al.*[155] and Brown and Light.[47] The rate constants given are obtained by averaging the results obtained at several times within the plateau period. For all temperatures shown the averaged value is within 1% of the result for each time within the plateau. We note that at higher temperatures it is necessary to use a larger V_{cut}, as more of the potential energy surface is sampled. As in the case of the Eckart barrier, at lower temperatures we need a larger grid. The agreement between the previous results and our present method is excellent over a wide range of temperatures though our results are higher than those of Brown and Light[47] above 1000 K.

It is interesting to examine the structure of the eigenvalues of $\hat{C}_{fs}$. Table 4.2 shows typical sets of eigenvalues obtained at different temperatures. The pattern is similar to that seen by Manthe and Miller[12] in the eigenreaction probabilities. Namely, as the temperature is raised more eigenvalues contribute to the rate, corresponding to more states of the activated complex which are now energetically (or thermally)

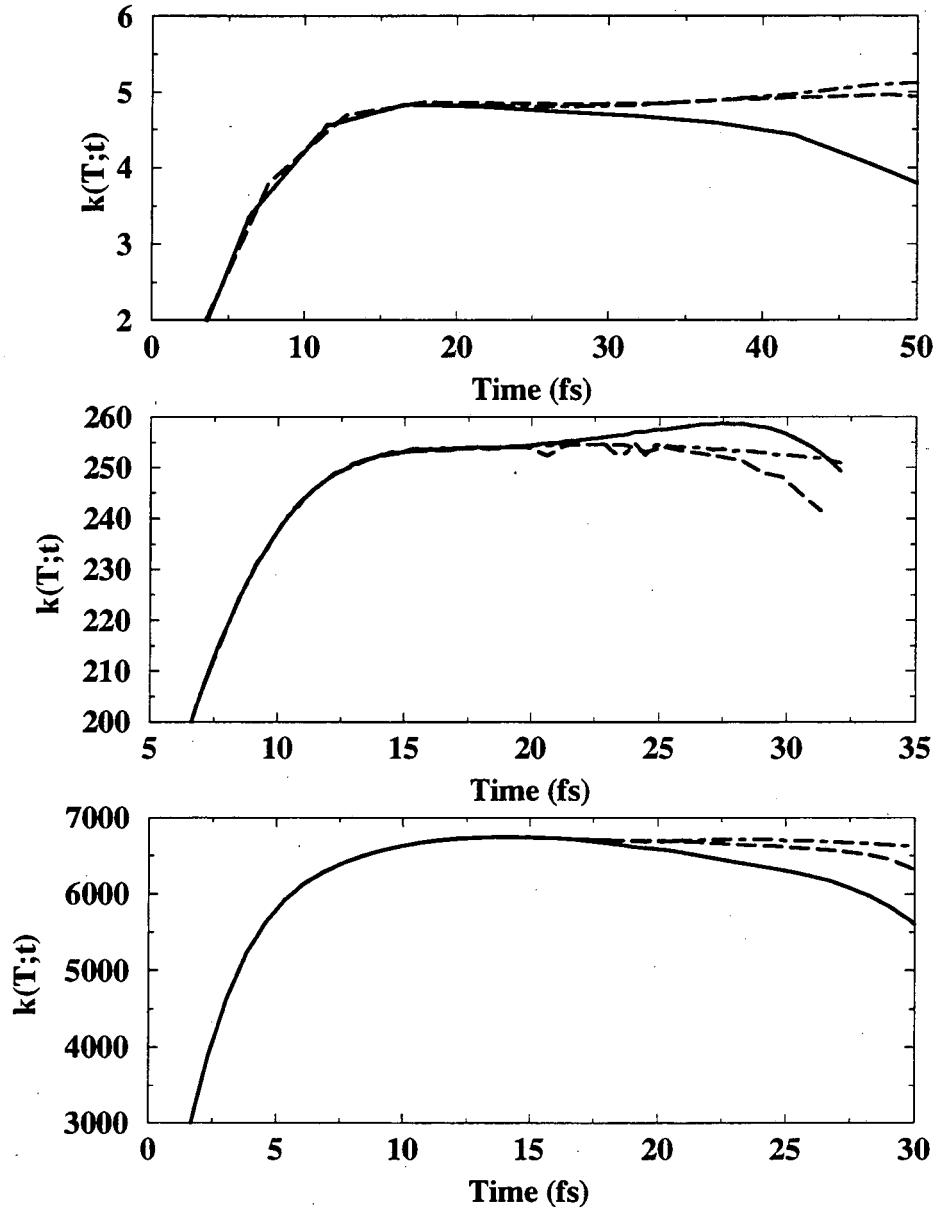

Figure 4.2: Thermal rate constants k(T;t) in units of cm molecule^{-1} s^{-1} for the collinear H + H_2 reaction calculated as a function of time from the flux-position correlation function for (a) T = 300 K, (b) T = 500 K, and (c) T = 1000 K. In (a) for T = 300 K results are shown for grid sizes of R_{max} = 6.0 a.u. (solid line), 6.5 a.u. (dashed line), and 7.0 a.u. (dot-dashed line). In (b) and (c) grid sizes of R_{max} = 5.0 a.u. (solid line), 5.5 a.u. (dashed line), and 6.0 a.u. (dot-dashed line) are shown.

	k(T)		
Temp. (K)	Present[a]	Ref. 155	Ref. 47
300	4.82	4.821	4.82
350	18.2	18.96	
400	54.3	54.69	
500	254	252.9	252
600	724	726.3	
700	1576	1574	
800	2853	2848	
900	4573	4557	
1000	6703	6692	6680
1500	2.29(4)[b]		2.21(4)
2000	4.76(4)		4.20(4)

[a]Calculated from Eq. (4.2.1).
[b]The number in parentheses is the power of 10.

Table 4.1: Thermal rate constants for the collinear H + H_2 reaction in units of cm molecule^{-1} s^{-1}

accessible. Also, as the temperature increases, the eigenvalues associated with a given state increase, representing an enhancement of the rate through that state. We have a different case than Manthe and Miller[12] because $\hat{C}_{fs}$ is not a positive definite operator. Therefore we have both positive and negative eigenvalues. The rate is given by the cancellation of the negative eigenvalues by the larger positive ones. This is consistent with the properties of the flux operator discussed above and in more detail by Park and Light.[158,159]

4.3.3 The D + H_2 Reaction

The D + H_2 reaction provides an ideal system for application of a new method for calculating rate constants. An accurate potential energy surface exists and there are recent exact[161,178] calculations of the thermal rate constant available for comparison.

We have carried out calculations of the thermal rate constant for the D + H_2 reaction for $J = 0$ on the LSTH (Liu-Siegbahn-Truhlar-Horowitz) potential

	Temperature				
	300 K	500 K	1000 K	1500 K	2000 K
	5.9251	377.572	7759.253	23872.925	43925.841
	0.8528	3.508	359.960	2203.398	8866.303
	0.4098	0.0264	16.542	51.169	1545.173
	0.1853		0.990	7.421	254.994
	0.0215		0.0267	0.938	53.182
	0.0035			0.063	19.687
					0.489
Eigenvalues					0.158
					-0.270
	-0.0025			-0.051	-14.112
	-0.0059		-0.094	-3.431	-41.140
	-0.0164		-0.462	-21.274	-139.343
	-0.0876	-0.0179	-5.206	-108.782	-520.493
	-0.1364	-0.258	-77.623	-763.604	-1233.238
	-2.1842	-122.604	-1360.776	-2691.187	-5244.550

Table 4.2: Eigenvalues of the $\hat{C}_{fs}$ operator for different temperatures. The eigenvalues have been divided by $Q_r(T)$ and are in units of cm molecule^{-1} s^{-1}. Only eigenvalues with absolute value greater than 0.001 are listed.

energy surface.[66–68] This surface is an analytical fit by Truhlar and Horowitz[66,67] to the *ab initio* calculations of Siegbahn and Liu.[68] The potential is thermoneutral with a symmetric barrier of 0.425 eV and a collinear transition state.

Details of the Calculation

Here we outline the procedure for the D + H_2 reactions (which is not largely different than for O + HCl). We have used the reactant Jacobi coordinates, as shown in Figure 4.3, where R is the distance from D to the center of mass of H_2, r the H_2 bond distance, and γ the angle between **R** and **r**. A discrete variable representation[21,22,37–39] has been chosen for the basis set. The radial sinc-function (DVR) of Colbert and Miller[37] is used for the coordinates r and R, while a symmetry-adapted Gauss-Legendre DVR is employed to describe the angular motion. Thus, the

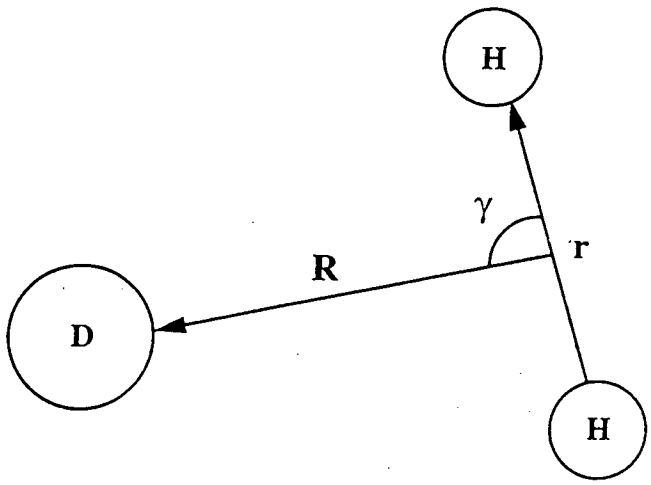

Figure 4.3: The Jacobi coordinates of the D + H_2 arrangement.

exchange symmetry of H_2 is taken into account and the total rate constant is obtained by performing both even and odd parity calculations and adding the resulting rate constants with the proper weights (1:3) from the nuclear spin statistics:

$$k(T) = k_{p=0}(T) + 3\,k_{p=1}(T). \tag{4.55}$$

Here p is the parity quantum number and $p = 0$ and 1 refer to even and odd parity, respectively. The reactant partition function is given by

$$Q_r(T) = \left(\frac{\mu_R}{2\pi\hbar^2\beta}\right)^{3/2} \left[\sum_{v,jeven} (2j+1)e^{-\beta\varepsilon_{v,j}} + 3\sum_{v,jodd} (2j+1)e^{-\beta\varepsilon_{v,j}}\right], \tag{4.56}$$

where the $\{\varepsilon_{v,j}\}$ are the energy levels of the isolated H_2 molecule (calculated numerically).

The general procedure for a calculation is as follows. First, a direct product DVR grid is laid out in the three coordinates. The spacing of grid points in the radial coordinates is determined by specifying the grid constant, N_B, where

$$\Delta x = \frac{2\pi}{N_B}\left(\frac{2\mu_x k_b T}{\hbar^2}\right)^{-1/2}, \tag{4.57}$$

with N_B typically between 10-13. [Note that in the symmetry-adpated Gauss-Legendre DVR only half of the grid points in an unsymmetrized basis in γ are used. Thus, the points lie only in the interval $(\pi/2, \pi)$ rather than $(0, \pi)$; the information in the other half of the range $(0, \pi/2)$ is redundant due to the symmetry.] The grid is then truncated according to two criteria: (1) A grid point in the reactant or product valley is discarded if the translational Jacobi coordinate for that arrangement, R_τ, (where τ is an arrangement index) is greater than some value, R_{max}. (Note that R_{max} can vary with arrangement.) (2) If the potential energy at a given grid point is larger than a specified cuttoff energy, V_{cut}, that grid point is discarded. The assumption being that at such a point the wavefunction will be vanishingly small and can be taken to be zero.

The basis set is defined by the parameters N_B, N_γ, p, V_{cut}, and R_{max}. The grid constant, N_B, determines the number of points per thermal de Broglie wavelength for the R and r coordinates. N_γ is the number of Gauss-Legendre DVR points used for the γ coordinate before symmetrization and p defines the parity of the calculation. If the potential energy at a DVR point is greater than V_{cut} that point is discarded. The grid is truncated in the asymptotic reactant valley if the translational Jacobi coordinate is greater than R_{max}. It is similarly truncated in the product valley by the same criterion, however, the Jacobi coordinates of the product arrangement are used.

For this system, the Hamiltonian for $J = 0$ is given by

$$\begin{aligned} \hat{H} &= -\frac{\hbar^2}{2\mu_R}\frac{1}{R}\frac{\partial^2}{\partial R^2}R - \frac{\hbar^2}{2\mu_r}\frac{1}{r}\frac{\partial^2}{\partial r^2}r + \left(\frac{\hbar^2}{2\mu_R R^2} + \frac{\hbar^2}{2\mu_r r^2}\right)\hat{\mathbf{j}}^2 + V(R, r, \gamma) \quad (4.58) \\ &= \hat{T}_R + \hat{T}_r + \hat{T}_\gamma + \hat{V}, \end{aligned}$$

where $\hat{\mathbf{j}}^2$ is the angular momentum operator associated with the diatom rotation. Note that the basis functions we choose for the finite basis reprentation associated with the DVR are actually of the form (for the sinc-function DVR in the R coordinate),

$$\tilde{\phi}_j = \frac{1}{R}\,\mathrm{sinc}\left[\frac{\pi}{\Delta x}(x - x_j)\right] = \frac{1}{R}\,\phi_j, \quad (4.59)$$

so that the matrix elements are of the form

$$\langle j'|\hat{A}|j\rangle = \int R^2 dR \tilde{\phi}_{j'}(R)\hat{A}\tilde{\phi}_j(R) = \int dR \phi_{j'}(R)\hat{A}\phi_j(R), \quad (4.60)$$

(where, of course, the integrals are evaluated by a specified quadrature). For the angular degrees of freedom a factor of $\sin^{1/2}\gamma$ is included in the basis functions in a similar fashion. The effect of this is to change the Jacobian from $R^2 r^2 \sin\gamma$ to 1 with a corresponding change in the Hamiltonian.

For the flux-flux correlation function, the one-dimensional propagators are calculated and stored for use in the split operator. This is implemented as follows: The operator $\hat{T}_\gamma$ does not commute with $\hat{T}_R$ and $\hat{T}_r$. Thus, we form the split operator in two steps, first separating out the radial kinetic energy terms,

$$e^{-i(\hat{H}-i\hat{\epsilon})\Delta t/\hbar} \simeq e^{-i\hat{T}_R\Delta t/2\hbar} e^{-i\hat{T}_r\Delta t/2\hbar} e^{-i(\hat{T}_\gamma+\hat{V}-i\hat{\epsilon})\Delta t/\hbar} e^{-i\hat{T}_r\Delta t/2\hbar} e^{-i\hat{T}_R\Delta t/2\hbar}, \tag{4.61}$$

and then the middle term is split once again:

$$e^{-i(\hat{T}_\gamma+\hat{V}-i\hat{\epsilon})\Delta t/\hbar} \simeq e^{-i\hat{T}_\gamma\Delta t/2\hbar} e^{-i(\hat{V}-i\hat{\epsilon})\Delta t/\hbar} e^{-i\hat{T}_\gamma\Delta t/2\hbar}. \tag{4.62}$$

Thus we need to obtain the matrices of the three one-dimensional kinetic energy propagators and the full-dimensional propagator containing the potential terms. The latter is simple since the potentials only depend on position and in a DVR are thus approximated as diagonal:

$$\langle j'|\, e^{-i(\hat{V}-i\hat{\epsilon})\Delta t/\hbar}\,|j\rangle = e^{-i[V(\mathbf{q}_j)-i\epsilon(\mathbf{q}_j)]\Delta t/\hbar}\,\delta_{j',j}, \tag{4.63}$$

where $\mathbf{q}_j$ represents the coordinates R, r, and γ for DVR grid point j. For the kinetic energy propagator matrix elements in the radial sinc-function DVR an analytical form can be obtained in terms of error functions (which can be evaluated numerically). Finally, the angular kinetic energy propagator is obtained by transforming to the corresponding finite basis representation (of Legendre polynomials) in which the propagator is diagonal and then transforming back:

$$\mathbf{P}_\gamma^{DVR} = \mathbf{U}\cdot\mathbf{P}_\gamma^{FBR}\cdot\mathbf{U}^\dagger, \tag{4.64}$$

where $\mathbf{P}_\gamma^{DVR}$ is the matrix of the angular kinetic energy propagator in the DVR, and similarly for $\mathbf{P}_\gamma^{FBR}$. The transformation matrix is

$$(\mathbf{U})_{k,l} = \sqrt{w_k}\,\sqrt{1+(-1)^{p+l}}\,\tilde{P}_l(cos\gamma_k), \tag{4.65}$$

where $k = 0, 1, \ldots, N/2$ is the DVR grid point index, $l = 0, 1, \ldots, N-1$ the Legendre polynomial index, w_k the weight for the Gauss-Legendre quadrature, $\tilde{P}_l$ the normalized Legendre polynomial, and p the parity quantum number. Also,

$$\left(\mathbf{P}_{\gamma}^{FBR}\right)_{l,l'} = \exp\left\{-\frac{i\Delta t}{\hbar}\left[1+(-1)^{p+l}\right] l(l+1)\hbar^2\right\}\ \delta_{l,l'}, \tag{4.66}$$

is the propagator in the finite basis representation. The split operator described above is applied using sparse matrix multiplication routines.

Once the propagator is known the Lanczos algorithm is carried out for the Boltzmannized flux operator to obtain the eigenvalues and eigenfunctions. Each eigenfunction is then propagated in real time to obtain the flux-flux correlation function which is integrated to obtain the thermal rate constant.

One additional note is necessary on the form of the absorbing potential. We have used a quartic function of the translational Jacobi coordinate of each arrangement for $\epsilon(\mathbf{q})$. Namely, $\epsilon(\mathbf{q}) = \epsilon_p(R_p) + \epsilon_r(R_r)$ where

$$\epsilon_\tau(R_\tau) = \lambda_\tau \left(\frac{R_\tau - R_{max,\tau}}{R_{max,\tau} - R_{0,\tau}}\right)^4, \tag{4.67}$$

where $\tau = r, p$ is the arrangement label, $R_{0,\tau}$ is the point where the absorbing potential "turns on," $R_{max,\tau}$ is the end of the absorbing potential (and the truncated grid), and λ_τ is the strength parameter.

Flux-Position Correlation Function Results

Fig. 4.4 illustrates the plateau period for the D + H_2 reaction for (a) T = 300 K, (b) T = 500 K, and (c) T = 1000 K. In this case at T = 300 K the plateau begins at 22 fs and at 20 fs for T = 500 K, both are slightly longer times than for the collinear H + H_2 case. At T = 1000 K, the plateau begins around 22 fs, significantly longer than for collinear H + H_2 or the Eckart barrier. The grid sizes for both temperatures (R_{max} = 6.0 a.u. for 300 K, and R_{max} = 5.0 a.u. for 500 K and 1000 K) are comparable to those needed for calculating the cumulative reaction probability. At the highest temperatures, about 20 Lanczos iterations are needed to converge the rate constant. For all temperatures the number of Chebychev terms necessary is less than 1000.

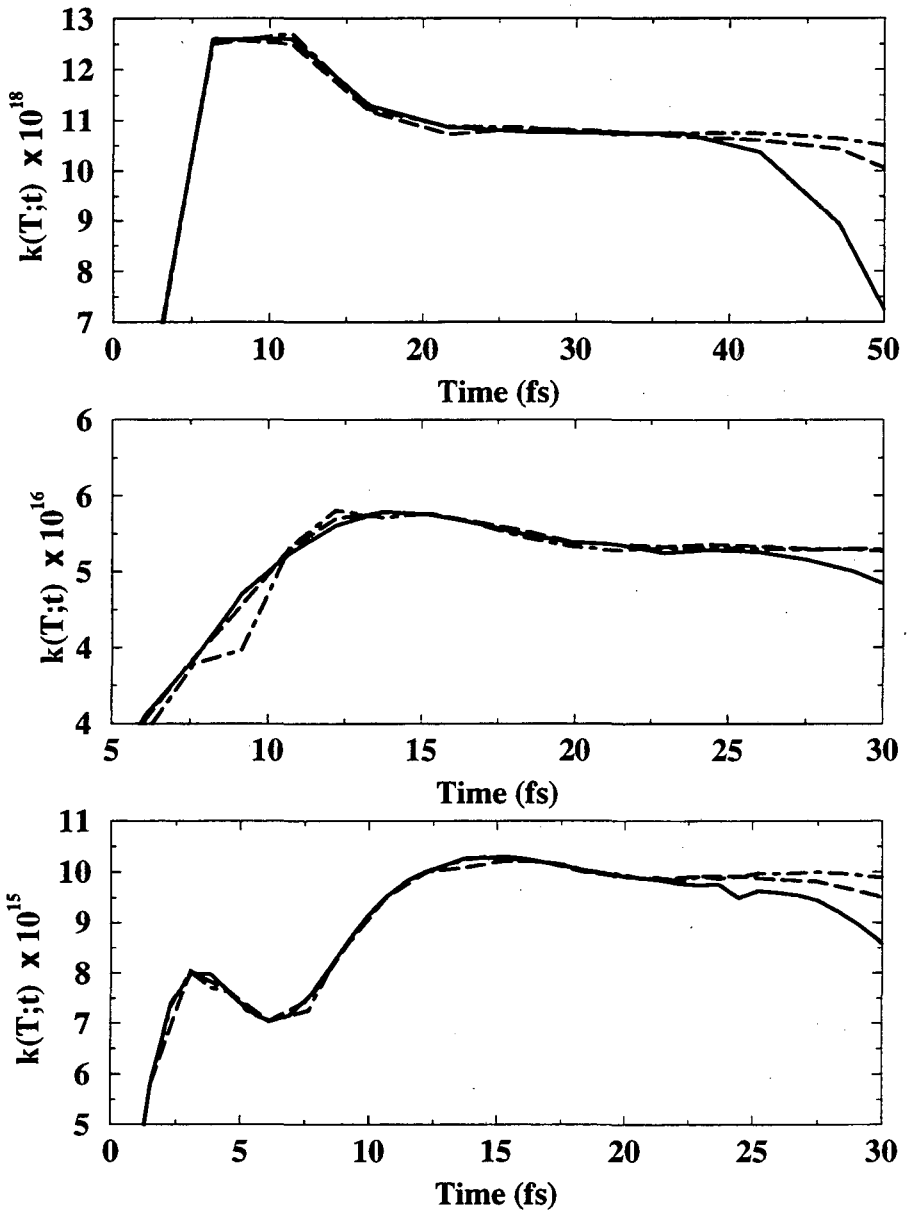

Figure 4.4: Thermal rate constants k(T;t) in units of cm^3 $molecule^{-1}$ s^{-1} for the three dimensional D + H_2 reaction calculated as a function of time from the flux-position correlation function for (a) T = 300 K, (b) T = 500 K, and (c) T = 1000 K. In (a) results are shown for grid sizes of R_{max} = 6.0 a.u. (solid line), 6.5 a.u. (dashed line), and 7.0 a.u. (dot-dashed line). In (b) and (c) grid sizes of R_{max} = 5.0 a.u. (solid line), 5.5 a.u. (dashed line), and 6.0 a.u. (dot-dashed line) are shown.

	k(T)		
Temp. (K)	Present[a]	Ref. 178	Ref. 161
300	1.07(-17)	8.17(-18)	9.2(-18)
500	5.15(-16)	5.22(-16)	5.6(-16)
700	2.96(-15)	3.00(-15)	3.2(-15)
900	7.66(-15)	7.59(-15)	8.1(-15)
1100	1.36(-14)	1.33(-14)	1.4(-14)
1300	1.96(-14)	1.94(-14)	2.1(-14)
1500	2.50(-14)	2.53(-14)	2.7(-14)

[a]Calculated from Eq. (4.2.1).

Table 4.3: Thermal rate constants for the three-dimensional D + H_2 ($J = 0$) reaction in units of cm^3 $molecule^{-1}$ s^{-1}

Table 4.3 compares the results from the flux-position correlation function to the results of Mielke *et al.*[178] and Park and Light.[161] As for the collinear H + H_2 results, the rate constants given in the table are obtained by averaging the results obtained at several times within the plateau period. For all temperatures shown the averaged value is within 2% of the result for each time within the plateau. The present method gives the rate constant in excellent agreement with the results of Mielke *et al.*[178] for temperatures above 300 K. At 300 K the rate is overestimated by the present method by about 30 %.

Flux-Flux Correlation Function Results

The flux-flux autocorrelation function for the D + H_2 reaction is shown in Figure 4.5 for (a) T = 300 K, (b) T = 500K, and (c) T = 1000 K. Fig 4.5(a) compares the correlation functions calculated with (solid line) and without (dashed line) an absorbing potential included in the real time propagation. The two correlation functions are virtually identical for the first 25 fs. At larger times, however, the absence of the absorbing potential results in unphysical reflection form the edge of the finite DVR grid and the correlation function diverges. Incorporating an absorbing potential eliminates this spurious reflection and the correlation function converges smoothly to zero.

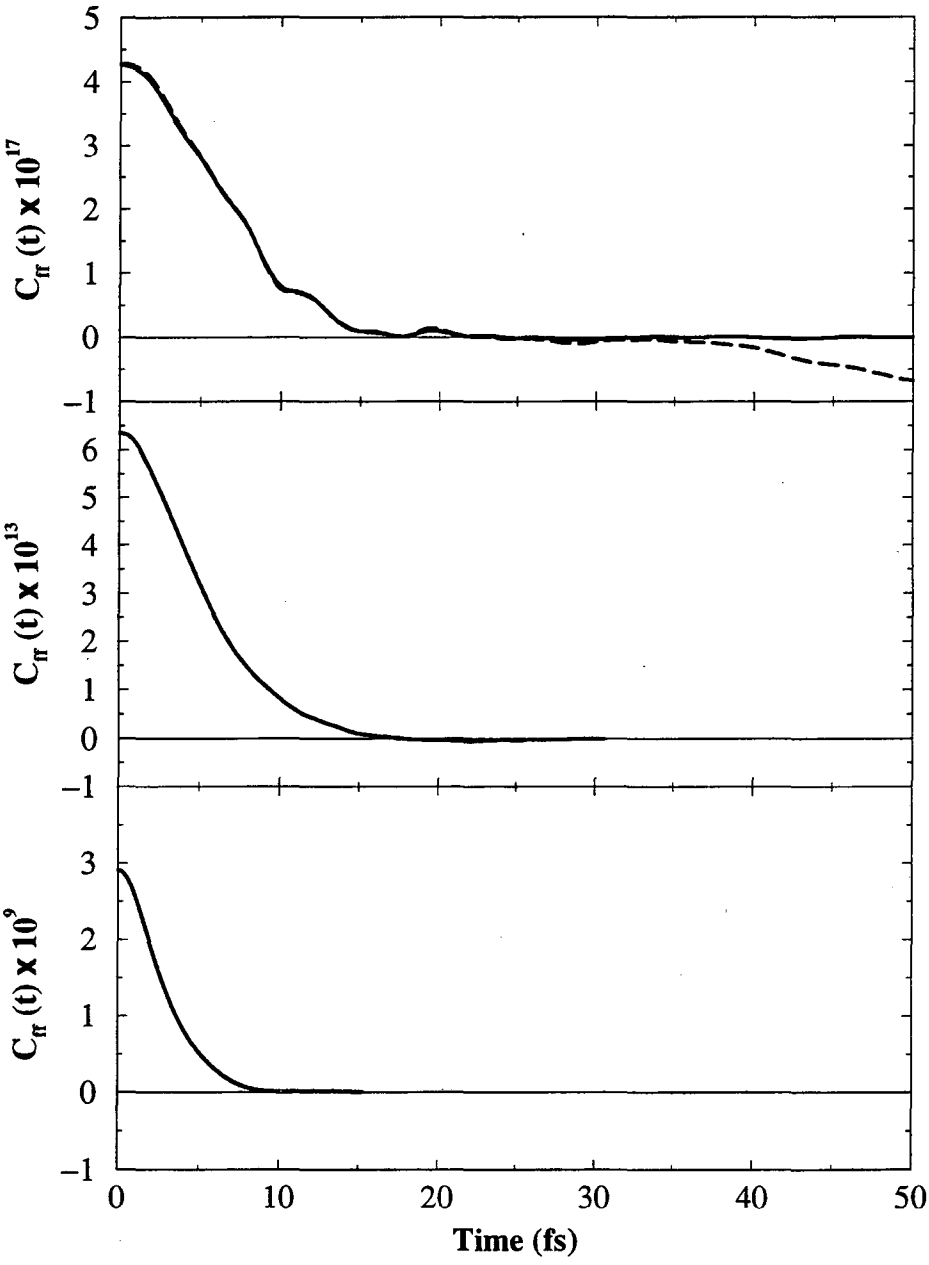

Figure 4.5: The flux-flux autocorrelation function for the D + H_2 reaction at (a) T = 300 K with (solid line) and without (dashed line) an absorbing potential, (b) T = 500 K, and (c) T = 1000 K. The units of $C_{ff}(t)$ are (atomic units of time)$^{-2}$.

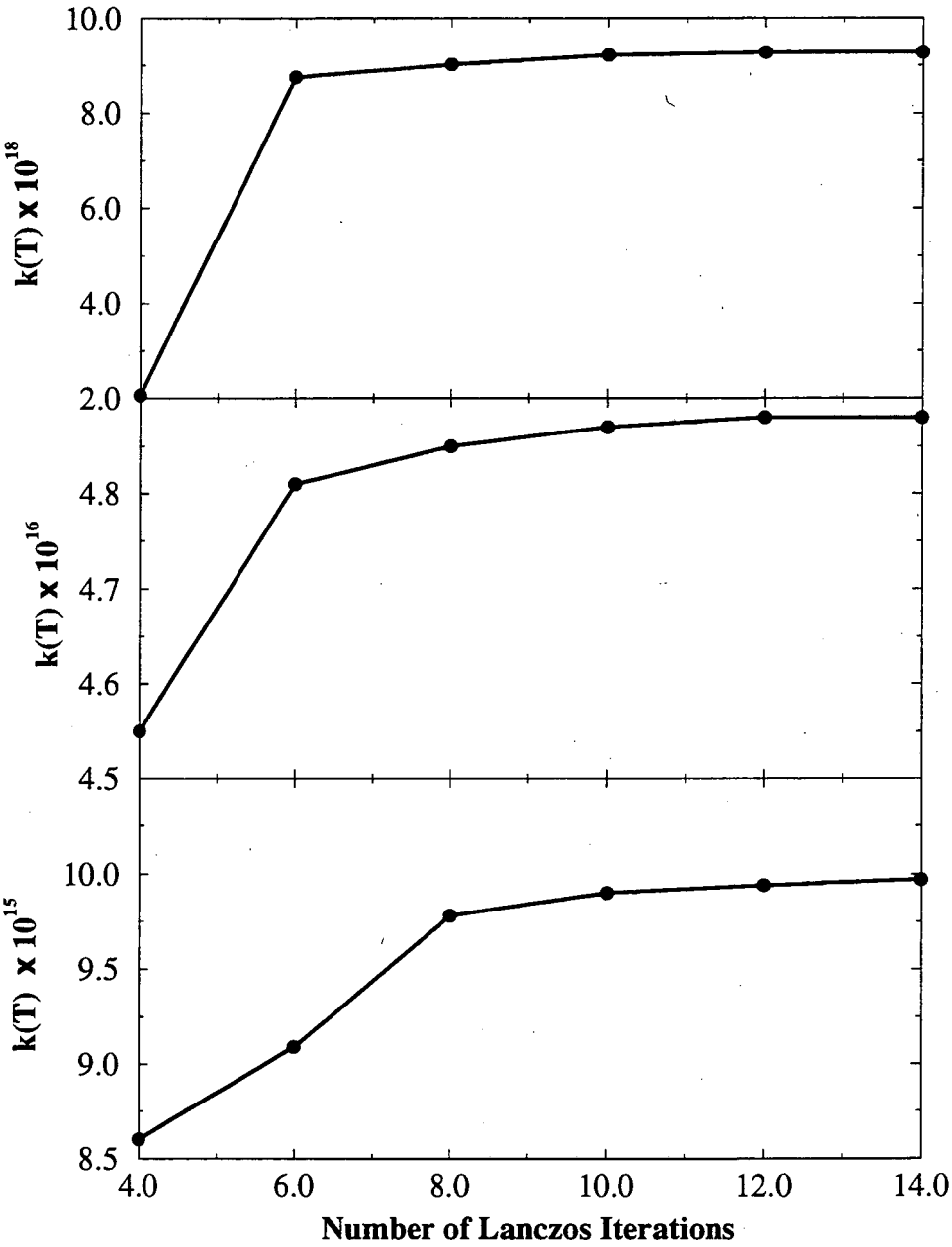

Figure 4.6: The thermal rate constant vs. the number of Lanczos iterations (*i.e.*, the number of eigenvalues of the Boltzmannized flux operator used to calculate the trace) at (a) T = 300 K, (b) T = 500 K, and (c) T = 1000 K.

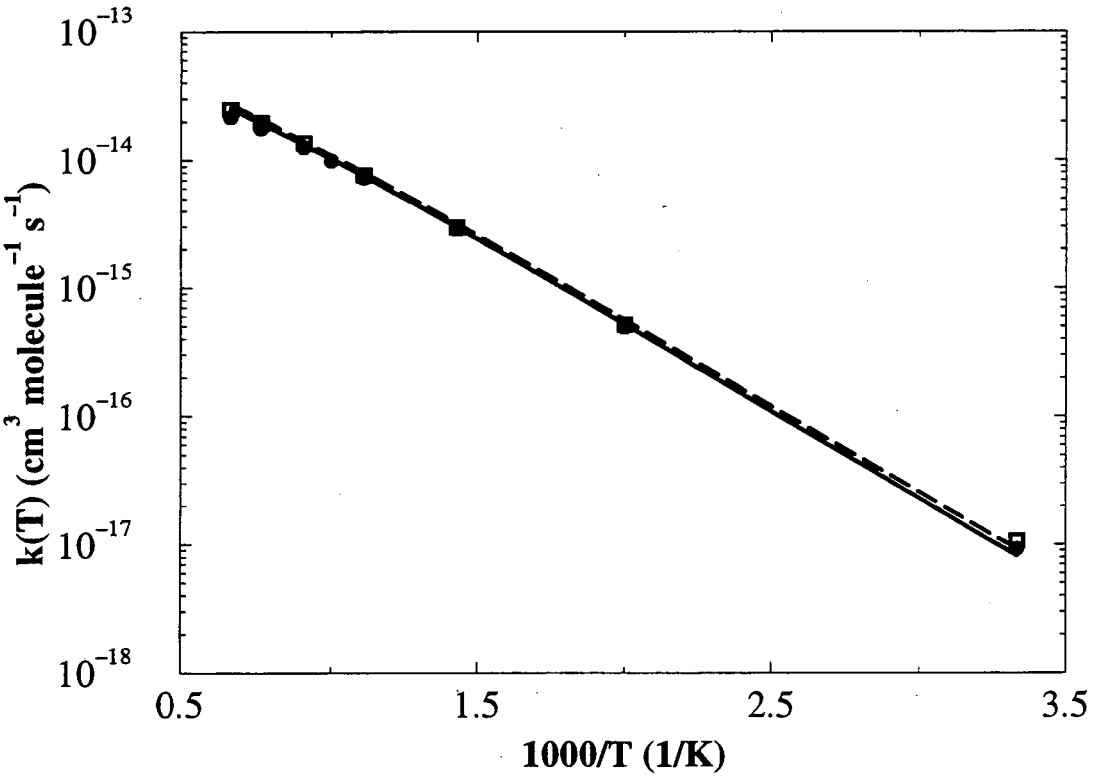

Figure 4.7: Arrhenius plot of the thermal rate constant, $k(T)$ vs. $1000/T$ for the D + H_2 reaction. The rates calculated from the flux-flux correlation function are shown as solid circles, the results of Mielke *et al.* (Ref. 178) as a solid line, and the results of Park and Light (Ref. 161) as a dashed line.

The correlation functions also illustrate the TST-like nature of this method. The propagation time required for the correlation function to decay to zero is quite short ($<$ 25 fs for all the temperatures shown here). This is analogous to the short times one would need to follow trajectories starting at the transition state forward and backward in time to obtain the exact classical rate constant. The present method obtains the exact quantum rate constant from short time dynamics in the region of the transition state. The time for the correlation function to decay to zero for a direct reaction over a barrier (such as this one) is expected to be on the order of $\hbar\beta$; naturally the time decreases with increasing temperature. Indeed, for D + H_2 we find the correlation function converges to zero in 22 fs at 300 K for which $\hbar\beta \simeq 25$ fs, in

15 fs at 500 K ($\hbar\beta \simeq 15$ fs), and in 10 fs at 1000 K ($\hbar\beta \simeq 8$ fs). While at higher temperatures the correlation function decreases smoothly, at 300 K oscillations are observed which can be attributed to a small amount of recrossing of the dividing surface; at this temperature almost all of the energies in the Boltzmann distribution lie below the barrier.

The rate constant vs. the number of Lanczos iterations (number of eigenvalues of the Boltzmannized flux operator) is plotted in Fig. 4.6 for (a) T = 300 K, (b) T = 500 K, and (c) T =1000 K. At all temperatures a reasonable approximation (< 10% error) to the rate can be obtained with just 6 eigenvalues; the rate constant is converged after only 12 eigenvalues of the Boltzmannized flux operator (corresponding to about 6 states of the activated complex contributing to the rate). This small number can be compared with the size of the DVR basis used for these calculations: approximately 690 grid points at 300 K, 950 at 500 K, and 1750 at 1000 K. Thus, while the size of the basis has increased by more than a factor of two, the number of eigenvalues of the Boltzmannized flux operator needed to obtain the rate has not changed.

An Arrhenius plot of the rate constant vs. 1000/T is shown in Fig. 4.7. The present calculated rate constants for $J = 0$ are compared with previous exact calculations by Park and Light[161] and Mielke *et al.*[178] (The calculations of Park and Light also obtained the rate constant from the flux-flux autocorrelation function.) Good agreement is observed between the present results and the previous calculations over the temperature range 300 - 1500 K.

4.3.4 The O + HCl → OH + Cl Reaction

Details of the Calculation

We have chosen to use the Jacobi coordinates of the H + OCl arrangement as shown in Figure 4.8: r is the O-Cl bond distance, R the distance from H to the center-of-mass of O-Cl, and γ the angle between **r** and **R**. These coordinates describe the interaction region well, and they provide a framework for approximate angular momentum decoupling schemes (such as the centrifugal sudden (CS) approximation

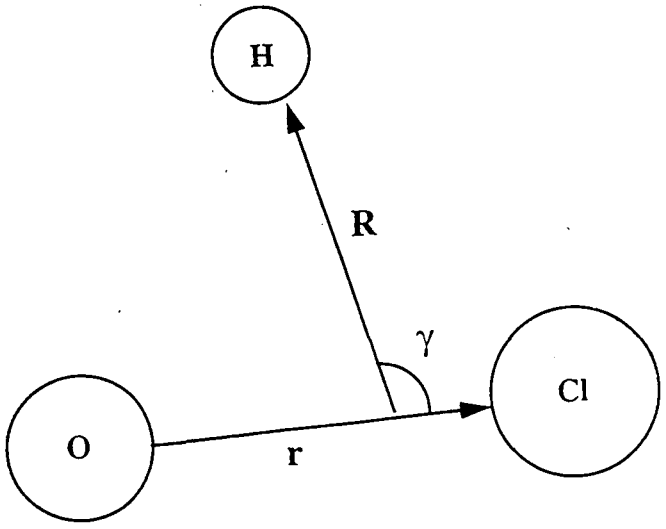

Figure 4.8: The Jacobi coordinates of the H + OCl arrangement.

or the J-Shifting approximation[109]) since to a good approximation one expects the projection of the total angular momentum along the O-Cl axis to be conserved (because the H atom is so light compared to O and Cl).

The $J = 0$ Hamiltonian in this coordinate system is given by

$$\hat{H} = -\frac{\hbar^2}{2\mu_R}\frac{1}{R}\frac{\partial^2}{\partial R^2}R - \frac{\hbar^2}{2\mu_r}\frac{1}{r}\frac{\partial^2}{\partial r^2}r + \left(\frac{1}{2\mu_R R^2} + \frac{1}{2\mu_r r^2}\right)\hat{\ell}^2 + \hat{V}(R, r, \gamma) \quad (4.68)$$

where $\hat{\ell}^2$ is the orbital angular momentum operator associated with the motion of H about the center of mass of O-Cl. μ_R and μ_r are the reduced masses associated with the coordinates R and r, respectively.

We have included the effects of nonzero total angular momentum by means of two approximate methods. In the J-shifting approximation,[109] it is assumed that rotational and internal motion are separable, so that the rotational energy E_{JK} simply adds to the $J = 0$ Hamiltonian of Eq. (4.68), and furthermore, E_{JK} is usually approximated by using rotation constants corresponding to the transition state geometry of the potential energy surface. Following Koizumi *et al.*,[179] the transition state geometry is assumed to be a symmetric top and the rotational energy levels are

given by

$$E_{JK} = \frac{J(J+1)\hbar^2}{2I_B} + \left(\frac{1}{2I_A} - \frac{1}{2I_B}\right) K^2\hbar^2, \tag{4.69}$$

where the moments of inertia I_B and I_A are effectively that of O-Cl and of H about the O-Cl axis, respectively. The values used by Koizumi *et al.* are $I_B = 4.16 \times 10^5$ a.u. and $I_A = 1.70 \times 10^3$ a.u. The total rate constant can then be obtained by a single calculation for $J = 0$ as

$$k(T) = k_{J=0}(T)\, Q_{JS}(T), \tag{4.70}$$

$$Q_{JS}(T) = \sum_{J=0} (2J+1) \sum_{K=-J}^{J} e^{-\beta E_{JK}}, \tag{4.71}$$

where $Q_{JS}(T)$ is the rotational partition function.

The centrifugal sudden, or helicity conserving approximation (HCA) is a more sophisticated approximation in which the coriolis coupling terms in the body-fixed representation of the Hamiltonian are neglected.[180] A difference in our present treatment from the usual helicity conserving approximation is that we have chosen the diatom vector **r** (the O-Cl vector) as the body-fixed quantization axis — because the projection of total angular momentum onto it is most nearly conserved — rather than the atom-diatom vector **R** as is usually done.[181] This results in the following term,

$$\hat{H}_{HCA} = \frac{[J(J+1) - 2K^2]\hbar^2}{2\mu_r r^2}, \qquad |K| \leq \min(J, \ell), \tag{4.72}$$

being added to the $J = 0$ Hamiltonian of Eq. (4.72). Within this approximation J and K are conserved quantum numbers and appear simply as parameters in the Hamiltonian. One calculates the rate via Eq. (4.40) for each J and K, and then the total rate constant is given by

$$k(T) = \sum_{J=0} (2J+1) \sum_{K=-J}^{J} k_{JK}(T). \tag{4.73}$$

The helicity conserving approximation is thus more expensive to apply than the J-shifting approximation because the latter requires only the $J = 0$ calculation (*cf.* Eq. (4.71)) while the former requires a separate calculation — each of which is essentially the effort of the $J = 0$ calculation — for each value of J and K. In

practice, though, things are greatly simplified because the dependence of k_{JK} on J and K is very simple. *E.g.*, if the J-shifting approximation were accurate, then Eq. (4.71) shows the J and K dependence is

$$\ln k_{JK}(T) = \text{constant} - \alpha J(J+1) - \eta K^2. \tag{4.74}$$

It will be seen in the next Section that Eq. (4.74) is not quantitatively correct, but nevertheless one needs to carry out calculations for only a few values of J and K and interpolate between them in order to evaluate the sum in Eq. (4.73).

We have chosen to use a discrete variable representation[21,39,38,37] (DVR) basis. This has the advantages that the Hamiltonian is sparse in a multidimensional case and no integrals over the potential need to be evaluated. Specifically, we have used the radial sinc-function DVR developed by Colbert and Miller[37] for the r and R coordinates and a Gauss-Legendre DVR for the γ coordinate. In the case where the HC approximation is used, an associated Legendre DVR is used since the projection quantum number is nonzero.[182–184,26]

The basis set implemented for this problem is much the same as that for the D + H_2 reaction: sinc-function DVRs for the radial coordinates and an unsymmetrized Gauss-Legendre DVR for the angular degree-of-freedom. For this problem we have found $N_B = 11-13$ to be sufficiently large. N_γ is the number of Gauss-Legendre DVR points used for the γ coordinate (usually, $N_\gamma \simeq 30$). As is typical, a "raw" grid is laid down in the Jacobi coordinates of the H + OCl arrangement and truncated by an energy cuttoff: if the potential energy at a DVR point is greater than V_{cut} that point is discarded. The grid is also truncated in the asymptotic reactant, O + HCl, valley if the translational Jacobi coordinate is greater than R_{max}. It is similarly truncated in the OH + Cl and H + OCl valleys using the translational Jacobi coordinates of those arrangements.

The split operator scheme used for here is the same as that described above for the D + H_2 reaction. Note that since only the 1D kinetic energy matrices and the values of the potential need to be stored, the memory requirements are quite low: usually less than 10 MB of core memory and never more than 30 MB even for the largest basis of about 19,000 DVR grid points. The optimum time step is determined

by calculating the rate constant for successively smaller Δt until the result does not change.

As in all the applications presented here, the commutator form of the flux operator as given in Eq. (4.50) is used here. In addition to it's usefulness in sparse matrix-multiplication routine, it is particularly more convenient than the differential form when the dividing surface — defined by the equation $s(\mathbf{q})$ — is expressed in terms of coordinates other than those used to represent the Hamiltonian. The dividing surface used in this study is defined by $r_{OH} - r_{HCl} + 0.29 = 0$ (with all distances in atomic units).

The form (and even the magnitude) of the absorbing potentials used for the O + HCl reaction are the same as those for D + H_2.

Results and Discussion

We have calculated the thermal rate constants for the O + HCl reaction on the Koizumi, Schatz, and Gordon (KSG)[179] potential energy surface which is an analytical fit to *ab initio* calculations,[179,185] but with the barrier height scaled down from 18.8 to 8.5 kcal/mole to match the experimental rate[186] at T = 295 K. This reaction provides a rigid test of a method for calculating thermal rate constants. The heavy masses involved demand a large basis and the heavy-light-heavy nature of the reaction requires that the correlation function be calculated for long times.

There have been numerous experimental measurements of the thermal rate constant for the O + HCl reaction,[186–192] in addition to several theoretical[179,187,193,194] studies. Brown and Smith[187] and Persky and Broida[193] carried out quasiclassical trajectory calculations on semi-empirical LEPS (London-Eyring-Polanyi-Sato) surfaces. These surfaces all featured a collinear transition state geometry. However, *ab initio* calculations on the system indicate that the transition state is significantly bent with an O–H–Cl angle of about 135°.[179,185,195] The KSG potential energy surface, with a bent transition state, was originally used by Koizumi *et al.* to calculate total and state-selected thermal rate constants. These calculations were carried out by integrating coupled channel equations in hyperspherical coordinates to obtain the

state-to-state reaction probabilities which were then used to obtain the rate constants (with a J-shifting approximation). Moribayashi and Nakamura have also carried out quantum reactive scattering calculations on the KSG surface (as well as a LEPS surface of Persky and Broida) by integrating coupled channel equations in hyperspherical coordinates.[194] They obtained state-selected and cumulative reaction probabilities as well as state-selected (but not total) rate constants. In addition they examined different approximations for including the effects of nonzero total angular momentum.

Recently, *ab initio* calculations have been carried out (and a potential energy surface obtained) by Ramachandran, Senekowitsch, and Wyatt giving a barrier height of 17.8 kcal/mole.[195] This is in reasonable agreement with the *ab initio* barrier height of 18.8 kcal/mole used in the KSG surface *before* scaling but significantly larger than the best *ab initio* estimate of 11.9 kcal/mole.[179] Rate constants have not yet been computed on this surface.

The KSG potential energy surface has a bent transition state geometry with an O–H–Cl angle of 133.4° and a barrier height of 8.5 kcal/mole.[179] The O + HCl → OH + Cl reaction is endothermic. In contrast, the H + OCl asymptotic arrangement is ∼ 40 kcal/mole higher in energy than O + HCl and is therefore not a relevant product channel. Thus we refer to OH + Cl as "products" without ambiguity.

There is an excited ($^3A'$) electronic state surface which is degenerate at linear geometries with the ($^3A''$) ground state. The details of this surface are not fully known and it is not included in the scattering calculations here. However, following Koizumi *et al.*[179] the rate constants presented here have been multiplied by the factor

$$f(T) = 3/(5 + 3e^{-228/T} + e^{-326/T}) \tag{4.75}$$

to approximately account for collisions that end up on the excited state as opposed to the ground state surface.

Figure 4.9 shows the $J = 0$ flux-flux autocorrelation function for the O + HCl reaction at T = 300 K. At very short times the correlation function decays rapidly and goes through zero around 7 fs, corresponding to an initial passage of flux across the dividing surface towards products. This is followed by a negative lobe indicating flux returning across the dividing surface from products to reactants. It is expected

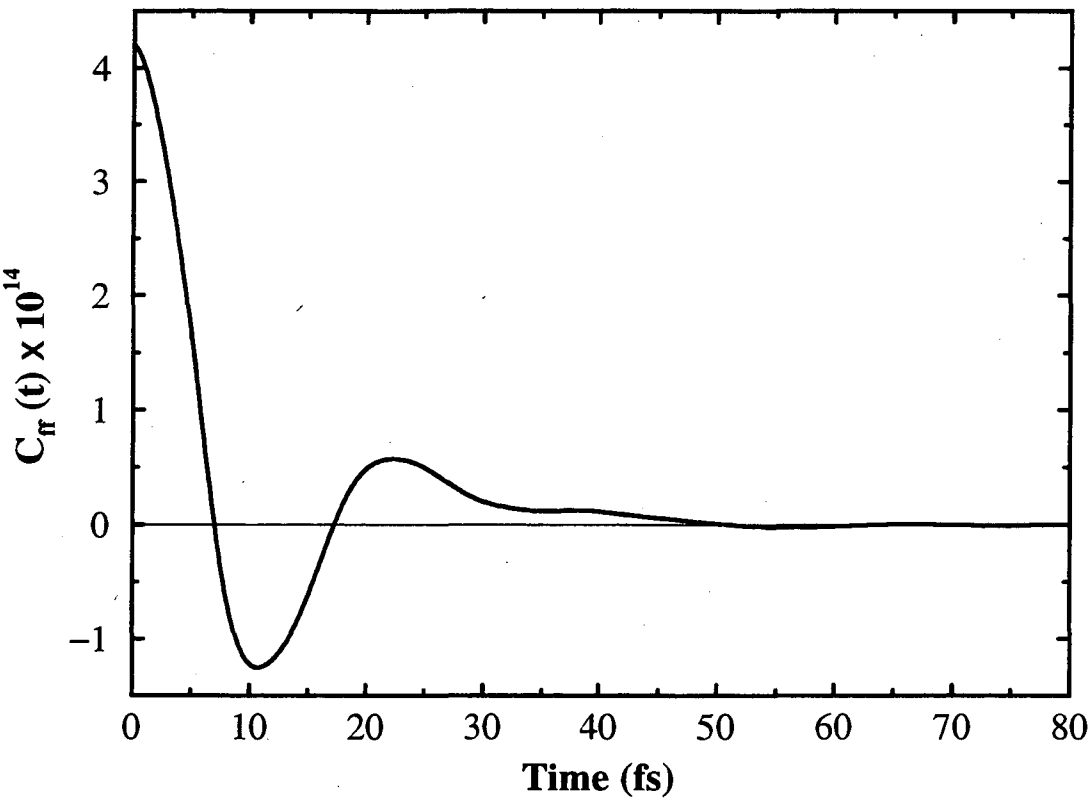

Figure 4.9: The flux-flux autocorrelation function for the O + HCl reaction at T = 300 K. The units of the correlation function are (atomic units of time)$^{-2}$.

that a heavy-light-heavy system such as O + HCl should exhibit significant recrossing of the transition state. In a classical picture the H atom in the region of the transition state is trapped between the massive O and Cl and bounces back and forth between these two collision partners. This is manifested in the oscillations in the correlation function — the negative lobe is immediately followed by a positive one representing a second passage of flux towards products. (Of course the oscillations observed depend on the position of the flux dividing surface which has not been optimized here for minimum recrossing.) The correlation function eventually dies to zero around 50 fs. This is twice the time that would be expected in the case of a direct reaction (which would be $\sim \hbar\beta \simeq 25$ fs).[58]

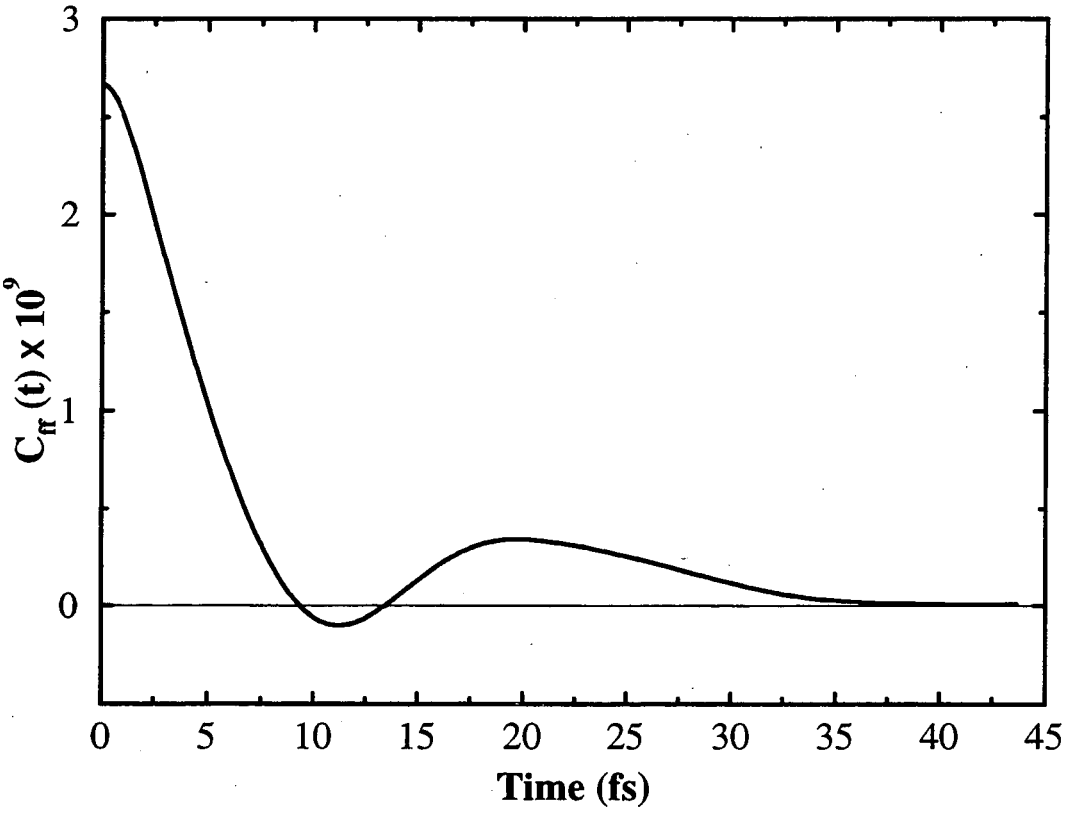

Figure 4.10: The flux-flux autocorrelation function for the O + HCl reaction at T = 700 K. The units of the correlation function are (atomic units of time)$^{-2}$.

Figure 4.10 shows the $J = 0$ flux-flux autocorrelation function for the O + HCl reaction at T = 700 K. This correlation function is similar to that shown in Fig. 4.9 for T = 300 K. There is a rapid initial decay to zero followed by a negative lobe and then a postive lobe. At this temperature the correlation function decays to zero in approximately 35 fs (*cf.* $\hbar\beta \simeq 11$ fs). However, in this case the negative lobe is much smaller (relative to the initial value of the correlation function) than for the lower temperature, while the following positive lobe is about the same magnitude. However the smaller oscillations observed at T = 300 K are not present here. While in a variational TST picture the optimum dividing surface for minimizing recrossing may change with temperature we have used the same dividing surface at all temperatures.

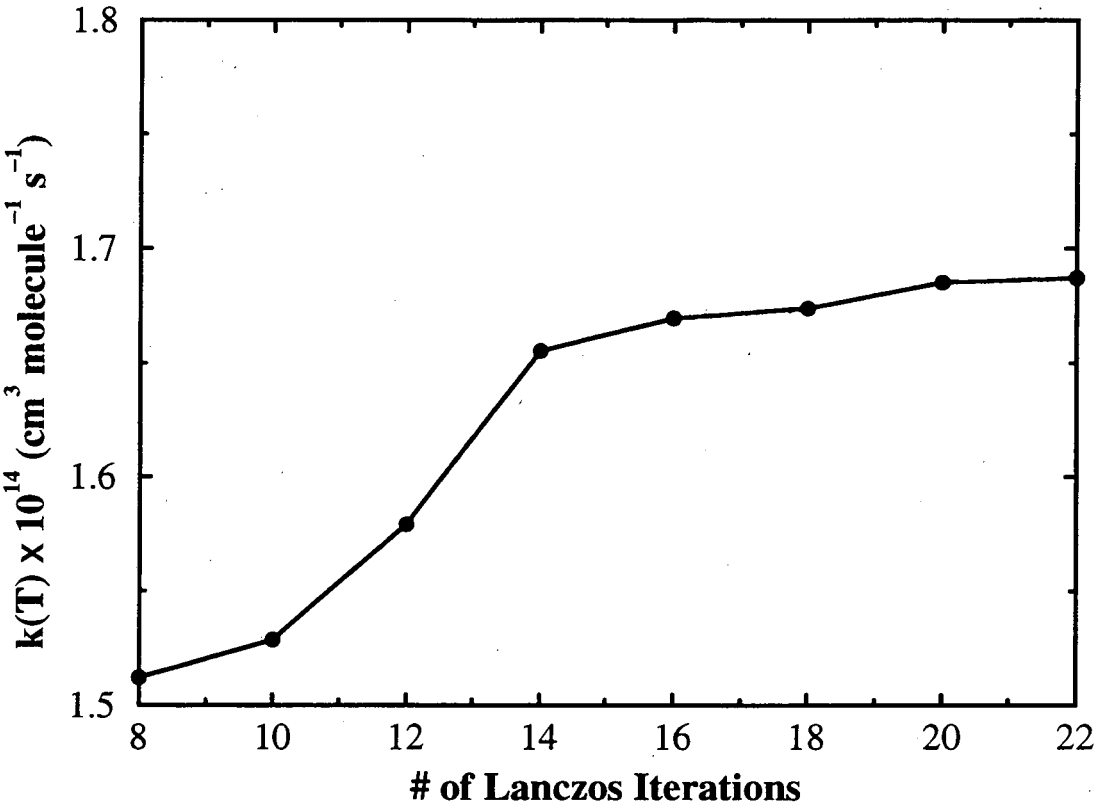

Figure 4.11: The thermal rate constant vs. the number of Lanczos iterations (*i.e.*, the number of eigenstates of the Boltzmannized flux operator used to obtain the rate) at T = 400 K.

Figure 4.11 shows the (J-shifted) rate constant versus the number of Lanczos iterations for T = 400 K. Recall that each Lanczos iteration corresponds to an eigenvalue (and eigenvector) of the Boltzmannized flux operator which is included in the calculation of the rate. At this temperature the rate converges with around 20 iterations implying that there are 9 or 10 thermally accessible states of the activated complex contributing to the reaction rate. With the heavy masses of the oxygen and chlorine it is expected there will be more states accesible at a given temperature than for a reaction like H + H_2 where all the atoms are "light." The number of eigenvalues that it is necessary to include changes very mildly with temperature; at the highest temperature (T = 700 K) about 24 Lanczos iterations are required. Note that the

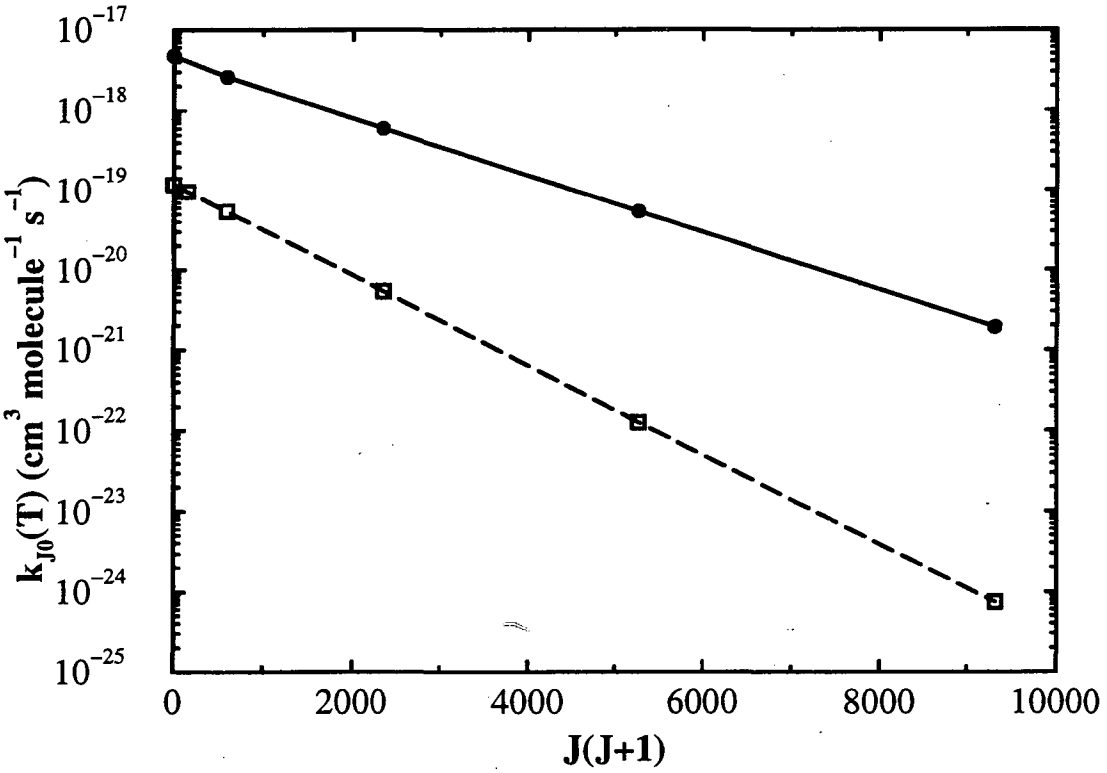

Figure 4.12: The partial rate constant $k_{JK}(T)$, within the helicity conserving approximation, vs. $J(J+1)$ for $K = 0$. Results for T = 400 K (solid line with circles) and T = 250 K (dashed line with squares are shown.

rate constant is within 2% of the final result after 14 iterations and within 1% after 18 iterations.

Results from helicity conserving calculations are presented in Figures 4.12 and 4.13. The HC rate constants for $K = 0$ are plotted as a function of $J(J+1)$ on a semilog plot in Fig. 4.12 for T = 250 and 400 K. At both temperatures a straight line is obtained. Fig. 4.13 shows the CS rate constant as a function of K^2 for fixed J. Results are shown for T = 250 K with $J = 24$ and T = 400 K with $J = 24$ and 48. As shown on a semilog plot, $k_{JK}(T)$ vs. K^2 is nonlinear but can be reasonably well approximated as a straight line. Note that for T = 400 K, the slope of the line is independent of J.

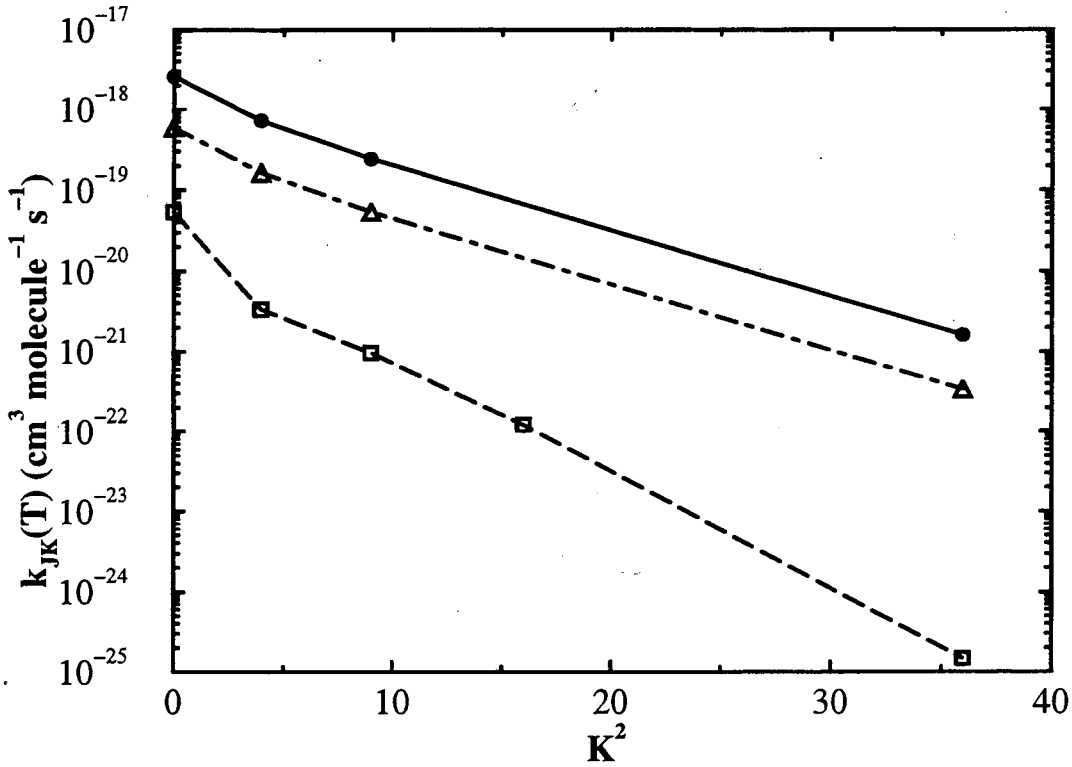

Figure 4.13: The partial rate constant $k_{JK}(T)$, within the helicity conserving approximation, vs. K^2 for fixed J. Results are shown for T = 400 K with $J = 24$ (solid line with circles) and $J = 48$ (dot-dashed line with triangles) and T = 250 K with $J = 24$ (dashed line with squares).

These results can be interpreted in terms of the above discussion on the J-shifting and helicity conserving approximations. In principle one needs to calculate $k_{JK}(T)$ within the CS approximation for all J and K which contribute. However, if the dependence of the rate on J and K is smooth, interpolation between the calculated values can be used to give the total rate constant. In that sense a rough "interpolation" can be made by assuming $\ln k_{JK}(T) = -\alpha J(J+1)$ and $\ln k_{JK}(T) = -\eta K^2$ (*i.e.*, fitting the curves as straight lines). This is equivalent to the J-shifting approximation (for fixed temperature) as discussed above and is tantamount to extracting "effective" moments of inertia. (We refer to rate constants obtained by this procedure as CS "Adjusted.") Doing this we obtain at $I_B = 4.73 \times 10^5$ a.u. and $I_A = 1.96 \times 10^3$ a.u.

	k(T)	
Temp. (K)	J-shifting	CS "Adjusted"[a]
200	9.8(-18)[b]	
250	1.0(-16)	1.2(-16)
300	5.8(-16)	
350	2.0(-15)	
400	7.1(-15)	7.7(-15)
500	3.7(-14)	
600	1.0(-13)	
700	2.8(-13)	

[a]See Section text.
[b]The number in parentheses is the power of 10.

Table 4.4: Total thermal rate constants within the J-shifting and Centrifugal Sudden approximations compared for the three-dimensional O + HCl reaction in units of cm^3 $molecule^{-1}$ s^{-1}

at T = 400 K and $I_B = 4.96 \times 10^5$ a.u. and $I_A = 1.86 \times 10^3$ a.u. at T = 250 K. This indicates that the moments of inertia do not depend strongly on temperature. In addition, these values are in reasonable agreement with those obtained by Koizumi *et al.*[179] from the transition state geometry. The change in the value of the rate constant is 20% at T = 250 K and 8% at T = 400 K. (See Table 4.4.)

Figure 4.14 presents an Arrhenius plot of the calculated rate constant as compared to the results of Koizumi *et al.* and experiment.[186,190] The present results are larger than both the experimental and previous theoretical rates at all temperatures. Unfortunately, since the thermal rate constant is a highly averaged quantity, it is not possible to extract a particular feature of the potential energy surface to hold accountable for the discrepancy. With regard to experiment, if the barrier height were raised only $\sim$ 0.8 - 1.0 kcal/mole — recall that the *ab initio* value of the barrier was scaled from 18.8 to 8.5 kcal/mole in the KSG potential energy surface — then our calculated rates would be in much better agreement with experiment. The lack of agreement between our results and Koizumi *et al.*'s is harder to understand. At present we have no explanation for this. We note that the rate constants calculated by Moribayashi and Nakamura[194] for the initial HCl rotational states $j = 0, 1, 2$ —

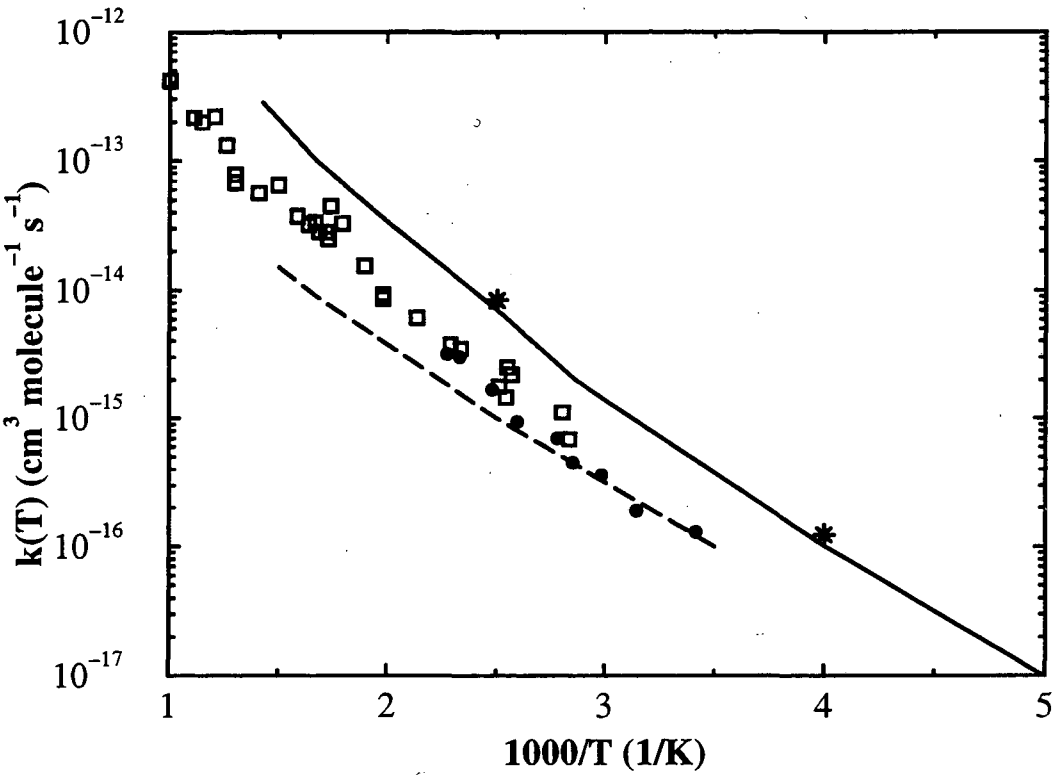

Figure 4.14: Arrhenius plot of calculated and experimental thermal rate constants. The present calculations are shown as a solid line and the results of Koizumi *et al.* as a dashed line. The experimental results of Brown and Smith (Ref. 186) are shown as open circles and that of Mahamud *et al.* (Ref. 190) as filled squares.

though not directly comparable to the present results since they are not fully Boltzmann averaged over all initial states — are also larger than the rates of Koizumi *et al.* (though smaller than ours). Moribayashi and Nakamura also suggest that higher j states ($j > 2$) may contribute even more significantly to the rate and if so, then their fully Boltzmann averaged rate constant would be even larger.

We note that in Fig. 4.14 the present results show indicate that the slope of $\ln k(T)$ vs. $1/T$ increases with increasing temperature. This is also observed in the rates obtained by Koizumi *et al.* as well as in the experimental results shown here. In fact the activation energy reported by Brown and Smith over the temperature range 293-440 K is 5.9 kcal/mole,[186] while a value of 7.3 kcal/mole is obtained by a

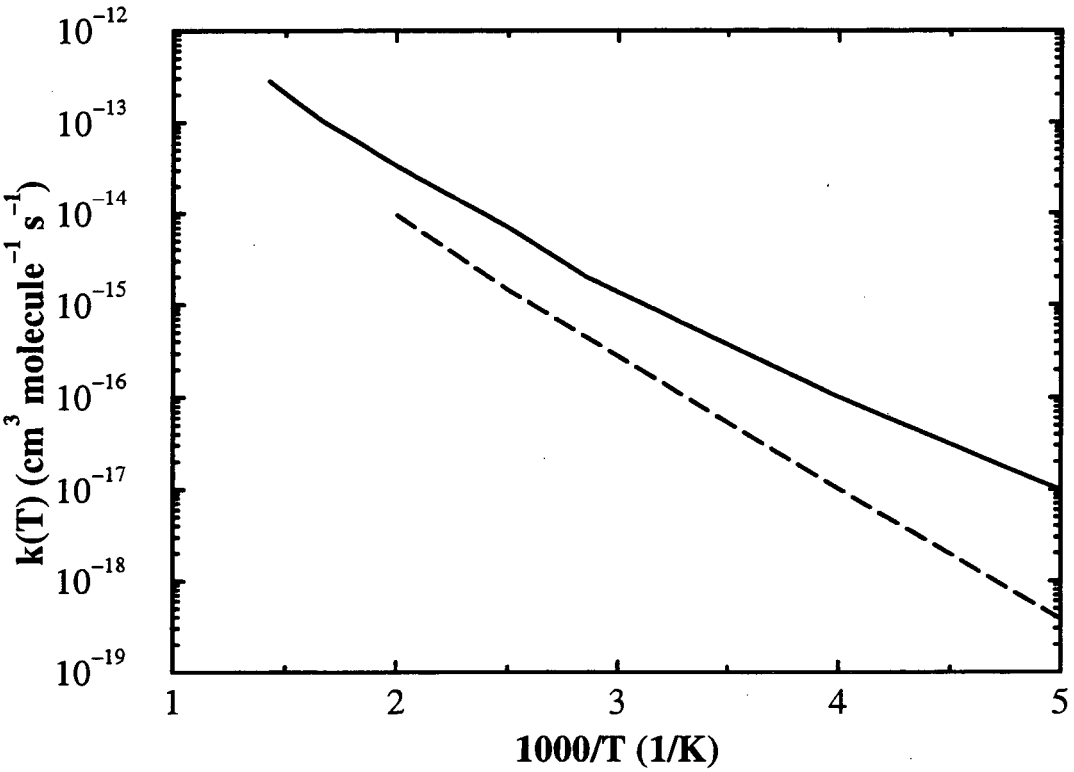

Figure 4.15: Calculated thermal rate constants, $k(T)$ vs. $1000/T$ for the O + HCl (solid line) and O + DCl (dashed line) reactions.

least squares fit of the data of Mahamud, Kim, and Fontijn[190] over the range 353-1486 K. Indeed, the results of Mahamud *et al.* show a non-Arrhenius increase in the activation energy as the temperature is raised. Our results give an activation energy of 5.7 kcal/mole over the range of 200-700 K as compared to about 5.0 kcal/mole from the results of Koizumi *et al.* over 285-667 K. Thus the theoretically calculated activation energies are lower than those obtained by experiment though the correct non-Arrhenius behavior is reproduced.

We have also performed calculations for the thermal rate constant of the O + DCl reaction. These are compared to the results for the O + HCl reaction in Figure 4.15. The deuterated rate constants were obtained by using the same basis set at a given temperature as was needed for the O + HCl reaction. The most interesting

result here is the tunneling enhancement of the rate when H is substituted for D. While the thermal rate constants for the reaction with DCl follow an Arrhenius form (*i.e.*, $\ln k(T)$ vs. $1/T$ is a straight line with the slope equal to the activation energy), with HCl the activation energy becomes smaller as the temperature is lowered. This change in the activation energy at lower temperatures can be attributed to the tunneling of the H atom. In the deuterated case the tunneling rate is reduced due to the heavier mass and the rate therefore remains Arrhenius at low temperature. Indeed, the activation energy for the O + DCl reaction is 6.7 kcal/mole, larger than that for O + HCl. Experimental measurements of Brown and Smith found the ratio of the rate constants k_{O+HCl}/k_{O+DCl} at T = 400 K as 2.4 $\pm$ 0.7.[187] This is smaller by a factor of two than the ratio of 4.8 obtained in the present calculations.

4.4 Concluding Remarks

A method for *directly* calculating thermal rate constants for chemical reactions by means of the flux-position and flux-flux correlation functions has been presented. The key to these methods is taking advantage of the low rank of the Boltzmannized flux operator, Eq. (4.30), to efficiently evaluate the required quantum mechanical trace. If the flux dividing surface is placed at the saddle point of the potential, this operator has a rank approximately equal to twice the number of thermally accessible states of the activated complex. It is in this context that these methods contain the spirit of transition state theory.

In the case of the flux-position correlation function, the Lanczos algorithm is used to find only the nonzero eigenvalues of the entire operator in the trace, Eq. (4.41). The propagation in complex time, $t_c = t - i\hbar\beta/2$ is carried out by a Chebychev polynomial expansion. The correlation function only needs to be calculated at a single (long) time. We have presented applications to the model one-dimensional Eckart barrier and two dimensional collinear H + H_2 reaction as well as the three-dimensional D + H_2 reaction for total angular momentum, $J = 0$. These examples illustrate the efficiency and accuracy of this approach.

The flux-flux autocorrelation function calculation has three main features:

(1) The low rank of the Boltzmannized flux operator is used to advantage in evaluating the quantum mechanical trace. An iterative Lanczos scheme is used to obtain the eigenfunctions of $\hat{F}(\beta)$ corresponding to the largest (in absolute value) eigenvalues and the trace is evaluated in this (much smaller) basis. (2) Absorbing potentials are used in the (real) time propagation to prevent reflection from the edge of the finite basis (here a DVR grid) making the method stable and thereby allowing the size of the basis to be reduced. (3) A split-operator algorithm is used for both the real and imaginary time propagation. For the real time propagation, this produces the time correlation function at all intermediate times necessary to perform the integral of $C_{ff}(t)$ at no additional computational effort.

The absorbing potentials in the flux-flux correlation function make it a more efficient and stable method than that using the flux-position function.

Application to the D + H_2 and O + HCl reactions indicate the applicability of the method to a large range of systems. The rank of the Boltzmannized flux operator is seen to be small ($\sim$ 12-24) and to depend weakly on the temperature and the size of the full basis set. This is in accord with the interpretation of these eigenvalues as related to the states of the activated complex. The real time propagation needed to obtain the correlation function need only be carried out for short times (on the order of $\hbar\beta$ for direct reactions). The advantages of this method make it applicable to a large range of molecular systems, including those with several atoms (> 3).

4.5 Appendix I: A Quantum Mechanical Transition State Theory

As discussed in Section 4.1, there is no unique quantum mechanical transition state theory (QMTST). Indeed, quantum "transition state theories" run the gamut from fully exact to very approximate. The exact methods presented in this Chapter could, in some sense, be called QMTSTs as they only follow the dynamics in a region about the transition state. However, Miller has previously proposed a convincing quantum mechanical *analogy* to classical transition state theory.[143] Section 4.2

discussed the connection between the classical characteristic function, $\chi(\mathbf{p},\mathbf{q})$, and the quantum mechanical projection operator $\hat{\wp}$. The classical TST assumption can be expressed by replacing the characteristic function by a step function, $h(p_s)$, where p_s is the momentum perpendicular to the flux dividing surface. This amounts to a zero time approximation to the characteristic function. Miller suggested that a quantum mechanical TST could be obtained in the same spirit by taking $\hat{\wp} \rightarrow h(\hat{p}_s)$.[143] This, also, is a zero time approximation. (See Eq. (4.20.)

The approximate thermal rate constant is then given by

$$k_{QMTST}(T) = \frac{1}{Q_r}\mathrm{tr}[h(\hat{p}_s)e^{-\beta\hat{H}/2}\hat{F}e^{-\beta\hat{H}/2}h(\hat{p}_s)]. \tag{4.76}$$

(Note that there is some ambiguity in how the operators in the trace should be ordered since $\hat{\wp}$ commutes with the Hamiltonian but $h(\hat{p}_s)$ does not. We have simply taken the correlation function in Eq. (4.20) at zero time.) This rate can be obtained by diagonalizing the operand of the trace using the Lanczos scheme described in the Chapter.

Note that just as in the case of classical transition state theory, Eq. (4.76) represents zero time dynamics, *i.e.*, the quantum mechanical transition state rate is the *instantaneous* flux through the dividing surface in the reactive direction. [We note that the projection operator involving the step function in position gives the rate constant as zero at $t \rightarrow 0$. It is clear that not all projection operators are created equal, particularly in the zero time limit.] As a practical point, we note that this approximation represents a significant computational savings in that one now only has to carry out a propagation in pure imaginary time (to evaluate the Boltzmann average)

In order to implement Eq. 4.76 we need the matrix elements of $h(\hat{p})$ in the sinc-function DVR. To accomplish this we begin by noting that the sinc-function DVR basis functions in the momentum representation are given by[74]

$$\phi_j(p) = \langle p|j\rangle = \sqrt{\frac{\hbar}{2p_{max}}}\, e^{-i\pi jp/p_{max}}, \quad |p| \leq p_{max} \tag{4.77}$$

where $\phi_j(p) = 0$ for $|p| > p_{max}$. We need to evaluate the matrix element of $h(\hat{p})$ in

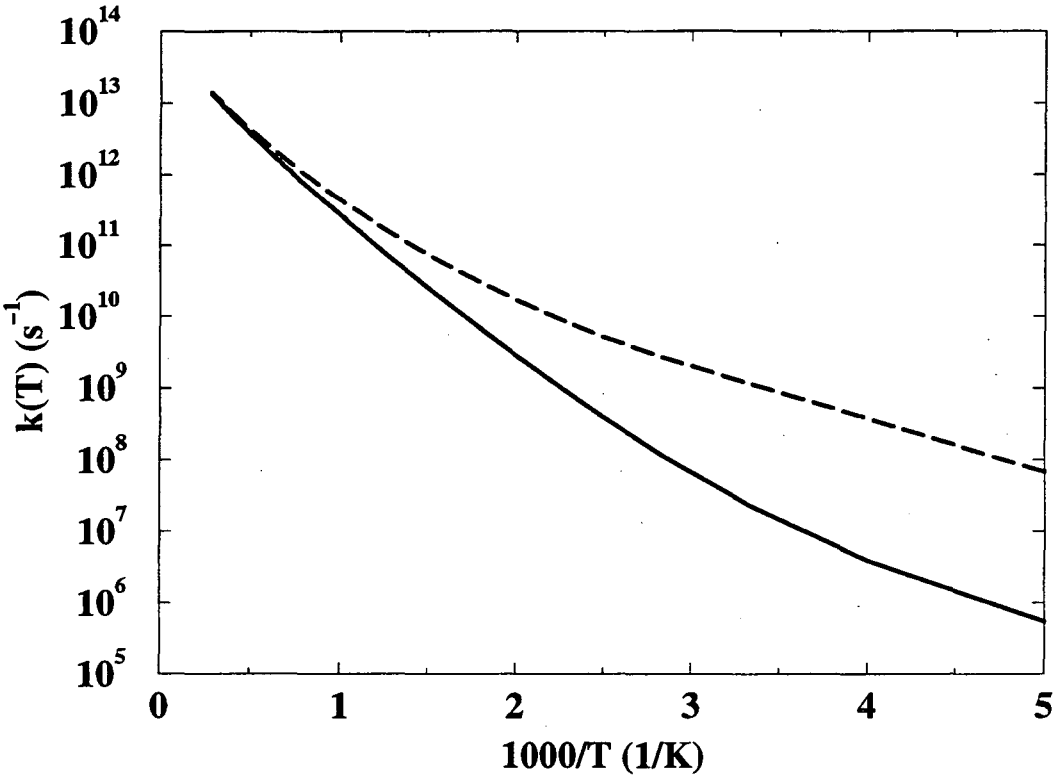

Figure 4.16: Arrhenius plot of the thermal rate constant, $k(T)$ vs. $1000/T$, calculated using the quantum mechanical analogue to transition state theory. The dashed line is the QMTST result and the solid line is the exact rate constant.

this basis. This gives

$$\begin{aligned} \langle j|h(\hat{p})|j'\rangle &= \int_{-\infty}^{\infty} \frac{dp}{\hbar} \langle j|p\rangle\, h(\hat{p})\, \langle p|j'\rangle \\ &= \frac{1}{2p_{max}} \int_0^{p_{max}} dp\; e^{i(j-j')\pi p/p_{max}}. \end{aligned} \tag{4.78}$$

The diagonal matrix elements for which $j = j'$ can immediately be identified as

$$\langle j|h(\hat{p})|j\rangle = \frac{1}{2}. \tag{4.79}$$

Integrating for $j \neq j'$ gives

$$\langle j|h(\hat{p})|j'\rangle = \frac{1}{2p_{max}} \left\{ \frac{p_{max}}{i(j-j')\pi} \left[e^{i(j-j')\pi} - 1\right] \right\} \tag{4.80}$$

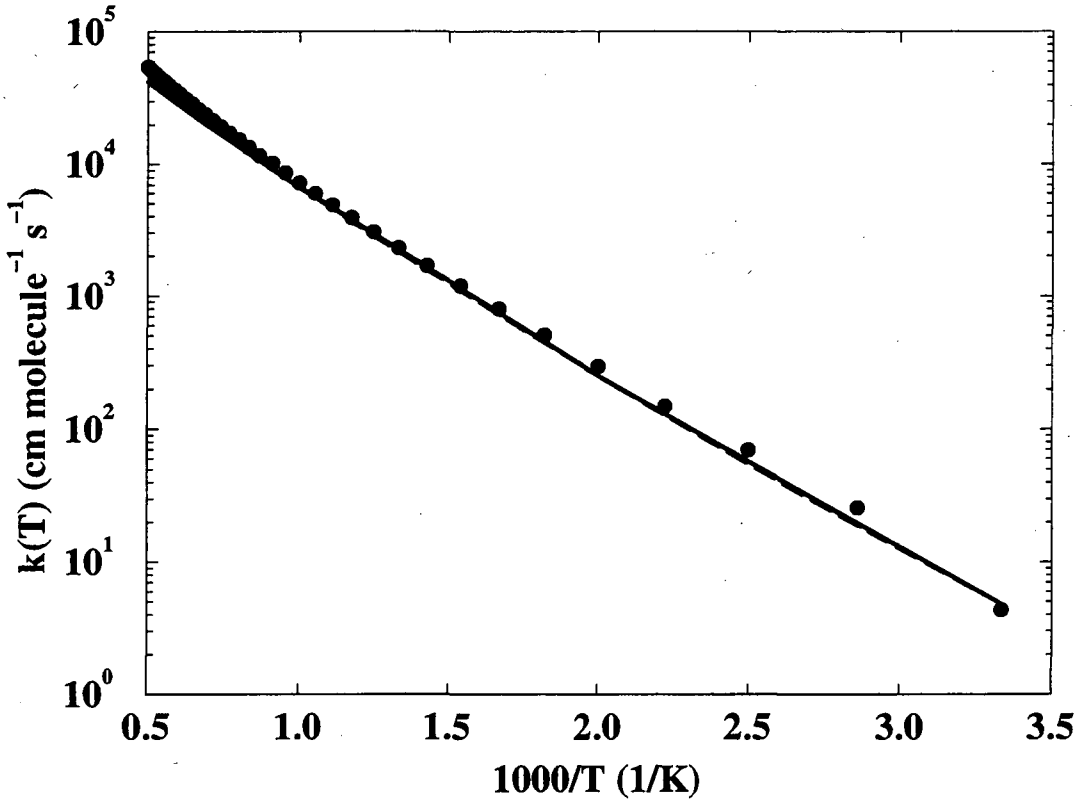

Figure 4.17: Arrhenius plot of the thermal rate constant, $k(T)$ vs. $1000/T$, for the collinear H + H_2 reaction calculated using the quantum mechanical analogue to transition state theory. The QMTST rates are shown as as solid circles, the results of Rom *et al.* (Ref. 155) as a solid line, and the results of Brown and Light (Ref. 161) as a dashed line.

as the result for the off-diagonal matrix elements. In some cases, one is interested in the matrix elements of $h(-\hat{p})$; the diagonal elements are the same and the off-diagonal elements differ by a minus sign.

We have applied this method to the Eckart barrier, the collinear H + H_2 reaction, and the three-dimensional D + H_2 reaction. The details of the calculations for these systems are given in the main text of the Chapter.

Figure 4.16 shows the Arrhenius plot of the rate constant calculated by the QMTST method compared to the exact result. The QMTST method does not reproduce the exact rate constant except at high temperatures. The transition state

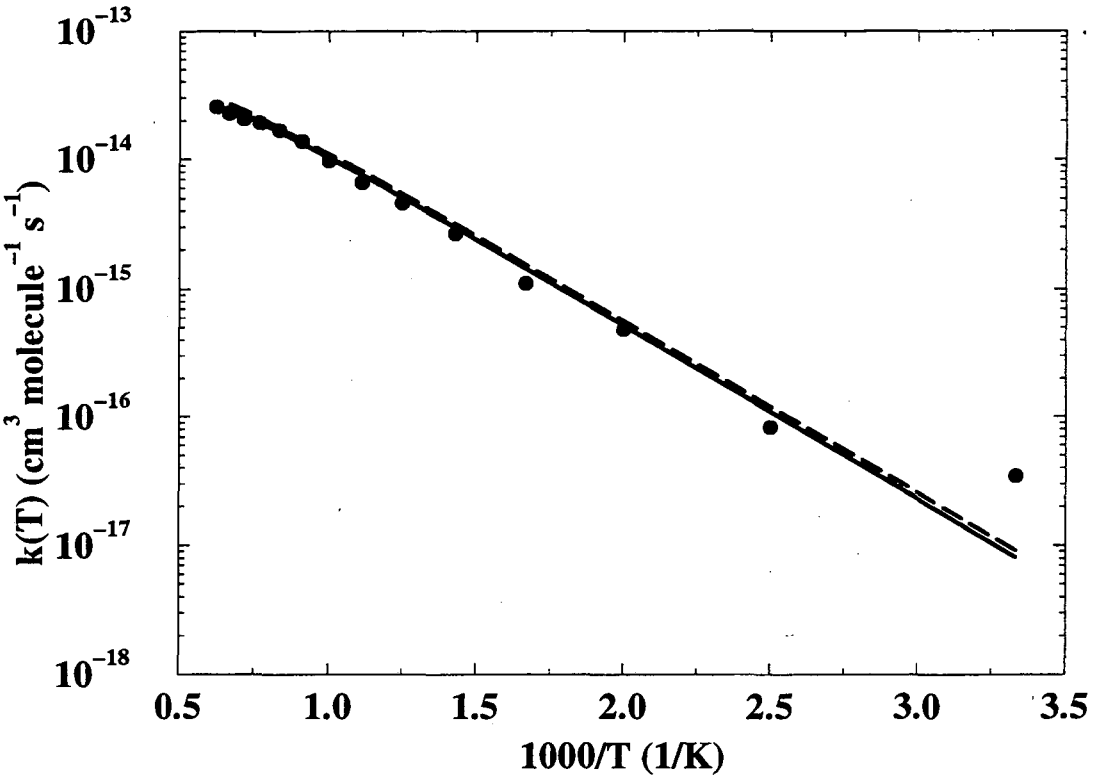

Figure 4.18: Arrhenius plot of the thermal rate constant, $k(T)$ vs. $1000/T$, calculated using the quantum mechanical analogue to transition state theory. The QMTST rates are shown as as solid circles, the results of Mielke *et al.* (Ref. 178) as a solid line, and the results of Park and Light (Ref. 161) as a dashed line.

theory approximation gives rate constants about two orders of magnitude too large at 200 K. However, for higher temperatures, the error decreases and is below 20% above 1700 K, and below 10% above 2400 K. We note that the TST rate, in this case, is an upper bound to the true rate. We also find that varying the position of the dividing surface shows that locating it at the top of the barrier gives the lowest TST rate at all temperatures.

Figure 4.17 shows a similar Arrhenius plot for the QMTST rate for the collinear H + H_2 reaction, compared to the results of Rom *et al.*[155] and Brown and Light.[47] In this case, the transition state theory result is in good agreement with the flux-position results over the entire temperature range. The largest error due to the

transition state theory approximation is 40% (at the lower temperatures) and the error is less than 15% above 400 K.

Finally, Figure 4.18 is an Arrhenius plot showing the present QMTST rate constants for the three-dimensional D + H_2 reaction (for total angular momentum, $J = 0$) with those calculated by Mielke *et al.*[178] and Park and Light.[161] The transition state theory approximation is in good agreement with the flux-position correlation function results at all temperatures except 300 K. The approximate rate overestimates the rate at 300 K by a factor of 4.

The results for this quantum mechanical analogue to classical transition state theory are mixed in nature. For the multidimensional examples (the collinear H + H_2 and D + H_2) the agreement with exact calculations is quite reasonable except at the lowest temperatures. For the one-dimensional Eckart barrier, on the other hand, the agreement is poor at all temperatures below about 1700 K. This may indicate that while this approximate method properly represents the nonseparability of the multidimensional cases, it is not properly describing the rate due to tunneling through the barrier. This would account for the inaccuracy at low temperatures for the multidimensional reactions as well as that for the Eckart barrier. The Eckart barrier height in this example is 0.425 eV; even at moderately high temperatures, tunneling will account for a significant portion of the rate constant.

Chapter 5

Concluding Remarks

5.1 Summary

In this work we have presented several methods for describing quantum reaction dynamics at differing levels of detail. As discussed in Chapter 1, it is imperative that advances in theoretical methods be made if the range of systems amenable to a quantum mechanical treatment is to be extended to more than three or four atoms. Clearly though, one cannot get something for nothing. How is it then, that more efficient methods can be developed? This has been achieved by two main approaches: (1) The quantity of interest is directly calculated, and (2) the physics involved in the chemical reaction is used to advantage. The first point is clear: one should not have to calculate quantitities which contain more detail than is desired, no more than an experimentalist should have to put in a laser to measure product state distributions, say, which are not of interest. Much of the effort expended in the calculation of these more detailed quantitities will be washed out in the subsequent averaging. The second point is more ill-defined, but we have presented here a couple of examples.

One example involves the state-to-state and initial state-selected reaction probabilities described in Chapter 2. While the absorbing boundary conditions enable the direct calculation of the desired quantitity, the intial state-selected calculation is more efficient than the state-to-state. The reason is that reactivity is determined in a smaller region about the transition state than the product state-selection (allowing

the size of the necessary basis to be reduced). This is a well-known property of gas phase chemical reactions.

Another example is the direct calculation of thermal rate constants presented in Chapter 4. Today, it is still common to obtain rate constants by first calculating the entire S-matrix and then averaging away all the hard earned detail. A simple (but possibly overstated) analogy to this practice is to estimate the number of cars crossing the Bay Bridge into San Francisco in a day by monitoring every car within driving distance to determine if it crosses the bridge or not. On the other hand, the *direct* way to obtain the same result is to sit at the toll plaza and count the cars as they pass. This is the spirit of the present methods for calculating the rate constant for a chemical reaction.

The flux correlation function approach requires the evaluation of a quantum mechanical trace. A straightforward computation of this in a basis of size N would require $2N$ applications of the propagator in complex time, $t_c = t - i\hbar\beta/2$. Alternatively, one can evaluate the trace in a basis of the eigenstates of the Hamiltonian. The correlation function is then easily obtained but first one must diagonalize an $N \times N$ matrix. The present methods take advantage of the low rank of the Boltzmannized flux operator in Eq. (4.30). This operator has a rank approximately equal to twice the number of states of the "activated complex" that are thermally accessible. These methods heed the lesson of transition state theory by concentrating on determining the contribution of each state of the activated complex to the rate. The number of states of the activated complex is usually less than the number of asymptotic reactant or product open channels. Indeed, we have found the rank of the Boltzmannized flux operator, M, is on the order of ten or twenty even for basis sets where N is several thousand. The effort involved in these methods is approximately $2M$ applications of the propagator in complex time (though somewhat less than this for the flux-flux correlation function since only one real time propagation is required).

We have also shown, in Chapter 3, how the photodetachment spectrum can be obtained using the absorbing boundary conditions Green's function. Photodetachment spectroscopy of a stable anion ABC^- can yield information about the neutral scattering surface of ABC. In such cases where the anion geometry is close to that

of the neutral transition state, it is often called transition state spectroscopy. Both total and arrangement-selected intensities can be obtained simultaneously. In addition, the spectrum for a large range of energies can be calculated at one time with the multiply-shifted quasi-minimal residual method.[132] The photodetachment spectra for H_3O^- has been calculated in reduced dimensionality (four degrees of freedom treated explicitly). When compared with experiment,[15] the theoretical spectra indicate that the WDSE potential energy surface[90,102] has incorrect equilibrium bending angles and a barrier that is too "late." However, since the the anion equilibrium geometries (there are two local minima on the surface) are not the same as the neutral saddle point, no direct information about the transition state is obtained.

5.2 Prognosis for the Future

5.2.1 The Present Methods

A few comments are in order here concerning the more immediate possible improvements in the methods presented here.

Transition state spectroscopy is a powerful tool for probing potential energy surfaces of scattering systems. However, it is not applicable to every system but can only be applied to systems with a stable anion with an equilibrium geometry close to that of the transition state of the neutral. In addition, if spectrum is not insensitive to the anion potential and the potential is not well characterized, the interpretation of the result in terms of the features of the neutral potential cannot be definitive and is much more subtle. With these caveats, transition state spectroscopy should continue to provide useful information for scattering systems. One additional note: the present calculations give the total and arrangement-selected intensities for the same effort. It seems one ought to be able to obtain the more detailed quantity more cheaply.

The method for direct calculation of thermal rate constants from the flux-flux correlation function, described in Chapter 4, provides hope for accurately treating large ($>$ 3 or 4 atoms) in the near future. There are, however areas in which some

improvement can be sought. Some of these involve minor, computational issues, such as using the Chebychev polynomial expansion to apply the Boltzmann operator (since the imaginary propagation time is fixed). One approach to the calculation (similar to the method of Manthe[167]) could be to diagonalize the Boltzmann operator for one value of β, call it β_0, corresponding to a high temperature (low β),

$$e^{-\beta_0 \hat{H}/2}\, \hat{F}\, e^{-\beta_0 \hat{H}/2}\, |n\rangle = f_n |n\rangle. \tag{5.1}$$

The rate for an arbitrary, lower temperature can then be obtained, after propagating these eigenstates, as

$$k(T) = \frac{1}{Q_r(T)} \int_0^\infty \langle n(t)|\, e^{-\Delta\beta \hat{H}/2} \hat{F} e^{-\Delta\beta \hat{H}/2}\, |n(t)\rangle. \tag{5.2}$$

Thus, the diagonalization and propagation only needs to be carried out once. However, a potential drawback is the higher rank of the Boltzmannized flux operator than is necessary at the lower temperatures (though Figure 4.6 is encouraging on that score). Such a method has not yet been tested.

5.2.2 General Comments

The field of gas phase reaction dynamics can be regarded as a mature field. Much progess has been made over the last 30 or 40 years in both theoretical and experimental methods. Theoretically, for example, atom-diatom reactions have now largely been rendered amenable to quantum mechanical calculations. However, much remains to be done in treating larger and more complicated systems as well as applying the current understanding to condensed phase systems. Ubiquitous in chemical dynamics is the case of a few strongly coupled degrees of freedom weakly linked to a few or many more degrees of freedom (a bath). This can occur in gas phase reactions involving a relatively large molecule (even in the case of H + H_2O, the OH bond is only very weakly coupled to the reacting degrees of freedom) or in reactions (and spectroscopy) taking place in solution, in a cluster, or on a surface.

One approach to treating such systems, which we have made use of in Chapters 2 and 3, is reduced dimensionality methods. Only the few degrees of freedom

which take part in the reaction or are strongly coupled are treated explicitly while the remaining coordinates are held fixed. The neglected degrees of freedom can be included approximately by adding their adiabatic energies to the potential[109,196] or by cruder methods of including the effect of their zero point energy at the barrier, say.[75] These methods have the advantage that the calculation only treats a few coordinates and in many cases (such as the H + H_2O reaction[75–78,141,166] and the D + H_2 reaction[56]) are quite accurate. However, one needs to know which degrees of freedom to neglect and these methods are not suited to cases where the these neglected degrees of freedom have a significant and interesting effect (such as condensed phase environments).

A highly promising methodology involves treating the "interesting" coordinates quantum mechanically while describing the remaining degrees of freedom using classical or semiclassical mechanics.[91–93,165,197–202] While this may eventually become the standard approach for treating large systems, there are still some questions which have not been answered.[202,203] One of the crucial issues is the interaction between the quantum mechanical system and the classical (or semiclassical) bath. A general procedure for carrying out the dynamics with consistent interactions between the system and bath has yet to appear. Of note is the work by Sun and Miller[204] on a mixed semiclassical-classical method in which classical trajectories are run including all the degrees of freedom, but the semiclassical phase information is only kept for the system coordinates.

The flux-flux correlation function method presented in Chapter 4 for directly calculating thermal rate constants holds promise for such mixed quantum-classical and quantum-semiclassical approaches. Such an idea has already been implemented by two groups,[91,165] but these methods have not taken advantage of the low rank of the Boltzmannized flux operator. This should be an exciting direction for future research.

Dynamical approximations are yet another avenue for treating large and small systems. A quantum mechanical theory with the power and amazing usefulness of classical transition state theory remains to be found, if indeed it exists. Other models, with less ambitious goals, would form an important part of the available

repertoire for describing chemical reactions, particularly those with a weak coupling to a bath.

One of the most important issues facing the field of reaction dynamics is the generation of high-quality *ab initio* potential energy surfaces. Accurately describing the nuclear dynamics is not very fruitful if the potential energy surface is in error. On the other hand, the WDSE potential for the OH + H_2 reaction, despite its many flaws, does a reasonably good job of describing the dynamics and allowed the theoretical prediction of the mode specificity.[105] The dynamicist can improve this situation without calculating potential energy surfaces by developing dynamics methods which are amenable to direct *ab initio* calculations. For example, the method for calculating photodetachment intensities described in Chapter 3 can calculate an entire spectrum using a single DVR grid. Thus, a direct *ab initio* calculation of the potential energies of both the anion and the neutral at these grid points is possible. The accuracy and efficiency of such an approach needs to be investigated. Another step in this direction is the development of methods which require the potential only in a small region, such as the thermal rate constant calculations.

The field of gas phase reaction dynamics has an exciting future ahead in the development of new methods and the application of the current knowledge to new and interesting systems.

References

[1] G. C. Schatz and A. Kuppermann, J. Chem. Phys. **65**, 4642 (1976).

[2] G. C. Schatz and A. Kuppermann, J. Chem. Phys. **65**, 4668 (1976).

[3] W. H. Miller, J. Chem. Phys. **50**, 407 (1969).

[4] M. E. Rose, *Elementary Theory of Angular Momentum* (John Wiley & Sons, Inc., New York, 1957).

[5] R. N. Zare, *Angular Momentum* (John Wiley & Sons, Inc., New York, 1988).

[6] W. Kohn, Phys. Rev. **74**, 1763 (1948).

[7] W. H. Miller and B. M. D. D. Jansen op de Haar, J. Chem. Phys. **86**, 6213 (1987).

[8] J. Z. H. Zhang, S.-I. Chu, and W. H. Miller, J. Chem. Phys. **88**, 6233 (1988).

[9] T. Seideman and W. H. Miller, J. Chem. Phys. **96**, 4412 (1992).

[10] T. Seideman and W. H. Miller, J. Chem. Phys. **97**, 2499 (1992).

[11] W. H. Miller and T. Seideman, in *Time Dependent Quantum Molecular Dynamics: Experiment and Theory*, edited by J. Broeckhove (NATO, ARW, 1992).

[12] U. Manthe and W. H. Miller, J. Chem. Phys. **99**, 3411 (1993).

[13] R. B. Metz, S. E. Bradforth, and D. M. Neumark, Adv. Chem. Phys. **81**, 1 (1992).

[14] D. M. Neumark, Acc. Chem. Res. **26**, 33 (1993).

[15] E. de Beer, E. H. Kim, D. M. Neumark, R. F. Gunion, and W. C. Lineberger, J. Phys. Chem. **99**, 13627 (1995).

[16] J. R. Taylor, *Scattering Theory* (John Wiley & Sons, Inc., New York, 1972).

[17] J. J. Sakurai, *Modern Quantum Mechanics* (Addison-Wesley, New York, 1985), pp. 379-448.

[18] A. Messiah, *Quantum Mechanics* (John Wiley & Sons, Inc., New York, 1966), Vol. II, pp. 801-872.

[19] G. Barton, *Elements of Green's Functions and Propagation* (Oxford University Press, New York, 1989).

[20] Prof. W. H. Miller, class notes, Chemistry 223B, Spring 1996, University of California at Berkeley.

[21] D. O. Harris, G. G. Engerholm, and W. D. Gwinn, J. Chem. Phys. **43**, 1515 (1965).

[22] A. S. Dickinson and P. R. Certain, J. Chem. Phys. **49**, 4209 (1968).

[23] R. Meyer, J. Chem. Phys. **52**, 2053 (1970).

[24] C. C. Marston and G. G. Balint-Kurti, J. Chem. Phys. **91**, 3571 (1989).

[25] J. T. Muckerman, Chem. Phys. Lett. **173**, 200 (1990).

[26] C. Leforestier, J. Chem. Phys. **94**, 6388 (1991).

[27] C. Leforestier, J. Chem. Phys. **101**, 7357 (1994).

[28] G. C. Corey and D. Lemoine, J. Chem. Phys. **97**, 4115 (1992).

[29] J. A. Bentley, R. E. Wyatt, M. Menou, and C. Leforestier, J. Chem. Phys. **97**, 4255 (1992).

[30] R. A. Friesner, Chem. Phys. Lett. **116**, 39 (1985).

[31] R. A. Friesner, J. Chem. Phys. **85**, 1462 (1986).

[32] R. A. Friesner, J. Chem. Phys. **86**, 3522 (1987).

[33] R. Kosloff, NATO ASI Ser. C **412**, 175 (1993).

[34] W. Yang and A. C. Peet, Chem. Phys. Lett. **153**, 98 (1988).

[35] A. C. Peet and W. Yang, J. Chem. Phys. **91**, 6598 (1989).

[36] J. Echave and D. C. Clary, Chem. Phys. Lett. **190**, 225 (1992).

[37] D. T. Colbert and W. H. Miller, J. Chem. Phys. **96**, 1982 (1992).

[38] J. V. Lill, G. A. Parker, and J. C. Light, Chem. Phys. Lett. **89**, 483 (1982).

[39] J. C. Light, I. P. Hamilton, and J. V. Lill, J. Chem. Phys. **82**, 1400 (1985).

[40] R. M. Whitnell and J. C. Light, J. Chem. Phys. **89**, 3674 (1988).

[41] A. Goldberg and B. W. Shore, J. Phys. B **11**, 3339 (1978).

[42] C. Leforestier and R. E. Wyatt, J. Chem. Phys. **78**, 2334 (1983).

[43] R. Kosloff and D. Kosloff, J. Comput. Phys. **63**, 363 (1986).

[44] D. Neuhauser and M. Baer, J. Chem. Phys. **90**, 4351 (1989).

[45] D. Neuhauser and M. Baer, J. Chem. Phys. **91**, 4651 (1989).

[46] D. Neuhauser, M. Baer, and D. J. Kouri, J. Chem. Phys. **93**, 2499 (1990).

[47] D. Brown and J. C. Light, J. Chem. Phys. **97**, 5465 (1992).

[48] G. Jolicard and E. J. Austin, Chem. Phys. Lett. **121**, 106 (1985).

[49] G. Jolicard and E. J. Austin, Chem. Phys. **103**, 295 (1986).

[50] G. Jolicard and M. Y. Perrin, Chem. Phys. **116**, 1 (1987).

[51] G. Jolicard, C. Leforestier, and E. J. Austin, J. Chem. Phys. **88**, 1026 (1988).

[52] I. Last, D. Neuhauser, and M. Baer, J. Chem. Phys. **96**, 2017 (1992).

[53] I. Last and M. Baer, Chem. Phys. Lett. **189**, 84 (1992).

[54] I. Last, A. Baram, and M. Baer, Chem. Phys. Lett. **195**, 435 (1992).

[55] I. Last, A. Baram, H. Szichman, and M. Baer, J. Phys. Chem. **97**, 7040 (1993).

[56] D. Wang and J. M. Bowman, J. Phys. Chem. **98**, 7994 (1994), and references therein.

[57] R. C. Mayrhofer and J. M. Bowman, J. Chem. Phys. **100**, 7229 (1994).

[58] W. H. Miller, S. D. Schwartz, and J. W. Tromp, J. Chem. Phys. **79**, 4889 (1983).

[59] S. M. Auerbach and W. H. Miller, J. Chem. Phys. **98**, 6917 (1993).

[60] C. Leforestier and W. H. Miller, J. Chem. Phys. **100**, 733 (1994).

[61] U. Manthe, T. Seideman, and W. H. Miller, J. Chem. Phys. **99**, 10078 (1993).

[62] U. Manthe, T. Seideman, and W. H. Miller, J. Chem. Phys. **101**, 4759 (1994).

[63] J. D. Gezelter and W. H. Miller, J. Chem. Phys. **103**, 7868 (1995).

[64] P. Saalfrank and W. H. Miller, J. Chem. Phys. **98**, 9040 (1993).

[65] P. Saalfrank and W. H. Miller, Surf. Sci. **303**, 206 (1994).

[66] D. G. Truhlar and C. J. Horowitz, J. Chem. Phys. **68**, 2566 (1978).

[67] D. G. Truhlar and C. J. Horowitz, J. Chem. Phys. **71**, 1514 (1979).

[68] P. Siegbahn and B. Liu, J. Chem. Phys. **68**, 2457 (1978).

[69] D. K. Bondi and J. N. L. Connor, J. Chem. Phys. **82**, 4383 (1985).

[70] L. M. Hubbard, S. Shi, and W. H. Miller, J. Chem. Phys. **78**, 2381 (1983).

[71] B. R. Johnson, Chem. Phys. Lett. **13**, 172 (1972).

[72] J. Z. H. Zhang and W. H. Miller, J. Chem. Phys. **91**, 1528 (1989).

[73] J. Z. H. Zhang, D. L. Yeager, and W. H. Miller, Chem. Phys. Lett. **173**, 489 (1990).

[74] G. C. Groenenboom and D. T. Colbert, J. Chem. Phys. **99**, 9681 (1993).

[75] D. C. Clary, J. Chem. Phys. **95**, 7298 (1991).

[76] D. C. Clary, Chem. Phys. Lett. **192**, 34 (1992).

[77] D. C. Clary, J. Chem. Phys. **96**, 3656 (1992).

[78] G. Nyman and D. C. Clary, J. Chem. Phys. **99**, 7774 (1993).

[79] J. Echave and D. C. Clary, J. Chem. Phys. **100**, 402 (1994).

[80] J. M. Bowman and D. Wang, J. Chem. Phys. **96**, 7852 (1992).

[81] D. Wang and J. M. Bowman, J. Chem. Phys **96**, 8906 (1992).

[82] D. Wang and J. M. Bowman, J. Chem. Phys. **98**, 6235 (1993).

[83] H. Szichman, I. Last, A. Baram, and M. Baer, J. Phys. Chem. **97**, 6436 (1993).

[84] H. Szichman, I. Last, and M. Baer, J. Phys. Chem. **98**, 828 (1994).

[85] H. Szichman and M. Baer, J. Chem. Phys. **101**, 2081 (1994).

[86] H. Szichman and M. Baer, Chem. Phys. Lett. **242**, 285 (1995).

[87] D. H. Zhang and J. Z. H. Zhang, J. Chem. Phys. **100**, 2697 (1994).

[88] D. H. Zhang and J. Z. H. Zhang, J. Chem. Phys. **101**, 1146 (1994).

[89] D. Neuhauser, J. Chem. Phys. **100**, 9272 (1994).

[90] S. P. Walch and T. H. Dunning, Jr., J. Chem. Phys. **72**, 1303 (1980).

[91] G. Wahnstrom, B. Carmeli, and H. Metiu, J. Chem. Phys. **88**, 2478 (1988).

[92] A. Garcia-Vela, R. B. Gerber, and D. G. Imre, J. Chem. Phys. **97**, 7242 (1992).

[93] A. Garcia-Vela and R. B. Gerber, J. Chem. Phys. **98**, 427 (1993).

[94] S. Keshavamurthy and W. H. Miller, Chem. Phys. Lett. **218**, 189 (1994).

[95] W. H. Thompson and W. H. Miller, Chem. Phys. Lett. **206**, 123 (1993).

[96] S. M. Auerbach and W. H. Miller, J. Chem. Phys. **100**, 1103 (1994).

[97] G. C. Light and J. H. Matsumoto, Chem. Phys. Lett. **58**, 578 (1978).

[98] R. Zellner and W. Steinert, Chem. Phys. Lett. **81**, 568 (1981).

[99] M. H. Mok and J. C. Polanyi, J. Chem. Phys. **53**, 4588 (1970).

[100] B. A. Hodgson and J. C. Polanyi, J. Chem. Phys. **55**, 4745 (1971).

[101] G. P. Glass and B. K. Chaturvedi, J. Chem. Phys. **75**, 2749 (1981).

[102] G. C. Schatz and S. P. Walch, J. Chem. Phys. **72**, 776 (1980).

[103] G. C. Schatz and H. Elgersma, Chem. Phys. Lett. **73**, 21 (1980).

[104] G. C. Schatz, J. Chem. Phys. **74**, 1133 (1981).

[105] G. C. Schatz, M. C. Colton, and J. L. Grant, J. Phys. Chem. **88**, 2971 (1984).

[106] A. Kuppermann, G. C. Schatz, and M. Baer, J. Chem. Phys. **65**, 4596 (1976).

[107] G. C. Schatz and A. Kuppermann, J. Chem. Phys. **65**, 4624 (1976).

[108] J. Palma and J. Echave, J. Chem. Phys. **104**, 2841 (1996).

[109] J. M. Bowman, J. Phys. Chem. **95**, 4960 (1991), and references therein.

[110] D. Wang and J. M. Bowman, J. Chem. Phys. **100**, 1021 (1994).

[111] A. Sinha, J. Phys. Chem. **94**, 4391 (1990).

[112] A. Sinha, M. C. Hsiao, and F. F. Crim, J. Chem. Phys. **92**, 6333 (1990).

[113] A. Sinha, M. C. Hsiao, and F. F. Crim, J. Chem. Phys. **94**, 4928 (1991).

[114] M. C. Hsiao, A. Sinha, and F. F. Crim, J. Phys. Chem. **95**, 8263 (1991).

[115] R. B. Metz, J. D. Thoemke, J. M. Pfeiffer, and F. F. Crim, J. Chem. Phys. **99**, 1744 (1993).

[116] M. J. Bronikowski, W. R. Simpson, B. Girard, and R. N. Zare, J. Chem. Phys. **95**, 8647 (1991).

[117] M. J. Bronikowski, W. R. Simpson, and R. N. Zare, J. Phys. Chem. **97**, 2194 (1993).

[118] M. J. Bronikowski, W. R. Simpson, and R. N. Zare, J. Phys. Chem. **97**, 2204 (1993).

[119] D. E. Adelman, S. V. Filseth, and R. N. Zare, J. Chem. Phys. **98**, 4636 (1993).

[120] M. Alagia, N. Balucani, P. Casavecchia, D. Stranges, and G. G. Volpi, J. Chem. Phys. **98**, 2459 (1993).

[121] M. J. Pilling and P. W. Seakins, *Reaction Kinetics* (Oxford University Press, Oxford, 1995).

[122] S. M. Auerbach and C. Leforestier, Comput. Phys. Commun. **78**, 55 (1993).

[123] B. W. Spath and W. H. Miller, J. Chem. Phys. **104**, 95 (1996).

[124] G. C. Schatz, J. Phys. Chem. **94**, 6157 (1990), and references therein.

[125] D. E. Manolopoulos, K. Stark, H-J. Werner, D. W. Arnold, S. E. Bradforth and D. M. Neumark, Science **262**, 1852 (1993), and references therein.

[126] S. S. Xantheas and T. H. Dunning, Jr., J. of Chinese Chem. Soc. **42**, 241 (1995).

[127] S. L. Mielke, (private communication).

[128] D. C. Clary, J. K. Gregory, M. J. T. Jordan, and E. Kauppi, (in press).

[129] Y. Saad and M. H. Schultz, SIAM J. Sci. Statist. Comput. **7**, 856 (1986).

[130] R. W. Freund and N. M. Nachtigal, Numer. Math. **60**, 315 (1991).

[131] H. O. Karlsson, J. Chem. Phys. **103**, 4914 (1995).

[132] R. W. Freund, in *Numerical Linear Algebra*, edited by L. Reichel, A. Ruttan, and R. Varga (de Gruyter, Berlin, 1993).

[133] C. Lanczos, J. Res. Natl. Bur. Stand. **45**, 255 (1950).

[134] D. H. Zhang and J. Z. H. Zhang, Chem. Phys. Lett. **232**, 370 (1995).

[135] D. H. Zhang, J. Z. H. Zhang, Y. Zhang, D. Wang, and Q. Zhang, J. Chem. Phys. **102**, 7400 (1995).

[136] Y. Zhang, D. Zhang, W. Li, Q. Zhang, D. Wang, D. H. Zhang, and J. Z. H. Zhang, J. Phys. Chem. **99**, 16824 (1995).

[137] W. Zhu, J. Dai, J. Z. H. Zhang, and D. H. Zhang, J. Chem. Phys. **105**, 4881 (1996).

[138] D. H. Zhang and J. C. Light, J. Chem. Phys. **104**, 4544 (1996).

[139] D. H. Zhang and J. C. Light, J. Chem. Phys. **105**, 1291 (1996).

[140] D. H. Zhang and J. Z. H. Zhang, J. Chem. Phys. **103**, 6512 (1995).

[141] W. H. Thompson and W. H. Miller, J. Chem. Phys. **101**, 8620 (1994).

[142] T. Yamamoto, J. Chem. Phys. **33**, 281 (1960).

[143] W. H. Miller, J. Chem. Phys. **61**, 1823 (1974).

[144] R. Jaquet and W. H. Miller, J. Phys. Chem. **89**, 2139 (1985).

[145] K. Yamashita and W. H. Miller, J. Chem. Phys. **82**, 5475 (1985).

[146] J. W. Tromp and W. H. Miller, J. Phys. Chem. **90**, 3482 (1986).

[147] J. W. Tromp and W. H. Miller, Faraday Discuss. Chem. Soc. **84**, 441 (1987).

[148] N. Makri and W. H. Miller, J. Chem. Phys. **90**, 904 (1989).

[149] W. H. Miller, J. Phys. Chem. **99**, 12387 (1995).

[150] G. Wahnstrom and H. Metiu, J. Phys. Chem. **92**, 3240 (1988).

[151] M. Thachuk and G. C. Schatz, J. Chem. Phys. **97**, 7297 (1992).

[152] M. Thachuk, H. R. Mayne, and G. C. Schatz, J. Chem. Phys. **99**, 3516 (1993).

[153] M. Thachuk and G. C. Schatz, J. Chem. Phys. **101**, 6577 (1994).

[154] P. N. Day and D. G. Truhlar, J. Chem. Phys. **94**, 2045 (1991).

[155] N. Rom, N. Moiseyev, and R. Lefebvre, J. Chem. Phys. **96**, 8307 (1992).

[156] R. Lefebvre, V. Ryaboy, and N. Moiseyev, J. Chem. Phys. **98**, 8601 (1993).

[157] V. Ryaboy and R. Lefebvre, J. Chem. Phys. **99**, 9547 (1993).

[158] T. J. Park and J. C. Light, J. Chem. Phys. **85**, 5870 (1986).

[159] T. J. Park and J. C. Light, J. Chem. Phys. **88**, 4897 (1988).

[160] T. J. Park and J. C. Light, J. Chem. Phys. **91**, 974 (1989).

[161] T. J. Park and J. C. Light, J. Chem. Phys. **94**, 2946 (1991).

[162] T. J. Park and J. C. Light, J. Chem. Phys. **96**, 8853 (1992).

[163] N. Makri, J. Chem. Phys. **94**, 4949 (1991).

[164] M. Topaler and N. Makri, J. Chem. Phys. **101**, 7500 (1994).

[165] T. N. Truong, J. A. McCammon, D. J. Kouri, and D. K. Hoffman, J. Chem. Phys. **96**, 8136 (1992).

[166] W. H. Thompson and W. H. Miller, J. Chem. Phys. **102**, 7409 (1995).

[167] U. Manthe, J. Chem. Phys. **102**, 9205 (1995).

[168] W. H. Thompson and W. H. Miller, J. Chem. Phys. **105**, 16 (1996).

[169] H. Eyring, Trans. Faraday Soc. **34**, 41 (1938).

[170] E. Wigner, Trans. Faraday Soc. **34**, 29 (1938).

[171] J. C. Keck, Adv. Chem. Phys. **12**, 85 (1967).

[172] P. Pechukas, in *Dynamics of Molecular Collisions, Part B*, edited by W. H. Miller (Plenum Press, New York, 1976), p. 269.

[173] P. Pechukas, Ann. Rev. Phys. Chem. **32**, 159 (1981).

[174] D. G. Truhlar, B. C. Garrett, and S. J. Klippenstein, J. Phys. Chem. **100**, 12771 (1996).

[175] T. Seideman and W. H. Miller, J. Chem. Phys. **95**, 1768 (1991).

[176] H. Tal-Ezer and R. Kosloff, J. Chem. Phys. **95**, 3967 (1984).

[177] G. Arfken, *Mathematical Methods for Physicists* (Academic Press, San Francisco, 1985), pp. 731-748.

[178] S. L. Mielke, G. C. Lynch, D. G. Truhlar, and D. W. Schenke, J. Phys. Chem. **98**, 7994 (1994).

[179] H. Koizumi, G. C. Schatz, and M. S. Gordon, J. Chem. Phys. **95**, 6421 (1991).

[180] R. T. Pack, J. Chem. Phys. **60**, 633 (1974).

[181] P. McGuire and D. J. Kouri, J. Chem. Phys. **60**, 2488 (1974).

[182] J. Tennyson and J. R. Henderson, J. Chem. Phys. **91**, 3815 (1989).

[183] S. E. Choi, J. Chem. Phys. **92**, 2129 (1990).

[184] M. Mladenovic and Z. Bacic, J. Chem. Phys. **93**, 3039 (1990).

[185] M. S. Gordon, K. K. Baldridge, R. J. Bartlett, and D. Bernhold, Chem. Phys. Lett. **158**, 189 (1989).

[186] R. D. H. Brown and I. W. M. Smith, Intl. J. Chem. Kinet. **7**, 301 (1975).

[187] R. D. H. Brown and I. W. M. Smith, Intl. J. Chem. Kinet. **10**, 1 (1978).

[188] D. L. Singleton and R. J. Cvetanovic, Intl. J. Chem. Kinet. **13**, 945 (1981).

[189] I. W. M. Smith, in *Bimolecular Collisions*, edited by M. N. R. Ashfold and J. E. Baggott (Royal Society of Chemistry, London, 1989), p. 53.

[190] K. Mahamud, J.-S. Kim, and A. Fontijn, J. Phys. Chem. **94**, 2994 (1990).

[191] D. J. Rakestraw, K. G. McKendrick, and R. N. Zare, J. Chem. Phys. **87**, 7341 (1987).

[192] R. Zhang, W. J. van der Zande, M. J. Bronikowski, and R. N. Zare, J. Chem. Phys. **94**, 2704 (1991).

[193] A. Persky and M. Broida, J. Chem. Phys. **81**, 4352 (1984).

[194] K. Moribayashi and H. Nakamura, J. Phys. Chem. **99**, 15410 (1995).

[195] B. Ramachandran, J. Senekowitsch, and R. E. Wyatt, (in press).

[196] J. M. Bowman, Adv. Chem. Phys. **61**, 115 (1985).

[197] J. C. Tully, J. Chem. Phys. **93**, 1061 (1990).

[198] S. Hammes-Schiffer and J. C. Tully, J. Chem. Phys. **101**, 4657 (1994).

[199] M. Head-Gordon and J. C. Tully, J. Chem. Phys. **103**, 10137 (1995).

[200] K. Haug and H. Metiu, J. Chem. Phys. **97**, 4781 (1992).

[201] A. Staib, D. Borgis, and J. T. Hynes, J. Chem. Phys. **102**, 2487 (1995).

[202] E. R. Bittner and P. J. Rossky, J. Chem. Phys. **103**, 8130 (1995).

[203] B. J. Schwartz, E. R. Bittner, O. V. Prezhdo, and P. J. Rossky, J. Chem. Phys. **104**, 5942 (1996).

[204] X. Sun and W. H. Miller, (in press).

Ernest Orlando Lawrence Berkeley National Laboratory
One Cyclotron Road | Berkeley, California 94720

Prepared for the U.S. Department of Energy under Contract No. DE-AC03-76SF00098